Mobility of critical elements (rare earth elements and fluor) in the Montseny-Guilleries massif (Catalan Coastal Ranges, NE Iberia)

ESTEBAN MELLADO ILABACA

UNIVERSITAT AUTÒNOMA DE BARCELONA

DEPARTAMENT DE GEOLOGIA

UNITAT DE CRISTAL•LOGRAFIA I MINERALOGIA

Mobility of critical elements (rare earth elements and fluor) in the Montseny-Guilleries massif (Catalan Coastal Ranges, NE Iberia)

DOCTORAL THESIS

Esteban Mellado Ilabaca

September 2022

UAB
Universitat Autònoma
de Barcelona

UNIVERSITAT AUTÒNOMA DE BARCELONA

DEPARTAMENT DE GEOLOGIA

UNITAT DE CRISTAL•LOGRAFIA I MINERALOGIA

Mobility of critical elements (rare-earth elements and fluor) in the Montseny-Guilleries massif (Catalan Coastal Ranges, NE Iberia)

TESIS DOCTORAL

Esteban mellado ilabaca

Septiembre 2022

Memoria presentada por:

ESTEBAN MELLADO ILABACA

Para optar al grado de Doctor en Geología.

Esta memoria ha sido realizada dentro del Programa de Doctorado en Geología de la *Universitat Autònoma de Barcelona*

Tesis doctoral supervisada por: **DRA. MERCÈ CORBELLA I CORDOMÍ**

Esteban Mellado Ilabaca   Dra. M. Mercè Corbella i Cordomí

Cerdanyola del Vallès, Septiembre 2022

M. Mercè Corbella i Cordomí, Doctora de Cristal·lografia i Mineralogia del

Departament de Geologia de la Universitat Autònoma de Barcelona (UAB).

CERTIFICO:

Que els estudis recollits en la present memòria sota el títol "**Geological origin of critical elements (rare earth elements and fluor) in the Montseny-Guilleries massif (Catalan Coastal Ranges, NE Iberia)**" han estat realitzats sota la meva direcció per en Esteban Mellado Ilabaca, llicenciat en Geologia, per optar al grau de Doctor en Geologia.

I perquè així consti, signo la present certificació.

Dra. M. Mercè Corbella i Cordomí Esteban Mellado

Cerdanyola del Vallès, Setembre 2022

"Science is not just about facts and just about mathematics. It's a lot about social conventions, people you know, people you interact with, the courses you took, the professors you knew, the meetings you go to, the journals you publish in, the editors and the reviewers in your field; these are every bit as important as the actual facts"

Don L. Anderson

THESIS RULES FOR COMPENDIUM OF PUBLICATIONS

DOCTORAL PROGRAM IN GEOLOGY, UNIVERSITAT AUTÓNOMA DE BARCELONA

February 2022

REQUIREMENTS

- That it consists of a minimum of two original articles, on the same line of research, published in journals indexed in the Journal Citation Reports (Thomson Reuters).

- That the doctoral student signs as the first author of the list of authors in each of the original articles contributed.

- That these articles have been published or accepted (*) after the date of admission to the Doctoral Program (RD 99/2011) or the date of registration of the thesis (RD 1393/2007). In addition, the conformity of all the co-authors so that the articles can be used by him purpose.

- That the structure of the thesis must contain at least the following sections: an introduction, in which the works are presented and the thematic of the thesis unit is justified; a global summary of the results and the discussion of these results; the final conclusions ; a copy of the works already published and accepted by the Study Committee of Postgraduate.

PREFACE

This work corresponds to a doctoral thesis by compendium of publications, which includes two original peer-reviewed scientific articles published in journals indexed in the Journal Citation Reports, and a third article recently sent to indexed international journals:

i) **Mellado, E., Corbella, M., Navarro-Ciurana, D., Kylander-Clark, A., 2021.** The enriched Variscan lithosphere of NE Iberia: data from post-collisional Permian calc-alkaline lamprophyre dykes of Les Guilleries. Geologica Acta, 19(15), 1-23. DOI: 10.1344/GeologicaActa2021.19.15.

ii) **Mellado, E., Corbella, M., Kylander-Clark, A, 2022.** Allanite in Variscan Post-Collisional Lamprophyre Dykes from Les Guilleries (NE Iberia) as a Part of Rare Earth Elements Recycling in Collisional Orogens. Minerals, 12(8), 954.

iii) **Mellado, E., Corbella, M, 2022.** Rare earth elements and Sr-Nd isotopic compositions of fluorite from the Osor vein deposit (Catalan Coastal Ranges, NE Iberia). Ore geology reviews (unpublished)

The general objective of these projects is identifying the source and characterize the mobility of REE within the Variscan zones of the Central System (SC) of the Central Iberian Zone and the Catalan Coastal Ranges (CCR), in order to be able to predict or find primary or secondary deposits of REE in the Iberian Peninsula. At the same time, the project aims to better understand the behavior of REE in igneous, metamorphic and hydrothermal environments.

This doctoral thesis is structured in the following chapters:

Chapter 1. INTRODUCTION. It presents the motivation, interest and justification of this doctoral thesis, as well as the objectives and the methodologies used.

Chapter 2. FIRST ARTICLE. Mellado, E., Corbella, M., Navarro-Ciurana, D., Kylander-Clark, A., 2021. The enriched Variscan lithosphere of NE Iberia: data from post-collisional Permian calc-alkaline lamprophyre dykes of Les Guilleries. Geologica Acta, 19(15), 1-23. DOI: 10.1344/GeologicaActa2021.19.15. This study presents the petrography, geochemistry and geochronology of Les Guilleries Lamprophyre (LGL) dykes in order to evaluate their mantle source characteristics, melting conditions, time of emplacement, post-magmatic hydrothermal events and regional correlations. To facilitate correlations, geochemical data of the main Variscan magmatic occurrences of NE Iberia and nearby Paleozoic massifs are compiled and plotted alongside those of Les Guilleries.

Chapter 3. SECOND ARTICLE. Mellado, E., Corbella, M A. Kylander-Clark, A, 2022. Allanite in Variscan Post-Collisional Lamprophyre Dykes from Les Guilleries (NE Iberia) as a Part of Rare Earth Elements Recycling in Collisional Orogens. Minerals, 12(8), 954. This study characterizes allanite crystals from Les Guilleries spessartite dykes described in the first article to gain insights about allanite occurrence, chemical composition, age and petrogenetic implications.

Chapter 4. THIRD ARTICLE. Mellado, E., Corbella, M, 2022. Rare earth elements and Sr-Nd isotopic compositions of fluorite from the Osor vein deposit (Catalan Coastal Ranges, NE Iberia). This study uses a combination of REY geochemistry and Sr-Nd isotopic composition in the Osor fluorite deposit to get in-sights on metal and fluid sources, precipitation conditions, fluid pathways and host rock interaction. (unpublished)

Chapter 5. SUMMARY AND DISCUSSION

Chapter 6. CONCLUSIONS

Other publications related to this research that are result of participation in international and national conferences are:

- **Mellado, E., Corbella, M., Navarro-Ciurana, D., Cardellach, E., 2018.** Geoquímica y mineralogía de lamprófidos alterados en el Macizo de Les Guilleries (Cordilleras Costero Catalanas). Macla 23, 57-58. Congreso SEM 2018 (XXXVII Reunión Científica de la Sociedad Española de Mineralogía, Madrid, June 2018 (poster format).

- **Mellado, E., Corbella, M., 2019.** Estudio de allanitas en lamprófidos calcoalcalinos mediante SEM. Macla 24. Congreso SEM 2019 (XXXVIII Reunión Científica de la Sociedad Española de Mineralogía, Ronda (Málaga), June 2019 (oral presentation).

- **Mellado, E., Corbella, M., 2019.** Sr and Nd isotopes of Les Guilleries Variscan lamprophyres: Insights on mantle evolution. Goldschmidt International Conference, Barcelona, August 2019 (oral presentation).

- **Mellado, E., Corbella, M., 2021.** Los lamprófidos de Les Guilleries: último pulso ígneo Varisco en los Catalánides. II Jornada de Jóvenes Investigadores de la SEM (International videoconference, March 2021 (oral presentation).

- **Mellado, E., Corbella, M., 2021.** "Ferriallanita-(Ce), el principal portador de tierras raras en los lamprófidos calco-alcalinos de Les Guilleries. X Congreso Geológico de España, Vitoria-Gasteiz, July 2021 (oral presentation).

Index

CHAPTER 1

INTRODUCTION

Rare earth elements (REE) are a group of seventeen chemically similar metallic elements that comprise the fifteen lanthanide elements (lanthanum to lutetium), scandium (Sc), and yttrium (Y). Based on their geochemical properties, REE can be divided into light (LREE-La, Ce, Pr, Nd and Sm), medium (MREE-Eu, Gd, Tb, Dy and Y), and heavy (HREE-Ho, Er, Tm, Yb and Lu) groups (Seredin & Dai, 2012). REE constitute raw materials with multiple applications, some of them important for the current way of life in the developed world, which can allow the transition towards a greener economy (Binnemans et al., 2013). There are more than 270 minerals with significant concentrations of REE, the most common being silicates, phosphates, oxides and carbonates. Bastnäsite (carbonate), monazite and xenotime (phosphates) have historically been commercially exploited, although minerals such as apatite, allanite or eudialite also usually contain significant proportions of REE.

The global demand for REE and Y, jointly referred to as REY, has grown rapidly because they have wide applications in many high-tech products, devices, and technologies, including solar cells and wind turbines used for clean energy and batteries (Hower et al., 2016; Pecht et al., 2012). REY are irreplaceable in electronic and optical industries, oil extraction, oil refining, automobile industries, information and nano- technologies, medicine and environment protection (Seredin & Dai, 2012). They are widely used in the manufacture of special alloys, industrial ceramics, catalysts, superconductors, high-quality glass, fiber optics and storage batteries). REY consumption has shown an exponential growth in recent years and there is no doubt it will continue to grow in the foreseeable future with demand predicted to increase by 7–8% annually (Kingsnorth, 2016). China produces approximately 70% of the REE consumed in the world, while the European Union (EU) is 100% dependent on REE imports since there is no REE exploitation in Europe. For this reason and above all, due to the risk posed by dependence on the supply from China, REE is considered the critical material with the greatest risk for the EU (https://ec.europa.eu/growth/sectors/raw-materials/ specific-interest/critical/).

Traditional sources of REY are alkaline igneous complexes, carbonate-rich igneous rocks and ion-adsorption clay (Dostal, 2017). As these conventional ore deposits become progressively depleted in response to the large demand, the possibility of recovering REY and other critical elements from other sources becomes an increasingly necessary research direction (Yin & Song (2021). Although the name may lead one to think, REE are not such rare elements, since they are found in many rocks and geological environments. Its mean concentration in the crust is about 125 ppm or mg/kg (Rudnik and Gao, 2004) although concentrations vary from one rare earth to another between 1 and 250 ppm. Its concentration in the early mantle may be an order of magnitude lower (McDonough and Sun, 1995). The problem with REE lies in their exploitation, since they are rarely concentrated in minerals and in sufficient proportions to be capable of constituting a mineral deposit. The concentration of REE on Earth may be due to primary processes of the magmatic or hydrothermal type, at high temperatures, or to secondary, superficial and low-temperature processes. Most of the primary REE deposits are associated with alkaline rocks, such as those in Greenland or Sweden, and carbonatites, such as those in Norway and Finland, which are formed in extensional continental environments (Chakhmouradian and Zaitsev, 2012) from magmas that come from the mantle with a very low degree of partial fusion. They are also found in pegmatites and related to granites (skarns), which in most cases seem to

have undergone hydrothermal remobilization (Holtstam and Andersson, 2007; William-Jones et al. 2012).

The geochemical behavior of REE in the surface environment such as that of secondary deposits has been the subject of various studies, both in oxidizing and neutral pH zones and in acids in relation to acid mine drainage (e.g. Ayora et al. 2016 ; Reinhart et al. 2018; Menéndez et al. 2019; Liu et al. 2019). On the other hand, its origin and mobility in deeper environments, generally at higher pressure and temperature, is more complex. REE had been considered immobile and for this reason they are used in petrological studies as indicators of geological processes. However, there are currently many experiments and models that test its transport both in hydrothermal conditions (William-Jones et al. 2012; Krneta et al. 2018) and in carbonate magmas (Anenburg and Mavrogenes, 2018) and even in metamorphic conditions (Mair et al. al. 2017). Different experiments and calculations indicate that REE can form stable complexes of F-, Cl-, SO_4^{2-}, OH-, CO_3^{2-} and PO_4^{3-}, although given the low solubility of fluorides, carbonates and phosphates with REE, these ions would limit the REE transport by instead promoting its precipitation (Migdisov and William-Jones, 2014; Migdisov et al. 2016). The REE would easily precipitate by interaction with rocks or mixing with colder fluids or fluids of different pH or by the addition of F-, CO_3^{2-} and PO_4^{3-} in the system.

From the study of the primary deposits, it is deduced that the main source of REE lies in the mantle (e.g. Chakhmouradian and Zaitsev, 2012), although its magmas generally do not have a sufficient concentration of REE to constitute a mineral deposit. Therefore, subsequent enrichment processes are necessary to form an economic deposit. In igneous rocks, these can be fractional crystallization or immiscibility of liquids (magmas or aqueous). Repeated mantle refertilization is thought to be critical for forming REE-enriched magmas (Goodenough et al. 2016), a process that often occurs at craton margins and in collisional orogenesis. In other types of environments, remobilization by hydrothermal or meteoric fluids in the surface, can contribute to REE concentration.

REE geochemistry has been extensively used to study the genesis of fluorite concentrations in different geological environments (e.g. Bau et al., 2003, Möller et al., 1976, Schwinn and Markl, 2005). Fluorite is not only an economically important mineral, but also an important gangue mineral associated with Pb–Zn, Ag, Mo, W and Sn deposits (e.g. Chen and Li, 2009, Ep-pinger and Closs, 1990, Hill et al., 2000). Therefore, the study of REE concentration in fluorite of different hydrothermal stages can provide insights into the evolution of a fluid through time, the fluid–rock interaction and element behaviour in ore-forming processes, and can be widely used as a geochemical exploration tool (e.g. Bau and Möller, 1992, Cao, 1997, Goff et al., 2004, Jiang et al., 2006, Möller, 2001, Ronchi et al., 1993, Sánchez et al., 2010, Schönenberger et al., 2008, Subías and Fernández-Nieto, 1995).

Currently no REE deposits are being exploited in the Iberian Peninsula, but some REE concentrations higher than usual have been found in different environments. On the one hand, primary accumulations have been described in Cretaceous alkaline rocks from the west of the peninsula (Miranda et al., 2009) and Cambro-Ordovician rocks from the Galician-Portuguese Variscan zone (Montero et al. 1998; Montero et.al. 2009), but also as the result of secondary processes, in the form of placers (Inverno et al., 1998; Oliveira, 1998), in bauxites (Reinhart et al. 2018) or paleosols (Menéndez et al. 2019). On the other hand, anomalous concentrations of REE have been documented in waters containing AMD, with values in the order of μmol/L (Cravotte, 2008) when the usual values in natural waters are usually in the order of pmol/kg (Noack et al . 2014. In addition, in the Central Iberian zone, near Santa Cruz de Mudela (Ciudad Real), alluvial sands very rich in monazite nodules have been identified, some with more than 60% by weight of REE with some ppms of U-Th (García-Tenorio et al. 2018).

Taking into account that the majority of localities with anomalous REE concentrations in the Peninsula are found within the Paleozoic base, it is reasonable to assume that the Variscan materials are the source of all these concentrations. Therefore, it is plausible to suppose that the Iberian Variscan Belt may hide a mantle anomalously refertilized in REE due to the successive reactivations of the old suture zones. This doctoral thesis aims to test this working hypothesis in Les Guilleries, in the Catalan Coastal Ranges (CCR).

In the Guilleries Massif, located in the westernmost part of the CCR in North East Iberia, the exposed pre-Variscan metamorphic basement records a complex story of fluid circulation and mineralization that was overprinted by Variscan and Alpine metamorphic, magmatic and hydrothermal events. The regional tectonic setting evolved from the Carboniferous compression-transpression during the collision between Gondwana and Laurasia, to Permo-Triassic transtension-extension during the fragmentation of the Variscan Belt, to Mesozoic rifting during the opening of the Atlantic ocean, to Late Cretaceous-Miocene compression during the collision of the Iberian microplate and the European plate that formed the Pyrenees, to late Neogene extension. During each period, the inherited structural, mineralogical and geochemical features of past events combined with the effects of new tectonometamorphic, magmatic and/or hydrothermal processes to produce a wide variety of mineralogical and geochemical changes in the crustal basement. Therefore understanding the oldest events of fluid circulation are essential to understand the younger ones.

The principal aim of this thesis is to contribute to the understanding of the mobility of rare earth elements and fluor in two locations of relevance in the Guilleries massif, the lamprophyre dykes, which have been found to contain unusually high concentrations of REE, and the Osor fluorite deposit, emplaced parallel to the lamprophyres 8km to the south.

Les Guilleries lamprophyres are located in Les Guilleries massif (in the bank of the Ter river about 3.5 Km north-west of the town Anglès, Girona), and are emplaced as vertical dykes in Variscan metasediments, orthogneisses and granitic rocks in a zone adjacent to a major regional structure. These lamprophyres have been observed by many geologists but have not been characterized yet.

The abandoned Osor fluorite vein deposit is located 4 km SE of the town of Anglés and includes several geologically similar and thick (1-4 m) fluorite-barite-sphalerite-galena veins, exploited to a depth of 300 m. Gangue minerals include quartz, barite, calcite, pyrite, and silicates (mainly muscovite, albite, and biotite). Exploitation of these veins concluded in 1980, after reaching annual productions of 20,000–30,000 t of fluorite, 2000 t of Pb concentrates, and 3000 t of Zn concentrates.

The methodologies used for this study included field work and sampling of Les Guilleries lamprophyres and Osor fluorites which were used for the petrological, geochemical and geochronological analyses, using mainly optical microscopy, scanning electron microscopy, electron-microprobe chemical analyses, LA-ICP-MS chemical analyses, U-Pb dating, Sm-Nd dating and Sr isotopic analyses. Detailed geological context and descriptions of methodologies used can be found in the respective sections of each publication.

References

Anenburg, M., Mavrogenes, J.A., 2018. Carbonatitic versus hydrothermal origin for fluorapatite REE-Th deposits: experimental study of REE tansport and crustal 'antiskarn' metasomatism. American Journal of Science 318, 2018, 335-366.

Ayora C., Macias, F., Torres, E.A, Lozano, S., Carrero, J.M., Nieto, R., Pérez-López, A., Fernández-Martínez, H., Castillo-Michel, M., 2016. Recovery of Rare Earth Elements

and Yttrium from Passive-Remediation Systems of Acid Mine Drainage. Env. Science and Technology 50, 8255-8262.

Binnemans, K., Jones, P.T., Blanpain, B., Gerven, T., Yang, Y., Walton, A., Buchert, M., 2013. Recycling of Rare Earths: a critical review. Journal of Cleaner Production 51, 1-22.

Chakhmouradian, A.R., Zaitsev, A.N., 2012. Rare earth mineralization in igneous rocks: sources and processes. Elements 8, 347-353.

Chakhmouradian, A.R., Walls, F., 2012. Rare earth elements: minerals, mines, magnets (and more). Elements 8, 333-340.

Dostal, J., 2017. Rare earth element deposits of alkaline igneous rocks. Resources, 6(3), 34. https://doi.org/10.3390/resources6030034

García-Tenorio, R., Manjón, G., Vioque, I., Jiménez-Ramos, C., Mantero, J., Díaz-Francés, I., 2018. Grey monazite (rare earths) mining in centre of Spain: Characterization and pre-operational radiological evaluation. Chemosphere 208, 691-697.

Goodenough, K.M., Schilling, J., Jonssond, E., Kalvig, P., Charles, N., Tuduri, J., Deady, E.A., Sadeghi, M., Schiellerup, H., Mülleri, A., Bertrand, G., Arvanitidis, N., Eliopoulos, D.G., Shaw, R.A., Thrane, K., Keulen, N., 2016. Europe's rare earth element resource potential: An overview of REE metallogenetic provinces and their geodynamic setting. Ore Geol. Reviews 72, 838-856.

Holtstam, D., Andersson, U.B., 2007. The REE minerals of the bastnäs-type deposits, South-Central Sweden. Can. Mineral. 45, 1073–1114.

Hower, J.C., Granite, E.J., Mayfield, D.B., Lewis, A.S., Finkelman, R.B., 2016. Notes on contributions to the science of rare earth element enrichment in coal and coal combustion by-products. Minerals, 6(2), 32.

Inverno, C.M.C., Oliveira, D.P.S., 1998. REE-enriched Ordovician quartzites in Vale de Cavalos, Portalegre, Portugal. Extended Abstracts, Geocongress '98 - Past achievements / Future challenges, Geological Society of South Africa, 153-157.

Kingsnorth, D.J., 2016. Rare earths: The China conundrum. In. The 12th International Rare Earths Conference (pp. 8-10). Hong Kong.

Krneta, S., Ciobanu, C.L., Cook, N.J., 2018. Numerical Modeling of REE Fractionation Patterns in Fluorapatite from the Olympic Dam Deposit (South Australia). Minerals, 8, 342.

Liu, W.S., Wu, L.L., Zheng, M.Y., Chaoc, Y.Q., 2019. Controls on rare-earth element transport in a river impacted by ionadsorption rare-earth mining. Science of the Total Environment, 660, 697-704.

Mair, P.H., Tropper, P., Harlov, D., Manning, C., 2017. The solubility of CePO4 monazite and YPO4 xenotime in KCl-H2O fluids at 800 °C and 1.0 GPa: Implications for REE transport in high-grade crustal fluids. American Mineralogist, 102, 2457-2466.

McDonough, W.F., Sun, S.S., 1995. The composition of the Earth. Chemical Geology 120, 223-253

Migdisov, A., William-Jones, A.E., 2014. Hydrothermal transport and deposition of the rare earth elements by fluorine-bearing aqueous líquids. Miner Deposita (2014) 49, 987-997.

Migdisov, A., Williams-Jones, AE., Brugger, J., Caporuscio, F.A., 2016. Hydrothermal transport, deposition, and fractionation of the REE: Experimental data and thermodynamic calculations: Chemical Geology, 439, 13-42.

Miranda, R., Valadares, V., 2009. Age constraints on the Late Cretaceous alkaline magmatism on the West Iberian Margin. Cretaceous Research 30(3), 575-586.

Montero, P., Floor, P., 1998. The accumulation of rare-earth and high-field-strength elements in peralkaline granitic rocks; the Galiñeiro orthogneissic complex, northwestern Spain. The Canadian Mineralogist 36(3), 683-700.

Montero, P., Bea, F., Corretgé, L.G., Floor, P., Whitehouse M.J., 2009. U-Pb ion microprobe dating and Sr and Nd isotope geology of the Galiñeiro Igneous complex. A model for the peraluminous/ peralkaline duality of the Cambro-Ordovician magmatism of Iberia. Lithos 107, 227-238.

Noack, C.W., Dzombak, A., Karamalidis A.K., 2014. Rare Earth Element Distributions and Trends in Natural Waters with a Focus on Groundwater. Environ. Sci. Technol. 2014, 48, 4317-4326.

Pecht, M.G., Kaczmarek, R.E., Song, X., Hazelwood, D.A., Kavetsky, R.A., Anand, D.K., 2012. Rare earth materials: Insights and concerns (p. 194). CALCE EPSC Press.

Rudnick, R.L., Gao, S., 2004. Composition of the continental crust. In: Rudnick, R.L. (Ed.), The Crust Treatise on Geochemistry Volume 3. Elsevier-Pergamon, Oxford, 1-64.

Seredin, V.V., Dai, S., 2012. Coal deposits as potential alternative sources for lanthanides and yttrium. International Journal of Coal Geology, 94, 67-93.

Williams-Jones, A.E., Migdisov, A.A., Samson, I.M., 2012. Hydrothermal mobilisation of the rare earth elements — a tale of "ceria" and "yttria". Elements 8, 355-360.

Yin, J. N., Song, X., 2021. A review of major rare earth element and yttrium deposits in China, Australian Journal of Earth Sciences, DOI: 10.1080/08120099.2021.1929477

CHAPTER 2

FIRST ARTICLE

Reference: **Mellado, E., Corbella, M., Navarro-Ciurana, D., Kylander-Clark, A., 2021. The enriched Variscan lithosphere of NE Iberia: data from post-collisional Permian calc-alkaline lamprophyre dykes of Les Guilleries. Geologica Acta, 19(15), 1-23.**

geologicaacta

The enriched Variscan lithosphere of NE Iberia: data from post-collisional Permian calc-alkaline lamprophyre dykes of Les Guilleries

Esteban Mellado[1]   Mercè Corbella[1]   Didac Navarro-Ciurana[1]   Andrew Kylander-Clark[2]

[1]Departament de Geologia, Facultat de Ciències, Universitat Autònoma de Barcelona
Carrer de la Vall Moronta s/n, 08193 Bellaterra, Barcelona, Spain.
Telephone: +34677086033, ORCID: 0000-0002-4818-3534.
Mellado E-mail: esteban.mellado@e-campus.uab.cat

[2]LASS Facility, University of California
Santa Barbara, CA 93106, USA

┤ **A B S T R A C T** ├

Post-collisional mafic dykes crosscut the Paleozoic metamorphic basement and late-Variscan plutons in Les Guilleries massif (Catalan Coastal Ranges, NE Iberia). The predominance of mafic phenocrysts, porphyritic texture, abundant amphibole, high MgO and volatile content, together with crustal-like trace-element patterns indicate that the dykes correspond to calc-alkaline lamprophyres, mainly spessartites. Their enrichment in LILE, HFSE and REE and initial Sr-Nd isotopic compositions ($^{87}Sr/^{86}Sr_i$ between 0.70851 and 0.71127, εNd_i between -5.23 and -4.63) are consistent with an enriched subcontinental lithospheric mantle source. U-Pb ages of matrix titanite crystals yield concordia ages of 262±7Ma, congruent with crosscutting relationships. Post-magmatic processes are evidenced by intense chloritization and albitization of the lamprophyres, together with systematic variations of Na_2O vs SiO_2, K_2O, CaO, Ba, Rb, Cs, Pb, Sr, Tl, and Zn, and possibly the removal of F. The geochemical and geochronological data support an orogenic geochemical affinity, in accordance with the transitional tectonic regime between Variscan compression/transpression and post-collisional transtension/extension, related to the fragmentation of Pangea and thinning of the lithosphere. The lamprophyre dykes studied could represent the youngest pulse of Variscan orogenic magmatism and, therefore, mark its end in NE Iberia before the onset of the generalized Triassic extension.

KEYWORDS | Calc-alkaline lamprophyre. Post-collisional dykes. Sr-Nd isotopes. Les Guilleries Massif. Catalan Coastal Ranges. Variscan Orogeny.

INTRODUCTION

Dyke swarms hold one of the keys to understanding the plate tectonics as they provide information on the extensional processes occurring in the continental and oceanic lithosphere (Peng *et al.,* 2016). Mafic dykes in particular are the primary channels of deep magma transport into the crust from a source area in the mantle;

they can thus be used to assess the nature of their parental magmas, location of magma reservoirs, emplacement mechanisms and/or regional paleostress conditions and to reconstruct ancient continental palaeogeographic regimes (Srivastava *et al.,* 2019).

In the Variscan Belt of Western Europe, mafic dyke swarms are essential constituents of the two main tectono-

magmatic and sedimentary cycles defined for the post-collisional orogenic evolution (Cortesogno *et al.*, 1998). The first cycle of Upper Carboniferous-Lower Permian age is ruled by an extensional, trans-tensional tectonic regime and is characterized by the calc-alkaline plutonic-volcanic magmatism and fluvio-lacustrine sedimentation. Dyke emplacement in the first cycle occurred diachronically in the Pyrenees, Iberian Ranges, Catalan Coastal Ranges (CCR) and Sardinia, and at different crustal levels (Lago *et al.*, 2004; Perini *et al.*, 2004; Ronca *et al.*, 1999; Ubide *et al.*, 2010; respectively). The second cycle is characterized by a plutonic-volcanic magmatism of alkaline geochemical signature associated with continental and shallow-marine sedimentation, generally developed from late Permian to early Triassic in south-western Europe, but was active since early Permian in some places (Cortesogno *et al.*, 1998). It marks an extensional event disconnected from the collapse of the Variscan belt, and likely related with the post-Variscan global re-organization of plates that would lead to the neo-Tethyan rifting in late Triassic times (Bonin, 1987; Orejana *et al.*, 2008; Wilson *et al.*, 2004).

The calc-alkaline mafic dyke swarms of the first cycle include, in some locations, potassium-rich varieties, such as lamproites, and calc-alkaline lamprophyres (spessartites, vosgesites, kersantites and minettes), that suggest the Variscan Subcontinental Lithospheric Mantle (SCLM) sources contained enriched domains in LILE (Large Ion Lithophile Elements: Ba, K, Rb, Sr, Th, U and Pb), HFSE (High Field Strength Elements: Hf, Nb, Ta, Ti, Zr and P) and REE (Rare Earth Elements), with high $^{87}Sr/^{86}Sr_i$ and low εNd_i (Perini *et al.*, 2004; Seifert, 2008; Soder, 2017). The general consensus is that these enriched domains are formed by metasomatism of the SCLM in suprasubduction zones when silica-rich, carbonatite-rich and/or asthenospheric melts penetrate mantle peridotite as vein networks (Foley, 1992; Prelević *et al.*, 2004; Seifert, 2008; Soder, 2017). Then, when the enriched mantle domains are affected by low degree melting, potassium-rich mafic magmas with a hybrid crustal and mantle signature may form; this magma can differentiate during ascent and may emplace at different crustal levels (Awdankiewicz, 2007; Elter *et al.*, 2004; Prelević *et al.*, 2004; Soder, 2017).

Alkaline mafic dykes of the second cycle also include potassium rich varieties such as camptonites, but they have a distinctive Oceanic Island Basalt (OIB) trace-element character with enrichments in LILE, HFSE and Light Rare Earth Elements (LREE), positive Nb-Ta and Ti anomalies, low $^{87}Sr/^{86}Sr_i$ and high εNd_i. This suggests an anorogenic nature of the magmas with no involvement of crustal and/or subduction-related components (Orejana *et al.*, 2008; Scarrow *et al.*, 2009).

The Catalan Coastal Ranges (CCR), which conform the north-easternmost Variscan domain of the Iberian Peninsula, contain different sets of lamprophyric dyke swarms. In the locality of Aiguablava, at Costa Brava, dykes with a calc-alkaline geochemical signature appear crosscut by others of alkaline affinity (Enrique, 2009; Ubide *et al.*, 2010). The former (mainly spessartites) intrude a ca. 288Ma leucogranite and have been interpreted to be of Permian age (Enrique, 2009; Losantos, 2000). Structural analyses have shown that these dykes are oriented WNW-ESE and intruded along a preexisting joint network in late-Variscan batholiths during a post-collisional extensional/transtensional tectonic regime (Martínez-Poza *et al.*, 2014). The second type of lamprophyres correspond to camptonites, which have $^{40}Ar/^{39}Ar$ ages of ca. 79.0±0.5Ma, unrelated to the Variscan orogeny (Ubide, 2013). This author interpreted the alkaline lamprophyres of CCR to represent the final stage of a series of alkaline magmatic pulses in NE Iberia that could have started during Triassic times, and lasted until the beginning of the Alpine orogeny, in relation with the continental rift setting developed in SW Europe during that period.

Vertical lamprophyric dykes also occur in Les Guilleries Massif, in the West-Central part of the CCR (about 50km west of Aiguablava), cutting metamorphic Paleozoic rocks (Fig. 1) and Variscan granitoids. Although they have been observed by many geologists, they have not been characterized yet. This study presents the petrography, geochemistry and geochronology of Les Guilleries Lamprophyre (LGL) dykes in order to evaluate their mantle source characteristics, melting conditions, time of emplacement, post-magmatic hydrothermal events and regional correlations. To facilitate correlations, geochemical data of the main Variscan magmatic occurrences of NE Iberia and nearby Paleozoic massifs are compiled and plotted alongside those of Les Guilleries.

GEOLOGICAL SETTING

Les Guilleries Massif, located in the north-western part of the CCR (Fig. 1A), mainly consists of Cambro-Ordovician metasedimentary units and orthogneisses cut by Variscan syn- to post-collisional intrusions (Durán, 1985, 1990). The massif is composed of three blocks separated by NE-SW striking normal faults. The deeper and higher-grade metamorphic block, the Osor block, outcrops in the southern part of the massif and contains sillimanite-grade metapelites with interlayered metapsammites, calc-silicates, amphibolites, and orthogneisses (Durán, 1985, 1990; Martínez *et al.*, 2008; Reche and Martínez, 2002; Sebastian, *et al.*, 1990). The Susqueda block is the intermediate one, which is composed of metapelites and metapsammites with quartzite layers and represents shallower levels of the crust, as the metamorphism reaches the andalusite-cordierite grade. The Osor and Susqueda
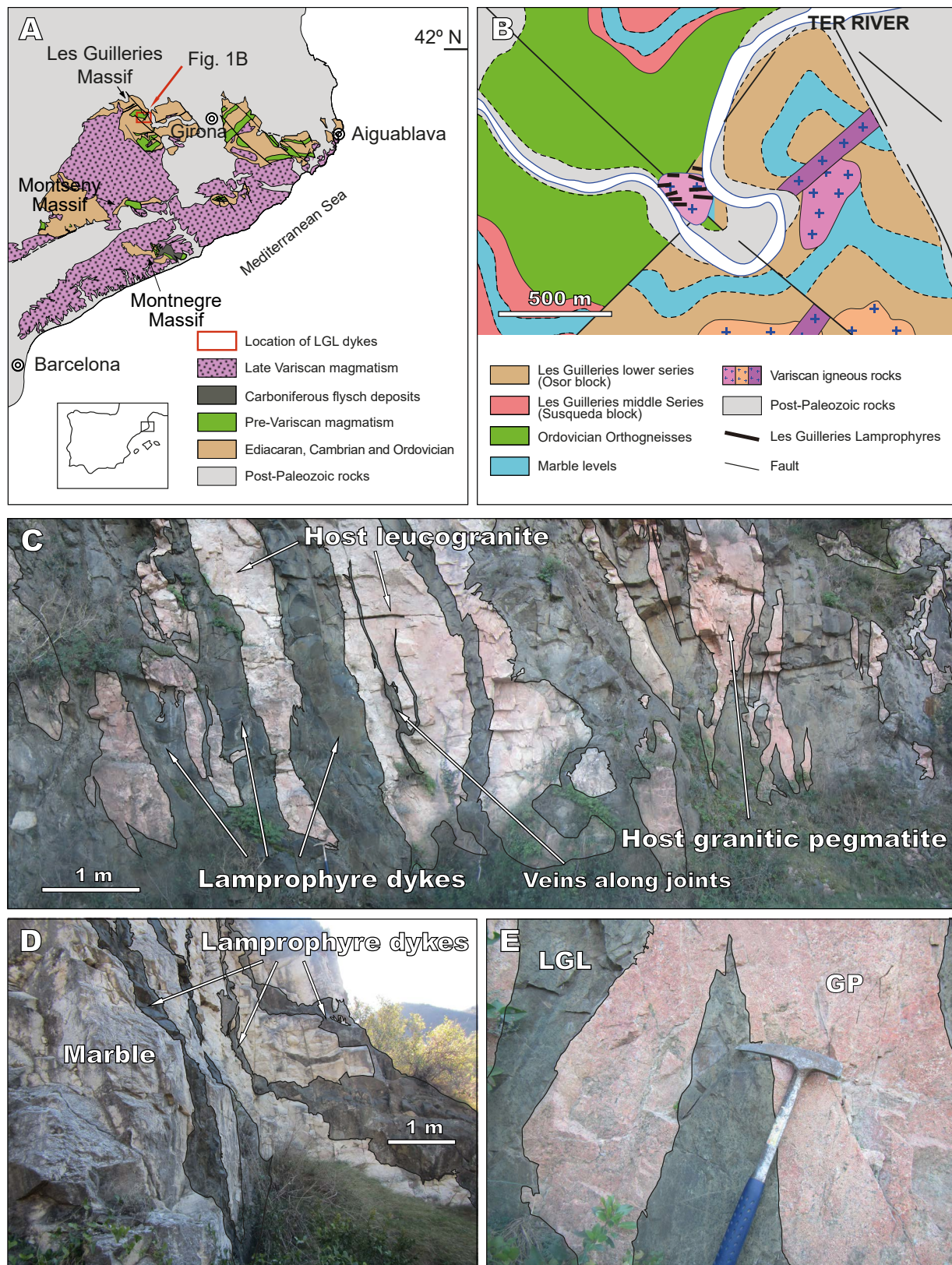
FIGURE 1. A) Location of les Guilleries Massif and Les Guilleries Lamprophyre (LGL) dykes within the Catalan Coastal Ranges. B) Detailed geological map of the study area and location of les Guilleries Lamprophyre dykes. C) Photograph of a lamprophyre dyke swarm cross-cutting Variscan leucogranites and granitic pegmatites. D) Photograph of lamprophyre dykes in a host marble. E) Photograph of lamprophyres (LGL) in a Variscan Granitic Pegmatite (GP) host.

blocks contain sill-like bodies of orthogneisses that record essentially continuous magmatic activity beginning at the Cambro-Ordovician boundary (488±3Ma) and reaching a peak of intrusions volume during the late Ordovician (462±8 to 459±3Ma; Martínez *et al.*, 2011). The northern and uppermost Sant Martí block is composed of Ordovician metavolcanic rocks interbedded with metagreywackes and metapelites (U-Pb age 452±4Ma; Martínez *et al.*, 2011). Some Silurian and Devonian volcanosedimentary rocks also crop out in the northern part, although the sequences appear incomplete due to faulting (Durán, 1990).

Several Variscan igneous rocks intruded the metasedimentary sequences of Les Guilleries Massif. The oldest Variscan intrusive forms the Susqueda complex, the largest basic massif of the CCR, which is composed of quartz diorites and diorites with calc-alkaline geochemical affinity, together with hornblende gabbros and hornblendites (Enrique, 1990; Esteve *et al.*, 2016). One syn-collision diorite sheet provided an U-Pb age of 323.6±2.8Ma (Martínez *et al.*, 2008), and most mafic intrusives are considered younger and post-tectonic (Esteve *et al.*, 2018). The Susqueda complex induces granulite-grade contact metamorphism and silica depleted melting in the host Susqueda block metasediments (Riesco *et al.*, 2004). Younger granites 305-299Ma old (U-Pb zircon ages; Martínez *et al.*, 2008) are abundant in the Osor block. Unpublished U-Pb Sensitive High Mass-Resolution Ion Microprobe (SHRIMP) ages of 284±3Ma have been found for post-collisional porphyritic granitoids (F.J. Martínez personal communication), which agree with the age of similar mafic and felsic plutonic bodies in the nearby Montnegre Massif, that yield ^{40}Ar/^{39}Ar ages between ca. 291 and 285Ma (Solé *et al.*, 2002). Ultrabasic-basic to intermediate rocks also appear associated with late-Variscan calc-alkaline granites in the Montnegre Massif, showing mineralogical and geochemical characteristics typical of appinite suites, with cumulate hornblendites and gabbros crystalized from K-rich and fluid-rich magmas and a complex mingled zone between diorites and biotite granodiorites (Butjosa *et al.*, 2013; Galán *et al.*, 2017).

Several types of ore mineralizations have been found in Les Guilleries (Ayora, 1990). Epigenetic mineralizations, mainly skarns (Cu, Fe, Zn, Pb) and veins (F, Ba, Zn, Pb), seem to be related to hydrothermal fluid circulation induced by the post-metamorphic granitic intrusions (Ayora, 1990). The most important deposit occurs in the Osor block and consists of fluorite-barite veins with sphalerite and galena crosscutting Variscan porphyritic granites and metapelites. These veins show different stages of recrystallization that have been attributed to Variscan movements and subsequent rejuvenation during the Alpine orogeny (Campá-Viñeta and Montoriol-Pous, 1974).

To date, Permain basins haven't been observed in Les Guilleries Massif. The area is thus interpreted as a topographic high since early Permian and affected by the Permo-Triassic erosional paleosurface, adjacent to pull-apart basins developed in dextral transtensional settings (Innocent *et al.*, 1994; Lago *et al.*, 2004). Some of the nearest Permian records are found in the Eastern Pyrenees, 90km to the NE (Serra del Cadí; Innocent *et al.*, 1994) and in the Iberian Ranges, 300km to the SE. These Permian basins record several syn- and post-rift depositional cycles, with or without volcanism, and a marked transition from calc-alkaline volcanism in the early-mid Permian to alkaline volcanism in the late Permian (Arche and López-Gómez, 1996; Innocent *et al.*, 1994).

SAMPLING AND ANALYTICAL TECHNIQUES

Seven lamprophyre dykes and their wall-rocks were sampled in order to cover the differences encountered in the field. Petrographic analysis and Scanning Electron Microscope (SEM) characterization were performed at the Geology Department and Serveis de Microscòpia of the Universitat Autònoma de Barcelona. The representative 13 samples were crushed and pulverized to 200μm and sent to ACTLABS, Ontario (Canada), for whole-rock geochemical analysis of 51 elements, including major, trace and rare earth elements. The analytical techniques used were lithium metaborate/tetraborate fusion with subsequent analysis by Ion Selective Electrode (ISE) for fluorine and Inductively Coupled Plasma Mass Spectrometry (ICP-MS) for the rest of the elements (SiO_2, TiO_2, Al_2O_3, Fe_2O_3, MnO, MgO, CaO, Na_2O, K_2O, P_2O_5, Li, Be, Sc, V, Cr, Co, Ni, Cu, Zn, Ga, Ge, Rb, Sr, Y, Zr, Nb, Sn, Cs, Ba, La, Ce, Pr, Nd, Sm, Eu, Gd, Tb, Dy, Ho, Er, Tm, Yb, Lu, Hf, Ta, W, Tl, Pb, Th and U). Detection limits and analytical errors are presented in Table 1.

Sr-Nd isotopic analyses were carried out at the Geochronology Unit of Universidad Complutense de Madrid (UCM). For ^{87}Sr/^{86}Sr, a mass spectrometer VG Sector-54® was used, following data acquisition method of dynamic multicollection during 10 blocks of 16 cycles each, with beam intensity of 3V. Isotopic standards used were NBS 987 (^{87}Sr/^{86}Sr= 0.710248±0.000003, National Bureau of Standards Certificate of Analysis). For ^{143}Nd/^{144}Nd mass spectrometer TIMS-Phoenix® was used, following data acquisition method of dynamic multicollection during 160 cycles with beam intensity of 1V. Isotopic standard used was JNd$_{i-1}$ (^{143}Nd/^{144}Nd= 0.512115±0.000002; Tanaka *et al.*, 2000). Analytical errors referred to two standard deviations are 0.01% for ^{87}Sr/^{86}Sr and 0.006% for ^{143}Nd/^{144}Nd.

U-Pb age measurements were conducted for titanite and allanite grains of samples from two dykes. Thin sections

TABLE 1. Whole-rock major and trace element concentration of LGL dykes

	Unit	DL	Dyke 1	Dyke 2	Dyke 3	Dyke 4	Dyke 5	Dyke 6	QMonz	Grd	GrPeg	LeuGr	LeuGr	LeuGr	LeuGr
SiO_2	wt.%	0.01	49.82	51.19	51.78	53.53	51.85	50.49	70.67	67.45	74.99	70.95	71.67	68.32	66.81
Al_2O_3	wt.%	0.01	16.46	15.24	16.44	15.75	16.17	15.53	14.94	16.14	13.99	14.96	14.73	15.36	15.84
$Fe_2O_3(T)$	wt.%	0.01	8.09	9.02	9.09	8.66	8.45	9.15	3.49	4.06	0.75	2.67	2.69	2.75	3.12
MnO	wt.%	0.001	0.188	0.165	0.169	0.193	0.141	0.134	0.169	0.15	0.046	0.046	0.052	0.052	0.056
MgO	wt.%	0.01	6.16	6.75	5.39	6.34	6.38	6.66	0.81	1.61	0.3	1.3	1.15	1.48	1.65
CaO	wt.%	0.01	6.42	5.72	5.65	3.61	6.35	6.56	2.31	2.51	0.63	1.03	0.81	0.99	1.06
Na_2O	wt.%	0.01	2.47	3.13	3.71	4.33	2.77	2.46	3.49	4.12	4.65	4.05	4.34	4.4	4.93
K_2O	wt.%	0.01	2.05	1.71	0.8	0.27	1.12	1.29	3.25	2.29	3.84	2.69	2.77	2.6	2.77
TiO_2	wt.%	0.001	1.409	1.318	1.453	1.376	1.306	1.418	0.338	0.498	0.051	0.351	0.356	0.387	0.421
P_2O_5	wt.%	0.01	0.37	0.39	0.4	0.37	0.34	0.42	0.11	0.15	0.22	0.11	0.16	0.14	0.17
LOI	wt.%		5.29	4.08	4.66	5.01	4.36	5.88	0.83	1.61	0.79	1.75	1.72	2.05	1.95
Total	wt.%	0.01	98.72	98.72	99.56	99.44	99.23	100	100.4	100.6	100.3	99.9	100.4	98.54	98.77
F	wt.%	0.01	0.08	0.06	0.06	0.07	0.03					0.02	0.02	0.03	0.03
Sc	ppm	1	27	25	27	26	26	25	7	9	5	6	6	6	6
Be	ppm	1	2	2	3	3	2	2	1	1	2	2	2	2	2
V	ppm	5	176	161	173	148	167	175	29	48	< 5	26	28	29	37
Cr	ppm	20	210	280	150	190	200	300	50	30	< 20	< 20	< 20	< 20	< 20
Co	ppm	1	29	33	44	32	41	32	47	27	67	28	38	33	23
Ni	ppm	20	80	100	50	70	80	110	< 20	< 20	< 20	< 20	< 20	< 20	< 20
Cu	ppm	10	< 10	30	40	< 10	30	30	40	10	10	< 10	< 10	< 10	< 10
Zn	ppm	30	130	130	170	230	90	110	40	50	< 30	40	40	50	40
Ga	ppm	1	22	19	21	20	19	18	18	19	13	18	18	18	19
Ge	ppm	0.5	1.6	1.7	2.4	2.3	1.2	2	1.8	1.9	2	1.1	1.1	1.3	1.2
As	ppm	5	< 5	< 5	< 5	< 5	< 5	< 5	< 5	< 5	< 5	< 5	< 5	< 5	< 5
Rb	ppm	1	68	51	29	9	47	46	74	58	95	73	74	69	71
Sr	ppm	2	391	295	360	296	349	310	309	371	135	243	199	204	230
Y	ppm	0.5	34.1	32.7	36.6	35.6	32.7	32.1	23.7	20.1	10	17.9	17.6	18.6	16.2
Zr	ppm	1	255	245	260	255	231	219	124	145	13	159	152	168	178
Nb	ppm	0.2	14.3	15.2	14.9	15	13.4	14.8	8	7.9	5.6	6.3	6.4	7.1	7.6

TABLE 1. Continued

	Unit	DL	Dyke 1	Dyke 2	Dyke 3	Dyke 4	Dyke 5	Dyke 6	QMonz	Grd	GrPeg	LeuGr	LeuGr	LeuGr	LeuGr
Mo	ppm	2	< 2	< 2	< 2	< 2	< 2	< 2	< 2	< 2	< 2	< 2	< 2	< 2	< 2
Ag	ppm	0.5	0.8	0.7	0.7	0.7	0.7	0.6	< 0.5	0.5	< 0.5	0.5	< 0.5	0.6	0.5
In	ppm	0.1	0.1	< 0.1	< 0.1	< 0.1	< 0.1	0.1	< 0.1	< 0.1	< 0.1	< 0.1	< 0.1	< 0.1	< 0.1
Sn	ppm	1	2	1	1	1	< 1	1	1	1	4	< 1	< 1	< 1	1
Sb	ppm	0.2	< 0.2	< 0.2	< 0.2	< 0.2	< 0.2	< 0.2	< 0.2	< 0.2	< 0.2	< 0.2	< 0.2	< 0.2	< 0.2
Cs	ppm	0.1	2.2	1.4	1.3	0.6	1.7	2.6	2.2	1.4	2.5	1.9	2.1	3	1.9
Ba	ppm	2	776	483	348	61	412	619	783	624	452	772	644	619	627
La	ppm	0.05	40.2	43.2	42	38.3	37.5	39.1	34.3	31.8	4.69	27.8	27.1	30	30.5
Ce	ppm	0.05	86.2	89.3	90.2	82.4	80.5	83.8	69.7	64.5	9.98	56.3	56.1	60.6	60.7
Pr	ppm	0.01	10.5	10.9	11.1	10.1	9.79	10.3	7.9	7.39	1.18	6.41	6.37	7.04	6.95
Nd	ppm	0.05	41.7	43.7	43.4	40.7	39.3	42	30.4	28.1	4.38	24.3	24.3	26	26
Sm	ppm	0.01	8.58	8.32	8.9	8.22	8.09	8.5	6.1	5.41	1.62	4.76	4.59	5.26	4.98
Eu	ppm	0.005	1.91	1.87	2	1.72	1.83	1.91	1.04	1.11	0.413	0.999	0.964	1.01	1.11
Gd	ppm	0.01	6.82	6.87	7.46	7.03	6.58	6.92	4.84	4.57	1.64	3.72	3.82	3.91	3.7
Tb	ppm	0.01	1.04	1.07	1.13	1.1	1.04	1.08	0.74	0.65	0.33	0.56	0.57	0.6	0.56
Dy	ppm	0.01	6.39	6.07	6.84	6.46	6.12	6.09	4.16	3.64	2.03	3.24	3.18	3.5	3.21
Ho	ppm	0.01	1.2	1.12	1.3	1.21	1.18	1.18	0.8	0.72	0.37	0.61	0.61	0.65	0.58
Er	ppm	0.01	3.5	3.24	3.59	3.41	3.34	3.25	2.2	1.97	0.86	1.72	1.7	1.74	1.57
Tm	ppm	0.005	0.489	0.46	0.493	0.49	0.467	0.466	0.328	0.278	0.123	0.245	0.233	0.24	0.21
Yb	ppm	0.01	3.11	2.82	3.22	3.14	3.04	2.98	2.16	1.71	0.84	1.51	1.5	1.5	1.33
Lu	ppm	0.002	0.484	0.425	0.501	0.454	0.462	0.472	0.327	0.254	0.128	0.21	0.23	0.22	0.213
Hf	ppm	0.1	6	5.7	6.2	5.9	5.2	5.4	3.9	4.1	0.6	4	3.9	4.3	4.3
Ta	ppm	0.01	0.87	0.9	0.92	0.86	0.97	0.81	1.39	0.87	1.8	1.11	1.28	1.14	0.99
W	ppm	0.5	54.4	55.1	79.6	52.9	102	30.9	347	195	429	303	407	364	233
Tl	ppm	0.05	0.35	0.27	0.16	< 0.05	0.22	0.26	0.45	0.35	0.45	0.37	0.4	0.36	0.36
Pb	ppm	5	23	15	8	6	6	< 5	14	11	21	8	9	6	< 5
Bi	ppm	0.1	0.8	0.2	0.3	0.8	< 0.1	< 0.1	< 0.1	< 0.1	< 0.1	< 0.1	< 0.1	< 0.1	< 0.1
Th	ppm	0.05	5.53	6.13	5.72	5.5	5.29	5.8	9.89	7.69	1.41	7.23	7.22	7.33	7.96
U	ppm	0.01	1.15	1.06	8.31	2.04	0.91	0.99	1.36	1.12	2.26	1.62	1.99	1.62	1.73
Mg#			60.1	59.7	54	59.1	59.9	59	31.49	43.99	44.20	49.09	45.85	51.60	51.16

were sent to University of California (UC) Santa Barbara (United States of America) for in situ U-Pb dating via Laser Ablation Inductively Coupled Plasma Mass Spectrometry (LA-MC-ICPMS) following the procedures outlined in Spencer *et al.* (2013), Kylander-Clark *et al.* (2013) and Kylander-Clark (2020). Samples were ablated with a Photon Machines Excite 193 nm laser ablation system equipped with a HelEx cell, using a spot size of $25\mu m$ and a repetition rate of 5Hz. Aerosol from the laser was carried in a mixture of He and Ar and analyzed by a Nu Instruments Plasma High Resolution Multi Collector Inductively Coupled Plasma Mass Spectrometry (HR MC-ICPMS) for U-Pb analysis and by an Agilent 7700X for trace-element analysis. For titanite, Reference Material (RM) MKED (Spandler *et al.*, 2016) was used to correct for instrumental offset of isotopic ratios, and BLR (Aleinikoff *et al.*, 2007) and Y1710C5 (Kylander-Clark *et al.*, 2008) were used to ensure accuracy; secondary RMs yielded ages within 2% of accepted values. Allanite analysis and data reduction required a two-step approach, first using NIST612 glass to correct for instrument drift and bias in $^{207}Pb/^{206}Pb$ and $^{206}Pb/^{238}U$ ratios, followed by a correction of the $^{206}Pb/^{238}U$ ratio such that RMs SISS, BONA, and TARA yielded ages within 2% of accepted values (von Blanckenburg *et al.*, 1992; Smye *et al.*, 2014). Trace-elements were determined using NIST612 as the primary RM and ^{28}Si as the internal standard, assuming 19.2 wt% in titanite and 14 wt% in allanite.

In order to recognize possible genetic relationships between the LGL dykes, their host rocks and other Variscan magmatic occurrences, their chemical composition has been compared with those of several rocks that represent some of the compositional end members of Variscan magmatism of Western Europe. These are calc-alkaline lamprophyres and lamproites to represent different extents of SCLM enrichment, Permian calc-alkaline volcanic andesites and alkaline basalts from eastern Pyrenees and the Iberian Ranges, Permian alkaline lamprophyres from the Iberian Central System (ICS) to represent asthenospheric influences, and ultramafic (appinites) to felsic intrusives of the Catalan Coastal Batholith and appinites from NW Iberia to represent main Variscan mantle-crust magmatism (compiled data in Appendix I).

FIELD OBSERVATIONS AND PETROGRAPHY

Les Guilleries lamprophyres crop out in a narrow zone (<2km²) on the walls of a unique meander of the Ter River, which formed by Alpine rejuvenation of the terrane. The meander probably reflects the strength to weathering of the Variscan granitoids that host the lamprophyres. This zone is highly fractured and highly altered in some places, reflecting multiple superimposed processes heterogeneously affecting the rocks at the meter scale.

Les Guilleries lamprophyres appear as a vertical to sub-vertical dyke swarm with branching dykes of some centimeters to meters in width and tens of meters in length, emplaced in the intersection of two perpendicular fault systems oriented NE-SW and NW-SE (Fig. 1A-B). They are dark colored that contrasts with the white to red granitoid hosts (quartz-monzonites, granodiorites, leucogranites and granitic pegmatites) and the grayish lower Paleozoic schists and marbles (Fig. 1C-E). The dykes are approximately E-W oriented although segmentation of the dykes in other directions is noticeable at decimeter- to centimeter-scale, along fractures and joints. The dykes have sharp contacts with their host rocks, with no evident fracturing at the tips of single veins (Fig. 1C). In hand specimens, all lamprophyres present a fine porphyritic texture with millimetric green phenocrysts and some sulfides in a micrometric groundmass, with variable spatial distribution of the phenocrysts at a centimetric scale.

The phenocrysts consist of mostly light green chlorite as seen in thin section, possibly altering pyroxene, amphibole and/or phlogopite crystals, with variable amounts of secondary epidote, albite and calcite, with some pyrite and chalcopyrite inclusions (Fig. 2A-C). These altered phenocrysts varied in shape and size (0.5 - 1.5mm). Millimeter size subhedral anortithe-albite phenocrysts are also present in all samples with varying proportions, commonly showing sericite and hematite inclusions (Fig. 2C). Millimetric dark brown amphibole phenocrysts up to 1.5mm, strongly replaced by chlorite and albite, are only present in some dykes, which appear to be the less altered (Fig. 2D). Some dykes contain millimetric xenocrysts of rimmed alkali feldspar whereas quartz occurs sporadically in others (Fig. 2E). Veins of epidote, calcite or both, of micrometric to millimetric width, are present in all dykes but are more common in the most altered ones (Fig. 2F).

The groundmass of the less altered dykes is composed of primary amphibole (actinolite to hornblende with cores slightly enriched in titanium and alkalis), anortithe, albite, K-feldspar and minor titanite, epidote, calcite, ilmenite, allanite, fluoroapatite, spinel, zircon, and pyrite together with secondary calcite, epidote, chlorite, albite, titanite and quartz (Fig. 2G-H). A diminishing content of amphibole, anorthite and K-feldespar along with an increasing content of albite, chlorite, epidote, titanite and quartz are observed with increasing alteration. Thus, the most altered dykes are dominated by secondary chlorite and albite phenocrysts, with a groundmass dominated by albite and chlorite (Fig. 2I) and minor epidote, titanite, ilmenite, quartz and rutile.

WHOLE-ROCK MAJOR AND TRACE ELEMENT CHEMISTRY

Major- and trace-element concentration of the LGL dykes are presented in Table 1. Even though some dykes appear
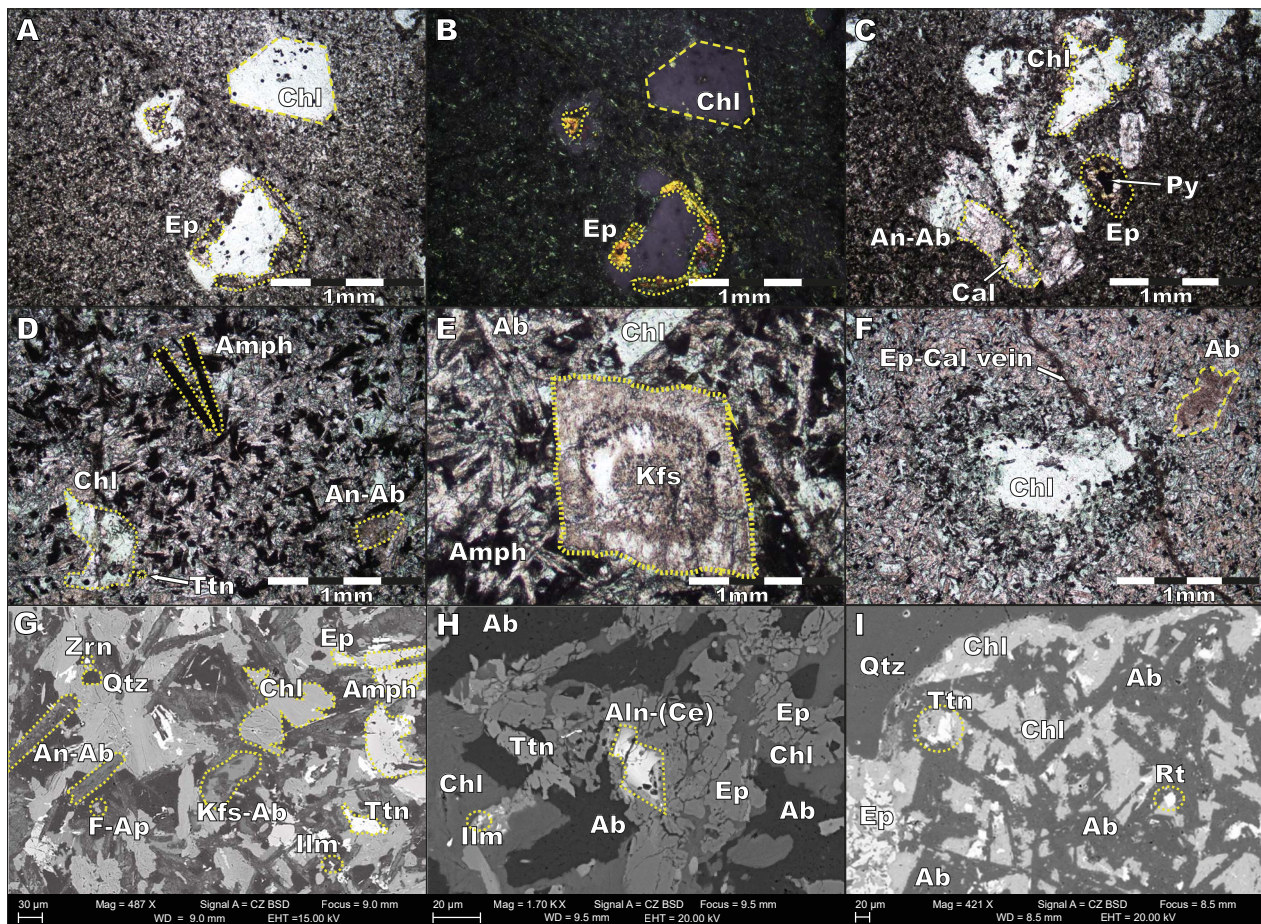
FIGURE 2. Photographs (A-F) and Back-Scattered Electron (BSE) images (G-I). A) Chloritized phenocrysts with inclusions and rims of epidote, in a fine grained matrix of mainly chloritized domains (green) and feldespatic domains (white), with opaque minerals mainly altered amphibole and titanite (black). B) Figure 2A in cross-polarised light. C) Glomeroporphyritic texture of chloritized mafic phenocrysts and albitized anorthite phenocrysts, with minor epidote and calcite, and pyrite inclusions. D) Elongated dark brown amphibole phenocrysts in a less altered sample. E) Sporadic rimmed alkali feldspar xenocryst. F) Chloritized phenocryst surrounded by tiny crystals of amphibole, chlorite and anorthite-albite (commonly known as "ocelli") reflecting disequilibrium conditions. Reddish hematitized albite phenocryst and epidote-calcite veins are also shown. G) Representative sample of the less altered dykes. It shows primary amphibole (mainly actinolite and hornblende), anorthite, K-feldspar, titanite, ilmenite, F-apatite, zircon and secondary chlorite, epidote, albite and quartz. H) Magmatic allanite-(Ce) affected by epidotization, chloritization and albitization (in that order). Some allanite crystals are surrounded by epidote coronas (not shown). I) Representative sample of the most altered dykes, showing predominance of secondary albite in the lamprophyre matrix, followed by chlorite and minor epidote, titanite and rutile. In the top left, part of a quartz xenocryst shows slightly reabsorbed boundaries. Ab: albite. Aln-(Ce): allanite-(Ce). Amph: amphibole. An: anorthite. Cal: calcite. Chl: chlorite. Ep: epidote. F-Ap: fluoroapatite. Ilm: ilmenite. Kfs: k-feldespar. Py: pyrite. Qtz: quartz. Rt: rutile. Ttn: titanite. Zrn: zircon.

more altered than others, they all present similar values of MgO (5.3-6.8%; Mg# 54-60), Al_2O_3 (15.2-16.5%), Fe_2O_3T (8.0-9.2%), TiO_2 (1.3-1.5%), P_2O_5 (0.37-0.42%), MnO (0.13-0.20%) and Loss On Ignition (LOI, 4.08-5.29%). However, the concentration is more variable in SiO_2 (49.8-53.6%), CaO (3.6-6.6%), Na_2O (2.4-4.4%) and K_2O (0.2-2.1%). These compositions plot in the calc-alkaline field (Fig. 3A) in the Na_2O+K_2O vs SiO_2 diagram of Rock (1991); ranging from the limit of the shoshonite to low-K calc-alkaline suites (Fig. 3B) in a K_2O vs SiO_2 diagram (Peccerillo and Taylor, 1976). These lamprophyres contain more iron than magnesium ($Fe_2O_3T>MgO$), more sodium than potassium ($K_2O/Na_2O<1$), and the K_2O content is generally inversely correlated with that of Na_2O (Fig. 3C). Silica concentration is directly proportional

to Na_2O concentration and inversely related to CaO and K_2O contents; these compositional variations are in agreement with the abundance of albite, anorthite and K-feldspar described in the Petrography section. All dykes show similar immobile Zr/Ti and Nb/Y ratios, corresponding to andesite to sub-alkaline basalt affinities (Fig. 3D).

Enrichments in LILE (K, Ba, Cs, Rb, Th) and HFSE (Zr, Hf), positive Pb and negative Nb, Ta, Sr and Ti anomalies can be observed for most dykes in a trace-element pattern normalized to primitive mantle values diagram (Fig. 4A). These are common features for calc-alkaline lamprophyres (Rock, 1991) and are also observed in Aiguablava dykes (Ubide *et al.,* 2010).
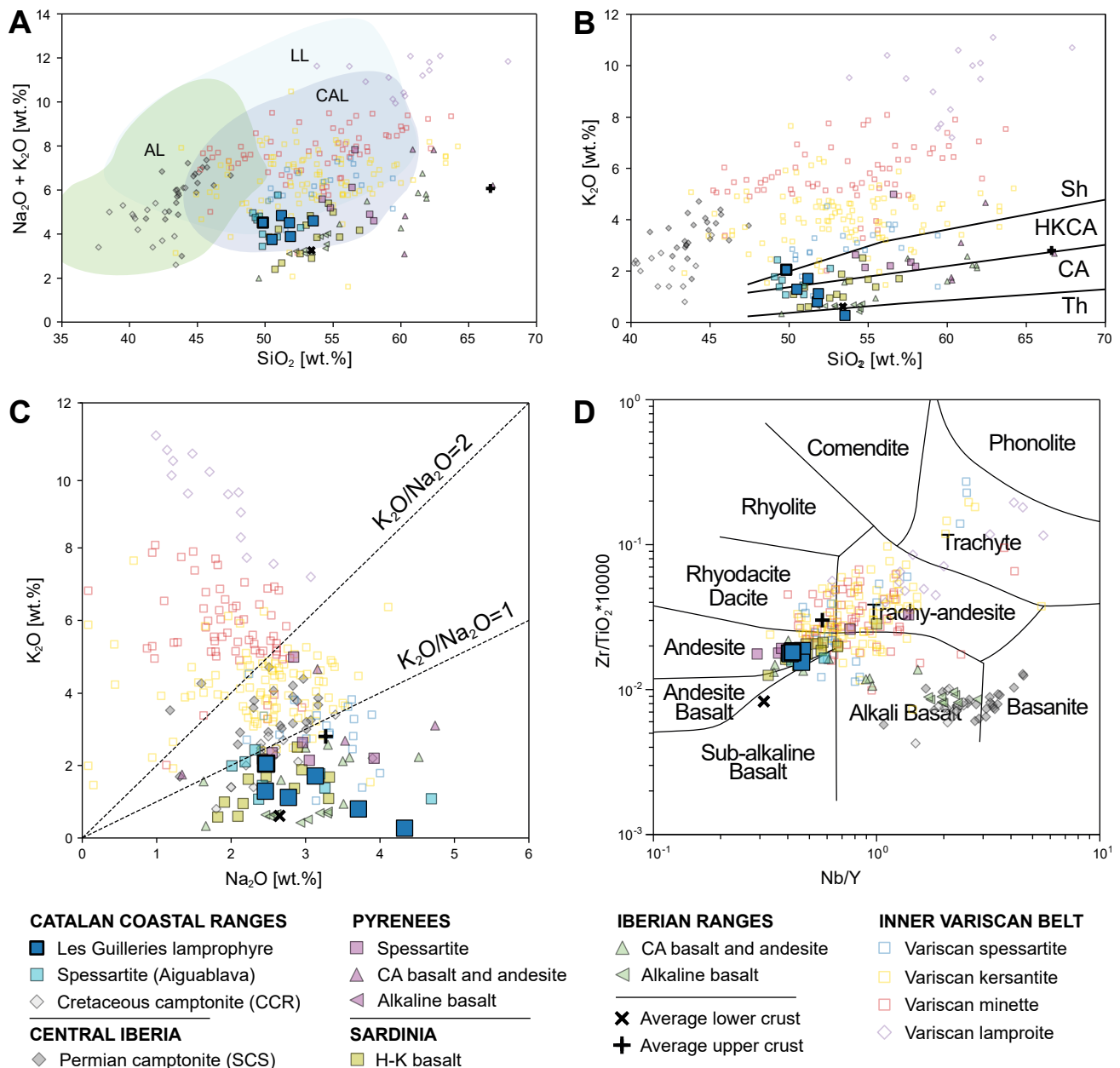
CATALAN COASTAL RANGES
■ Les Guilleries lamprophyre
■ Spessartite (Aiguablava)
◇ Cretaceous camptonite (CCR)

CENTRAL IBERIA
◆ Permian camptonite (SCS)

PYRENEES
■ Spessartite
▲ CA basalt and andesite
◀ Alkaline basalt

SARDINIA
■ H-K basalt

IBERIAN RANGES
△ CA basalt and andesite
◁ Alkaline basalt

✕ Average lower crust
✚ Average upper crust

INNER VARISCAN BELT
□ Variscan spessartite
□ Variscan kersantite
□ Variscan minette
◇ Variscan lamproite

FIGURE 3. A) $Na_2O + K_2O +$ vs. SiO_2 diagram of lamprophyre classification (fields after Rock, 1991). AL: alkaline lamprophyre. CAL: calc-alkaline lamprophyre. LL: lamproite. B) K_2O vs. SiO_2 classification diagram for orogenic magmatic rocks (Peccerillo and Taylor, 1976). Sh: shoshonite. HKCA: high-K calc-alkaline. CA: calc-alkaline. Th: tholeitic. C) K_2O vs. Na_2O showing that all LGL dykes have $K_2O/Na_2O <1$. D) Zr/TiO_2 vs. Nb/Y diagram (after Winchester and Floyd (1977)) in which LGL dykes plot in the fields of andesite to sub-alkaline basalt. Data sources: Aiguablava spessartites, Enrique (2009) and Ubide *et al.* (2010); Cretaceous camptonites from the Catalan Coastal Ranges (CCR), Ubide (2013); camptonites from the Spanish Central System, Orejana *et al.* (2008); spessartites from Maladeta (Pyrenees), Perini *et al.* (2004); high-K basaltic andesite dykes from Sarrabus (Sardinia), Ronca *et al.* (1999); Permian volcanic calc-alkaline andesites and alkaline basalts from eastern Pyrenees (Serra del Cadí, Innocent et al., 1994) and the south-eastern Iberian Ranges (Lago *et al.*, 2004; Lago *et al.*, 2012). Variscan spessartites, kersantites and minettes from the inner parts of the Variscan Belt are from: minettes, kersantites and spessartites from Vosges, Schwarzwald and Black Forest, Soder (2017); kersantites and spessartites from Erzgebirge in Bohemian massif, Seifert (2008); lamproites from Bohemian massif, Krmíček *et al.* (2015). Average lower and upper crust from Rudnick and Gao (2003).

Chondrite-normalized REE patterns also show similar fractionation for all dykes, independent of their alteration degree, with enrichments up to two orders of magnitude with respect to chondrite, enrichments in LREE with respect to Middle Rare Earth Elements (MREE) and HREE, and negative Eu anomaly (Fig. 4B). In spite of the

similarities, significant variations among LGL dykes show up for mobile elements and the highest differences occur for F, Ba, Sr, Cr, Zn, Ni, Rb, Pb and Cs concentrations. Figure 5 shows that Ba, Rb and Cs concentrations decrease with increasing Na_2O content. A similar trend is observed for Pb, Sr, Cr and Ni concentrations, although it is less

evident. On the other hand, Zn concentration increases with Na_2O (Fig. 5).

LGL dykes have major- and trace-element concentrations similar to the Aiguablava spessartites, but slightly more enriched in most HFSE and REE (Fig. 4A). With respect to other Variscan K-rich mafic dykes, the LGL dykes present lower enrichments in LILE, HFSE and REE in general, but within the ranges of variation of Variscan spessartites (Fig. 4A). LGL dykes also show major- and trace-element concentrations similar to high-K basaltic andesite dykes from Sardinia (Fig. 4A).

The plots of Figure 6 show that Variscan enriched mafic dykes show a wide variation in the concentration of several elements at similar MgO content, with clear differences between calc-alkaline (orogenic) and alkaline (anorogenic)

lamprophyres, as the later show higher TiO_2 and Fe_2O_3 content. LGL dykes cluster together with Aiguablava spessartites and high-K basaltic andesite dykes from Sardinia, showing characteristic high values of Al_2O_3, Fe_2O_3 and low values of K_2O and total REE, which are closer to average lower crustal values than spessartites, kersantites, minnetes and lamproites located in more internal positions within the Variscan belt (closer to the Rheic suture, here referred for simplicity as "Inner Variscan Belt"). LGL dykes also show Al_2O_3, CaO, Fe_2O_3, K_2O and LOI similar to some calc-alkaline basalts and andesites from Permian basins in the Eastern Pyrenees and Iberian Ranges, but with generally higher TiO_2, P_2O_5 and REE contents.

With respect to Variscan intrusives of the Catalan Coastal Batholith, LGL dykes have higher concentrations in K_2O, TiO_2, P_2O_5 and LOI at the same silica content, whereas in the rest of major-element concentrations, LGL dykes are similar
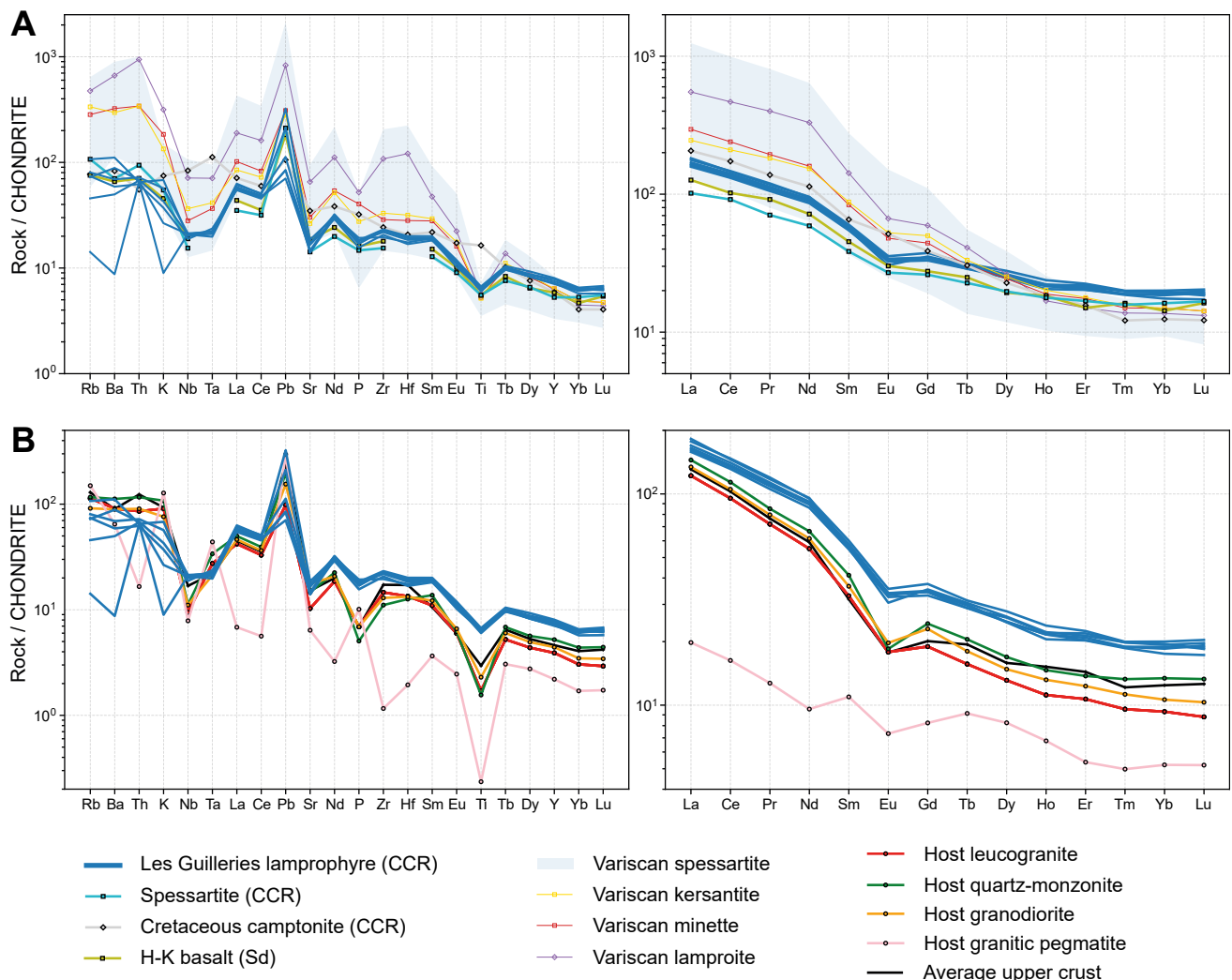
FIGURE 4. Primitive mantle-normalized trace element patterns (left) and chondrite-normalized REE patterns (right) of LGL dykes with respect to A) Variscan calc-alkaline lamprophyres and lamproites and host, B) Variscan granitoids. Median values are shown except for LGL dykes and the dark area represent the wide compositional variation of Variscan spessartites. Normalizing values of primitive mantle and chondrite from Sun and McDonough (1989) and McDonough and Sun (1995), respectively. Data sources as in Figure 3.

to those of gabbros from the appinite suits of Susqueda and Montnegre and fall within the known calc-alkaline trend of post-collisional Variscan magmatism in the CCR (Fig. 7).

Sr-Nd isotopes

Whole-rock Sr-Nd isotopic compositions of LGL dykes are presented in Table 2. $^{87}Sr/^{86}Sr_i$ values range from 0.708510 to 0.711272 ±0.000005, where the highest values are found in the most altered samples. $^{143}Nd/^{144}Nd$ ratios show a narrower range, between 0.512231 and 0.512246 ±0.000002, with calculated εNd_i from -5.23 to -4.63 (Fig. 8). Initial Sr-Nd isotopic compositions of LGL dykes plot within the ranges of variation of Variscan minnetes, kersantites and spessartites from Erzgebirge, Schwarzwald, Vosges and Pyrenees, with high $^{87}Sr/^{86}Sr_i$ and low εNd_i

CATALAN COASTAL RANGES
- Les Guilleries lamprophyre
- Spessartite (Aiguablava)
- Cretaceous camptonite (CCR)

CENTRAL IBERIA
- Permian camptonite (SCS)

PYRENEES
- Spessartite
- CA basalt and andesite
- Alkaline basalt

SARDINIA
- H-K basalt

IBERIAN RANGES
- CA basalt and andesite
- Alkaline basalt
- Average lower crust
- Average upper crust

INNER VARISCAN BELT
- Variscan spessartite
- Variscan kersantite
- Variscan minette
- Variscan lamproite

FIGURE 5. Trace element concentrations vs. Na$_2$O of LGL dykes showing the most mobile elements during alteration. Arrows point towards increasing albitization. Data sources as in Figure 3.

typical of variably enriched lithospheric mantle sources (Fig. 8A). In the ICS the isotopic composition of pyroxenitic and hornblenditic xenoliths overlap with the lamprophyre compositional fields, implying that the mantle beneath the ICS has a "two-pole composition": one pole is a depleted isotopic component with high εNd_i (3.5 to 7.1) and low $^{87}Sr/^{86}Sr_i$ (0.7029 to 0.7044); the second pole is an enriched lithospheric mantle with low εNd_i values (0.9 to 1.5) and relatively high $^{87}Sr/^{86}Sr_i$ (0.7043 to 0.7051) (Orejana *et al.*, 2006). LGL dykes show even higher $^{87}Sr/^{86}Sr_i$ (up to 0.7112) and lower εNd_i (-5.23 to -4.63), clustering together with high-K basalts from Sardinia, and Permian calc-alkaline volcanics from the Iberian Ranges and Eastern Pyrenees (Fig. 8A).
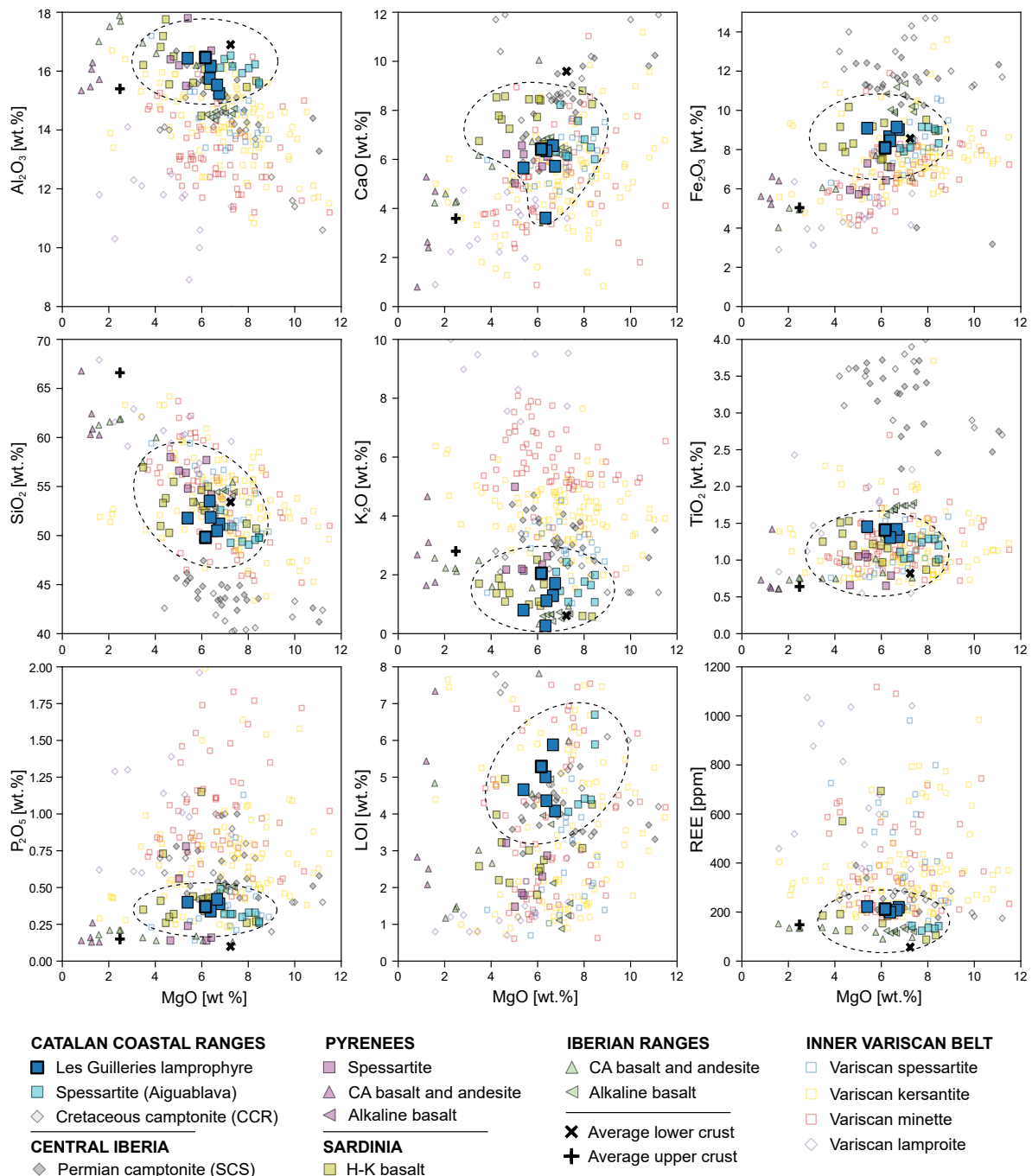
FIGURE 6. Major element constituents vs. MgO and total REE content of LGL dykes with respect to other Variscan lamprophyres and lamproites. The composition of LGL dykes is roughly similar to Aiguablava spessartites and high-K basalts from Sardinia in most elements. Dotted lines enclose the data from the Catalan Coastal Ranges and Sardinia. Data sources as in Figure 3.

Other SCLM domains in Western Europe present different Sr-Nd isotopic compositions in geochemically similar enriched mafic dykes. In southwest Britain, post-Variscan ultrapotassic lamprophyres emplaced north of a main boundary, fall on the mantle array, with εNd$_i$ ranging from -1 to +1.6, related to the Avalonia terrane, while those south of the boundary are enriched in radiogenic Sr, have initial εNd$_i$ values of -0.3 to +3.5, and are isotopically indistinguishable from similar-aged lamprophyres in Armorican massifs in Europe (Dijkstra and Hatch, 2018). Lamprophyres from Vosges and Black Forest show even lower εNd$_i$ values that overlap with LGL between -4 and -6, as well as the highest $^{87}Sr/^{86}Sr_i$ enrichments between 0.708 and 0.712. Soder (2017) found a boundary between Saxo-thuringian granitoids and lamprophyres with higher εNd$_i$ and lower $^{87}Sr/^{86}Sr_i$, and the Moldanubian granitoids and lamprophyres with lower εNd$_i$ and higher $^{87}Sr/^{86}Sr_i$ that cluster together with LGL dykes (Fig. 8B).

U-Pb ages in titanite

The lack of fresh phenocrysts, commonly used for lamprophyre dating, and the scarcity of zircons, make titanite and allanite from the matrix the only minerals suitable for dating. Allanite shows intense alteration and yields lower intercept dates with large uncertainties, therefore only titanite ages are taken into account. Additionally, only small crystals of titanite are present, so that it was not possible to obtain several spots from a single unzoned crystal. Therefore, the ages are an average of several titanite grains of up to 50μm in length. The only reliable ages obtained come from two variably altered dykes. The less altered dyke yielded the best results with lowest Mean Square Weighted Deviation (MSWD = 0.89) and concordia ages from Tera-Wasserburg diagram of 262±7Ma (mid to late Permian), while the most altered dyke yielded 255±17Ma with MSWD= 1.7 (Middle Permian to Middle Triassic; Fig. 9). Raw U-Pb data of titanite is presented in Table 3.

DISCUSSION

Petrographic classification and alteration

The similarities between all LGL dykes in terms of color, texture and mineral composition, as well as comparable HFSE, REE and some major-element contents (Figs. 3; 4) suggest that they formed from the same magmatic source. On the other hand, heteromorphism (differences in phenocrysts, microphenocrysts and matrix crystal sizes) coupled with similar chemistry of immobile elements suggests that dykes cooled at different rates and represent discrete low-volume pulses. But in spite of being discrete pulses, similarity in emplacement characteristics (orientation and space-filling features) suggests these pulses are close in time under the same tectonic regime. As secondary or alteration minerals are abundant and completely replace most phenocrysts and part of groundmass crystals, it is difficult to distinguish primary crystal features and evaluate processes of fractional crystallization and magma mixing. Nevertheless, as LGL dykes are similar to Aiguablava's spessartites, the observed fully chloritized phenocrysts probably correspond to clinopyroxene with minor amphibole and olivine, as Aiguablava's. This would explain the moderate MgO, Cr, and Ni concentrations, which are common in mantle-derived rocks. The occurrence of chloritized mafic phenocrysts of comparable sizes and shapes in dykes with different cooling rates (Fig. 2A-F), suggests that the phenocrysts did not crystalize during the late stage cooling but may have formed during either previous periods of stagnation or by mixing with another magma carrying these phenocrysts.

The principal criteria of lamprophyre classification is based on the relative abundance of primary mica and amphibole phenocrysts (Le Maitre et al., 2002), which appear chloritized in LGL dykes, and of plagioclase and K-feldspar, which are strongly modified by the alteration. Thus, alteration obliterates the primary composition and blurs the mineralogical classification. Nevertheless, the predominance of amphibole in the matrix, the predominance of primary plagioclase and the calc-alkaline geochemical affinity point towards a classification as spessartites.

TABLE 2. Whole-rock Sr and Nd isotopic data of LGL dykes. Initial $^{87}Sr/^{86}Sr$ and εNd were calculated at 262Ma using $\lambda^{87}Rb=1.42E^{-11}$ y^{-1} and $\lambda147Sm=6.54E^{-12}$ y^{-1}, $^{147}Sm/^{144}Nd_{CHUR}=0.1967$, and $^{143}Nd/^{144}Nd_{CHUR}= 0.512638$, respectively

	Dyke 1	Dyke 2	Dyke 3	Dyke 4	Dyke 5
Rb	68	51	29	9	47
Sr	391	295	360	296	349
$^{87}Sr/^{86}Sr$	0.711277±5	0.710588±3	0.710924±4	0.711628±3	0.710086±5
$^{87}Sr/^{86}Sr_i$	0.709242	0.708565	0.709982	0.711272	0.708510
Sm	8.58	8.32	8.9	8.22	8.09
Nd	41.7	43.7	43.4	40.7	39.3
$^{143}Nd/^{144}Nd$	0.512238±1	0.512249±1	0.51224±1	0.512232±1	0.512246±2
εNd$_i$	-5.18	-4.63	-5.14	-5.23	-5.04
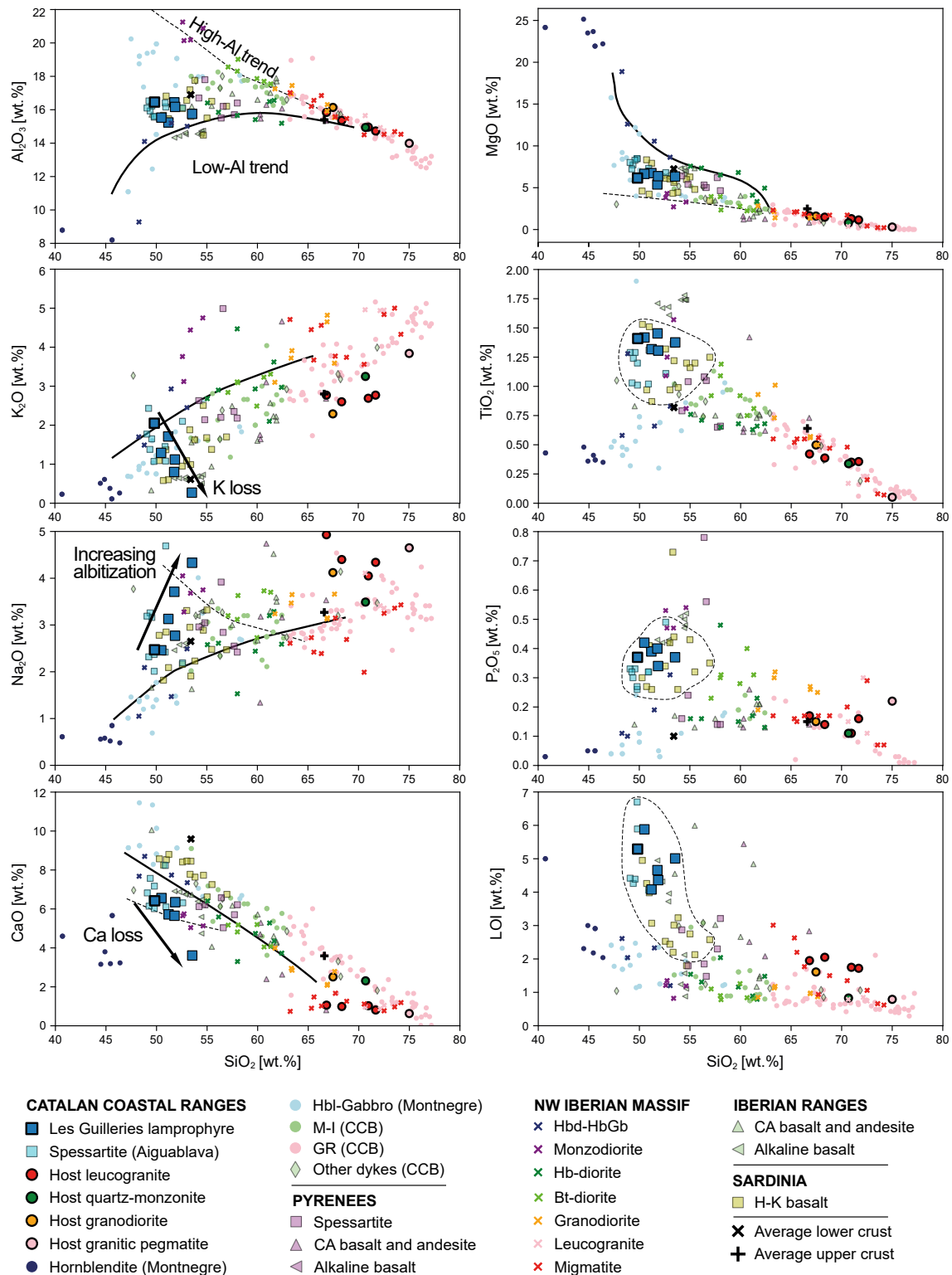
FIGURE 7. Harker variation diagrams showing LGL dykes major element trends with respect to host granitoids and rocks from the Catalan Coastal Batholith (Enrique, 1990). Comparison with appinite suits of the Sanabria complex in NW Iberia (Castro *et al.,* 2003) is provided. Lines show the main trends defined by Castro *et al.* (2003): a high-Al trend (dashed line) and a low-Al trend (continuous line). The high-Al trend links monzodiorites and Bt-diorites with tonalites, granodiorites and migmatites. The low-Al trend links Hb-gabbros and Hb-diorites. The two trends converge at silica contents of 63wt% for most elements. LGL dykes, Aiguablava spessartites and high-K basalts from Sardinia plot between these two trends, with commonly higher K_2O, TiO_2, P_2O_5 and LOI at the same silica content. Data sources as in Figure 3. M-I: mafic and intermediate igneous rocks. GR: syn to post collisional Variscan granitoids. Hbd-Gabbro: Hornblendite and horndblende gabbros.

TABLE 3. Titanite U-Pb data of measured ratios corrected for common Pb

Sample	$^{207}Pb/^{235}U$	2σ	$^{206}Pb/^{238}U$	2σ	rho	$^{238}U/^{206}Pb$	2σ	$^{207}Pb/^{206}Pb$	2σ	rho	$^{208}Pb/^{232}Th$	2σ
GI7-Ttn1	2.35	0.13	0.0590	0.0018	0.73	16.95	0.53	0.2924	0.0113	0.50	0.0272	0.0014
GI7-Ttn2	6.43	0.15	0.0907	0.0020	0.61	11.03	0.24	0.5113	0.0116	0.56	0.1490	0.0082
GI7-Ttn3	2.91	0.35	0.0641	0.0033	0.14	15.60	0.79	0.3260	0.0405	0.32	0.0352	0.0038
GI7-Ttn4	5.57	0.38	0.0880	0.0036	0.55	11.36	0.46	0.4670	0.0286	0.48	0.0628	0.0092
GI7-Ttn5	9.39	0.80	0.1225	0.0069	0.71	8.16	0.46	0.5380	0.0309	0.34	0.1530	0.0911
GI7-Ttn6	13.48	0.40	0.1502	0.0036	0.84	6.66	0.16	0.6503	0.0153	0.47	0.2130	0.0118
GI7-Ttn7	10.87	0.96	0.1313	0.0095	0.86	7.62	0.55	0.5980	0.0295	0.41	0.4100	0.2801
GI7-Ttn8	7.90	1.41	0.1040	0.0102	0.90	9.62	0.94	0.5110	0.0461	0.52	0.1270	0.0401
GI7-Ttn9	11.72	0.75	0.1387	0.0103	0.82	7.21	0.53	0.6050	0.0278	0.28	0.0630	0.0121
GI7-Ttn10	13.20	1.13	0.1493	0.0096	0.95	6.70	0.43	0.6400	0.0263	0.60	0.2040	0.0611
GI7-Ttn11	13.50	1.33	0.1530	0.0114	0.94	6.54	0.49	0.6580	0.0239	0.53	0.3300	0.1202
GI7-Ttn12	13.98	0.69	0.1599	0.0052	0.18	6.25	0.20	0.6240	0.0307	0.40	0.0920	0.0102
GI7-Ttn13	18.00	1.54	0.1930	0.0126	0.96	5.18	0.34	0.6770	0.0217	0.61	0.1830	0.0213
GI7-Ttn14	8.63	0.97	0.1136	0.0083	0.22	8.80	0.64	0.5560	0.0808	0.38	0.1500	0.1600
GI7-Ttn15	24.75	0.53	0.2479	0.0056	0.58	4.03	0.09	0.7254	0.0160	0.50	0.2410	0.0129
GI7-Ttn16	24.40	1.20	0.2413	0.0110	0.92	4.14	0.19	0.7320	0.0183	0.50	0.3510	0.0973
GI7-Ttn17	23.79	0.85	0.2406	0.0075	0.23	4.16	0.13	0.7150	0.0262	0.52	0.2700	0.0553
GI7-Ttn18	12.40	1.82	0.1510	0.0133	0.56	6.62	0.59	0.5950	0.0700	0.32	0.2730	0.0932
GI7-Ttn19	26.50	2.36	0.2610	0.0187	0.94	3.83	0.28	0.7290	0.0325	0.25	0.2380	0.0472
GI7-Ttn20	34.30	1.38	0.3340	0.0155	0.91	2.99	0.14	0.7500	0.0192	0.44	0.6300	0.1804
GI7-Ttn21	35.70	1.94	0.3410	0.0156	0.95	2.93	0.13	0.7510	0.0180	0.43	0.2900	0.0306
GI7-Ttn22	32.50	4.15	0.3150	0.0326	0.99	3.17	0.33	0.7450	0.0266	0.63	0.1200	0.0113
GI7-Ttn23	35.20	1.57	0.3350	0.0129	0.94	2.99	0.11	0.7630	0.0188	0.32	0.3150	0.0258
GI7-Ttn24	38.20	1.77	0.3600	0.0157	0.98	2.78	0.12	0.7652	0.0169	0.55	0.3950	0.0575
GI7-Ttn25	36.00	8.83	0.3240	0.0653	1.00	3.09	0.62	0.7420	0.0265	0.36	0.2590	0.0453
GI7-Ttn26	41.20	3.01	0.3790	0.0252	0.98	2.64	0.18	0.7860	0.0198	0.32	0.5000	1.0000
GI7-Ttn27	45.59	1.03	0.4266	0.0097	0.90	2.34	0.05	0.7773	0.0163	0.36	0.5990	0.0398
GI7-Ttn28	45.70	1.59	0.4260	0.0147	0.94	2.35	0.08	0.7776	0.0172	0.40	0.1629	0.0054
GI7-Ttn29	45.50	1.67	0.4260	0.0147	0.95	2.35	0.08	0.7810	0.0174	0.32	0.2319	0.0085
GI7-Ttn30	43.30	7.55	0.4040	0.0635	1.00	2.48	0.39	0.7740	0.0253	0.59	0.7300	0.3703
GI7-Ttn31	47.20	2.58	0.4360	0.0227	0.95	2.29	0.12	0.7828	0.0178	0.60	0.2014	0.0099
GI7-Ttn32	47.60	2.68	0.4430	0.0219	0.95	2.26	0.11	0.7770	0.0203	0.43	0.4130	0.0645
GI7-Ttn33	52.90	5.50	0.4820	0.0509	0.99	2.07	0.22	0.8019	0.0186	0.18	0.7000	0.2204
GI7-Ttn34	54.10	2.10	0.5020	0.0189	0.88	1.99	0.07	0.7810	0.0185	0.28	0.6950	0.0871
GI7-Ttn35	53.40	8.17	0.4920	0.0677	0.99	2.03	0.28	0.7900	0.0240	0.61	0.7700	0.4902
GI7-Ttn36	64.10	4.11	0.5740	0.0407	0.93	1.74	0.12	0.8120	0.0265	0.39	0.7400	0.2804
GI7-Ttn37	70.20	2.13	0.6300	0.0188	0.95	1.59	0.05	0.8128	0.0172	0.31	0.5780	0.0397
GI7-Ttn38	71.10	3.78	0.6280	0.0316	0.97	1.59	0.08	0.8179	0.0186	0.57	0.5900	0.3402
GI7-Ttn39	89.80	2.69	0.8090	0.0228	0.96	1.24	0.03	0.8087	0.0170	0.30	1.3500	0.1820
GI7-Ttn40	94.80	4.61	0.8380	0.0452	0.96	1.19	0.06	0.8120	0.0196	0.48	1.4000	1.3003

The replacement of primary magmatic phases by secondary minerals typical of greenschist-facies metamorphism (calcite, chlorite and epidote) is a ubiquitous feature in many lamprophyres (Rock, 1991). This is sometimes understood as autometasomatic processes upon solidification of melts with high volatile content (Rock, 1991). In LGL dykes the calcite-chlorite-epidote paragenesis occurs together with albite and hematite (Fig. 3H). Moreover, there is a systematic variation in Na$_2$O, SiO$_2$, K$_2$O, CaO, F, Ba, Rb, Cs, Pb, Sr and Zn (Fig. 5) with the abundance of albite, chlorite, hematite, titanite, and their replacement textures (Fig. 2). Similar precipitation of minute hematite crystals and albitization of plagioclases have been observed in late-Variscan granitoids of the extended Montseny-Guilleries Massif (Fàbrega *et al.*, 2019), Paleozoic rocks of the Variscan Morvan Massif in France (Parcerisa *et al.*, 2010) and host granitoids from this study. Therefore, one or more post-magmatic processes of alteration must have affected LGL dykes additionally to common autometasomatic processes. The anomalously low concentration of K$_2$O and K$_2$O/Na$_2$O ratios in LGL dykes with respect to lamprophyres from other massifs (Fig. 3C), seem to occur also in Aiguablava spessartites, according to the published geochemical data (Enrique, 2009; Ubide *et al.*, 2010), which suggests albitization was a common process across the CCR in contrast to other Variscan domains. Recent studies have suggested that an albitization event developed under low-temperature subsurface conditions previous to erosion that led to the Lower Triassic paleosurface (Fàbrega *et al.*, 2019; Parcerisa *et al.*, 2010). Additionally, the elements that may have been remobilized by the albitization (Ba, F, Pb, Zn) in Les Guilleries are concentrated in epigenetic vein mineralizations nearby (Osor fluorite-barite-sphalerite-galena veins). As this mineral deposit is related to hydrothermal fluid circulation, the same hydrothermal event could have been responsible for the alteration of LGL dykes, although it is still not clear if there is a direct relationship between the lamprophyres and fluorite deposits.

Age of emplacement

From field observations, LGL dykes are younger than all late-Variscan syn-post collisional plutons of Les Guilleries and nearby massifs with ages ranging from 323.6±2.8Ma to 284±3Ma (Martínez *et al.*, 2008; Solé *et al.*, 2002). The new U-Pb titanite MSDW age of 262±7Ma is in agreement with the crosscutting relationships, although this age may be skewed towards younger ages due to the influence of secondary titanite related with post-magmatic alteration. Additionally, late crystallization and post magmatic events are known to yield up to 19Myr younger U-Pb ages in titanite than early crystallizing zircons in Variscan granites (Broska and Petrík, 2013). This suggests that LGL dyke emplacement may be slightly older than matrix titanite crystallization at 262±7Ma, but younger than the most felsic magmatism. An approximate E-W orientation of LGL dykes with gentle N-dipping and emplacement along fractures and diaclases are similar to what is observed in Aiguablava's spessartites intruded in ca. 288Ma pluton, and considering the geochemical similarities, both dyke swarms may have resulted from related events.

Relation with appinite suites of the Catalan Coastal Batholith

The REE parallel profiles of LGL dykes and their host rocks (Fig. 4B) suggest they have a common source and are related by fractionation processes (*e.g.* Fowler and Henney, 1996), which is common of appinite suites (Murphy, 2013). Indeed, the Catalonian Coastal Batholith plutonic and hypabyssal association forms a very complete post-collisional calc-alkaline igneous suite (Enrique, 1990; Martínez *et al.,* 2008; Figure 7). The suite's ultrabasic-basic to intermediate rocks, with olivine hornblendites, hornblende melanogabbros-gabbros and leucogabbros, are associated with late-Variscan calc-alkaline granites in the Susqueda complex and Montnegre Massif, that have been interpreted as appinite suites (Butjosa *et al.,* 2013; Galán *et al.,* 2017). The most acidic rocks of the suite are hornblende-biotite quartz diorites and monzodiorites. Although the evolutionary trend of this association is calc-alkaline, the hornblendites and the leucogabbros are thought to be derived from basic magmas enriched in K, whereas quartz diorites are considered hybrid rocks, generated by mixing of basic and felsic magmas (Butjosa *et al.,* 2013). The mineralogical and geochemical characteristics of LGL dykes match those of the hypothesized basic parental magmas of the appinite suite, an amphibole-phlogopite-bearing melt with high potassium and high fluid content (Fig. 7). Therefore, the LGL dykes probably represent the least modified magmas from the SCLM beneath the CCR during Variscan times to reach crustal levels, along lithospheric-scale deep transcurrent faults, and could represent one of the deepest sources of heat and material of the Variscan-post-collisional magmatism. The lamprophyre magmas could have transferred fluids as well as LILE (K, Ba, Rb, Cs, Pb, Th), HFSE (Ti, P, Zr, Nb) and REE from the metasomatized lithospheric mantle to the crust, and thus probably played a significant role in crustal melting and formation of mineral resources.

The relationship between appinites and calc-alkaline lamprophyres has long been recognized (Rock, 1991). Examples of hornblendites related to granitoids and/or migmatites exist in the Iberian Massif, Pyrenees and other Variscan terranes in the context of large scale dextral strike-slip tectonics produced by the interaction between Laurassia and Gondwana, and coeval lamprophyre dykes are present in all this places (Bea *et al.*, 1999; Castro *et al.*, 2003; Roberts *et al.*, 2000; Scarrow *et al.*, 2009).

Source characteristics and melting conditions

The Th/Yb vs. Nb/Yb ratios (Fig. 10A) are usually interpreted to reflect source composition and/or crustal assimilation (Pearce *et al.*, 2008), where subduction processes and crustal contamination usually result in an enrichment of Th with respect to Nb. The significantly high Th/Yb ratio for the most basic LGL sample, with 49.82% SiO_2, is unlikely to be explained only by crustal contamination, and probably reflects the extent of metasomatism during Variscan and/or older subduction events in the SCLM source. This is also consistent with Sr-Nd isotopic variations reflecting an enriched lithospheric mantle source with high $^{87}Sr/^{86}Sr_i$ and low

εNd_i (Fig. 8), although mixing with small proportions of crustal magmas or fluids cannot be discarded, as deduced by the presence of xenocrysts and hybridization textures. Ratios between Rb, Ba and Sr are commonly used to discriminate phlogopite vs. amphibole rich sources, which is not possible for LGL dykes as those elements have been remobilized by post-magmatic processes. However, the predominance of amphibole over phlogopite in most mafic lithologies is a common feature of appinite rocks from the CCR. Additionally, the ratios between LREE and HREE in LGL dykes could be explained by an amphibole lherzolite mantle source with a combination of spinel and garnet as aluminum phases. This is observed in the diagram of Figure 10B, C, where garnet-compatible Yb is compared with La, Sm and Gd-garnet incompatible elements (Rollinson, 1993). Additionally, the Sm/Yb vs. La/Sm diagram (Fig. 10C; Jung *et al.,* 2006) also shows that a spinel and garnet lherzolite around 2% degree of melting could explain the observed ratios.

Integrating the above results, major, trace- and rare-earth-element ratios suggest that the LGL magma source was probably an enriched SCLM with the composition of an amphibole-bearing spinel-garnet lherzolite that underwent low degrees of partial melting. Similar sources have been proposed for post-collisional spessartites across the Variscan Belt in the Bohemian Massif, Vosges and Black Forest (Soder, 2017). However, lamprophyre dyke swarms related to the inner parts of the orogenic belt show a wide variety of lamprophyre types with higher LILE, HSFE, REE enrichments (Fig. 3; 6), being the most extreme examples the lamproites and peralkaline minnetes from the Bohemian Massif and Black Forest, respectively, that formed from very low degree melting of enriched domains (Krmíček *et al.,* 2015; Soder, 2017), not observed in the CCR. Figure 11 shows there is a compositional continuum between high-K lamproites and low-K gabbros revealing different degrees of metasomatism in Variscan SCLM, variable melting conditions and complex differentiation stories. LGL dykes and high-K basaltic andesitic dykes from Sardinia represent moderately enriched SCLM in LILE, HFSE and REE closer to lower crustal values in most elements than most enriched species of the inner Variscan belt (Figs. 3; 6; 11). Although there is still few isotopic data to define precise lithospheric domains, the striking geochemical similarities between CCR and Sardinia's mafic dykes with respect to dykes from other Variscan domains strongly suggest they come from a similar and compositionally unique domain of the Variscan SCLM, different from other parts of the Variscan Belt of western Europe. However, it is still not clear whether these geochemical features are related to the nature and source of the subducted continental material and/or conditions of partial melting and the nature of residual phases.
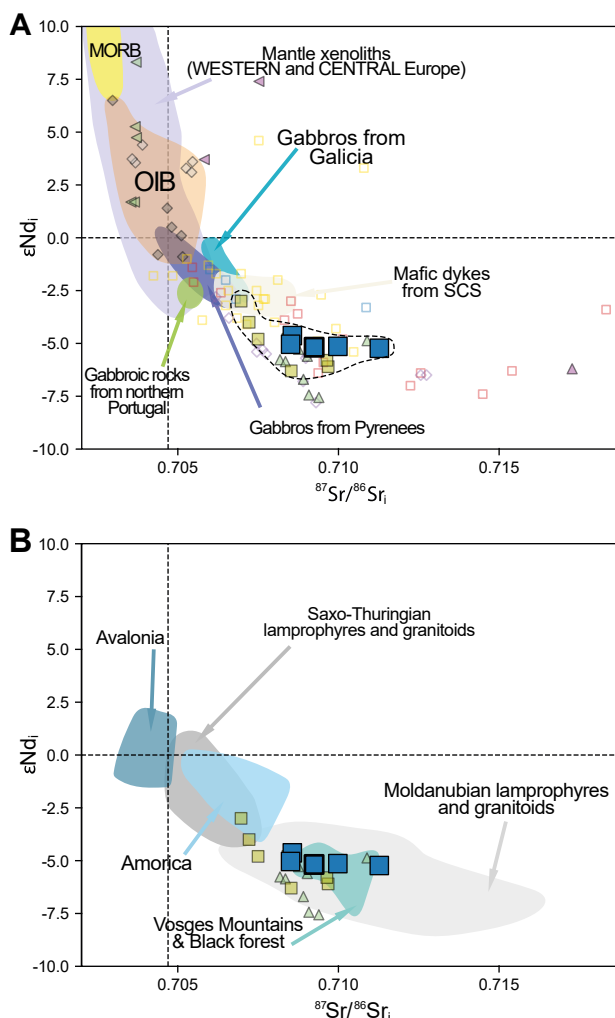

FIGURE 8. Initial Sr–Nd isotopic compositions of LGL dykes at 262Ma. Isotopic compositions of post-collisional A) Variscan mafic rocks and previously defined B) Variscan SCLM domains are shown for comparison. Dashed lines represent Bulk Earth isotopic ratios from DePaolo (1980). Data sources as in Figure 3 except for Avalonia and Amorica Massifs that are from Dijkastra and Hatch (2018) and references therein. Saxo-thuringian and Moldanubian domains in B are from Soder (2017). Note that LGL dykes cluster with high-K basalts from Sardinia and Permian andesites from the Iberian Ranges, suggesting a common SCLM source.

REGIONAL CORRELATIONS

Post-collisional magmatism in NE Iberia happened several tens of million years after the main Variscan tectono-metamorphic event related to the Rheic suture in the Inner Variscan Belt, during Late Devonian to Early Carboniferous (Wilson *et al.*, 2004). Most calc-alkaline lamprophyre dykes in the Inner Variscan belt are older than LGL dykes, with ages that range from Early Carboniferous to Early Permian (Seifert, 2008; Soder, 2017). However, calc-alkaline lamprophyre dykes with younger Permian ages and geochemistry similar to the one of LGL dykes are also present in this area (e.g. Western Carpathians, 259.0±2.8Ma, spessartites, Spišiak *et al.*, 2019; Bohemian massif, kersantites and spessartites, Seifert, 2008). This suggests that these Mid to Late Permian calc-alkaline lamprophyres occurred in domains with similar characteristics with respect to the architecture of the Variscan Belt under a strike-slip regime previous to the extensional post-orogenic regime (Debon and Zimmermann, 1993).

The age obtained in this study is also similar to a Rb-Sr biotite age of 259±3Ma from a calc-alkaline basaltic andesite dyke from the Sarrabus batholith in Sardinia, where mafic dykes cross cut 290 to 270Ma metaluminous and peraluminous rhyolitic products. This age points to some mafic magmatism intruding after the felsic magmatism (Ronca *et al.*, 1999), similar to what is observed in the CCR. This age also indicates that the change from a calc-alkaline (orogenic) to an alkaline (anorogenic) signature in post-collisional magmatism, related to the transition from the first to the second cycle as defined by Cortesogno *et al.* (1998), did not occur before 262±7Ma in the CCR.

Such change from orogenic calc-alkaline to anorogenic alkaline magmatism is also present in lamprophyre dykes from the western Pyrenees (Debon and Zimmermann, 1993) and Sardinia (Bonin, 1987), as well as in volcanic rocks from Permian pull-apart basins of the Iberian Ranges and eastern Pyrenees, which occurred from Early Permian to Late Permian-Triassic (Arche and López-Gómez, 1996; Innocent *et al.*, 1994). In summary, the calc-alkaline signature of LGL dykes represent the latest stage in the evolution from Early Permian strike-slip tectonics (associated or not with a Paleotethys subduction environment, Pereira *et al.*, 2014; Perini *et al.*, 2004) to Late Permian extension associated with the Neotethys opening.

CONCLUSIONS

Les Guilleries lamprophyre dykes constitute a mostly vertical dyke swarm that intrudes late Carboniferous to early Permian granitoids and lower Paleozoic metasediments of the Catalan Coastal Ranges.

The predominance of mafic phenocrysts, porphyritic texture, high MgO and volatile content, together with crustal-like trace-element patterns indicate that LGL dykes correspond to calc-alkaline lamprophyres, probably spessartites. The parallel REE pattern of lamprophyres and host rocks indicates a common magmatic source.

The geochemical characteristics of LGL dykes (enrichments in LILE, HFSE and REE) is a feature shared with the calc-alkaline lamprophyres from the CCR

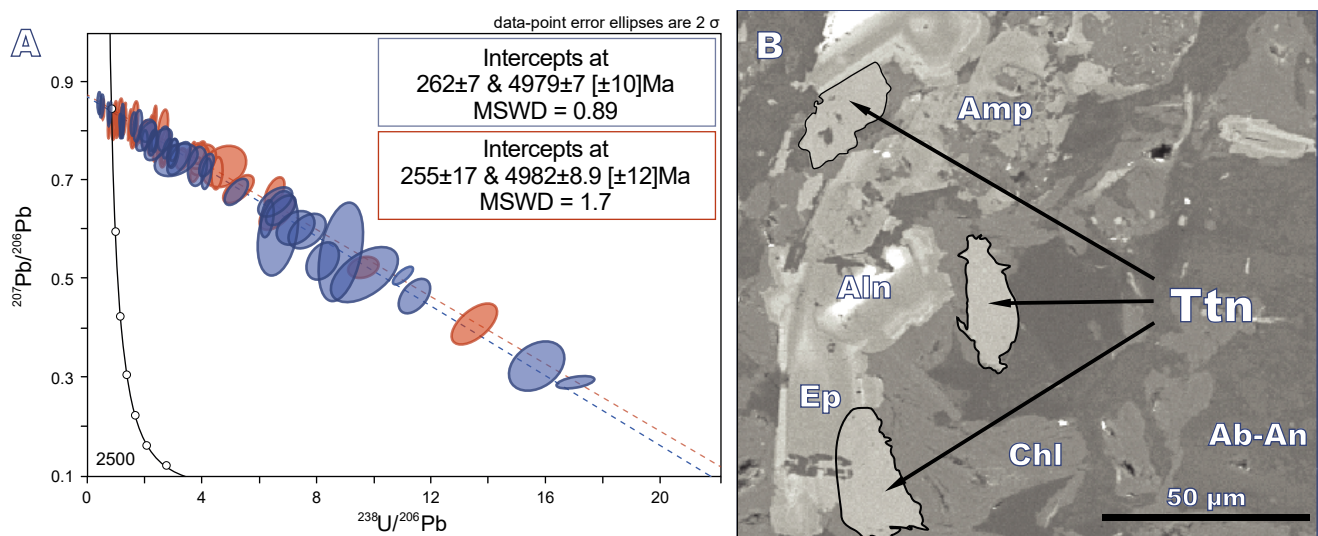**FIGURE 9.** A) Titanite Tera-Wasserburg concordia diagram using measured $^{207}Pb/^{206}Pb$ and $^{238}U/^{206}Pb$ ratios corrected for common Pb, with the data conversion performed by Isoplot 3.7. Titanite data from the two samples are plotted at 2σ and uncertainties on lower intercept ages are 95% confidence. B) BSE images showing examples of analyzed titanite crystals.
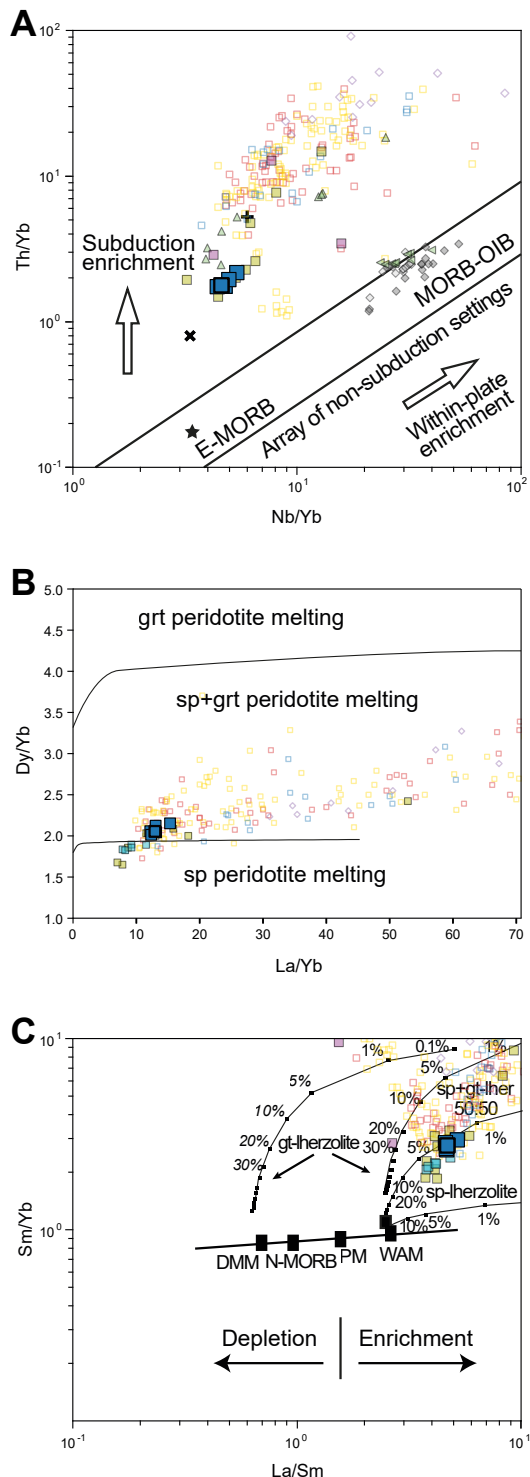
FIGURE 10. A) Nb/Yb vs. Th/Yb plot (after Pearce, 2008) suggesting LGL mantle source enrichment from subduction episodes. B) La/Yb vs. Dy/Yb plot suggesting LGL generation at shallow depth in spinel+garnet-peridotite stability field near the boundary of pure spinel-peridotite stability field (after Jung *et al.*, 2006). C) La/Sm vs. Sm/Yb plot showing partial melting curves for a spinel-lherzolite and a garnet-lherzolite (Aldanmaz *et al.* (2000) and references therein) mantle. REE ratios of LGL dykes fit the field around 2% degree of melting in a spinel+garnet lherzolite at 50:50 proportion. DMM: Depleted Mantle. PM: Primitive Mantle. WAM: Western Anatolian Mantle. Data sources and symbols as in Figure 3.

(Aiguablava) and high K-basalts from Sardinia, as well as Permian calc-alkaline andesites from the eastern Pyrenees and Iberian Ranges.

High $^{87}Sr/^{86}Sr$ and low $^{143}Nd/^{144}Nd$ isotope ratios suggest an enriched subcontinental lithospheric mantle source similar to what is found in post-collisional K-rich mafic dykes from Sardinia, Permian calc-alkaline andesites from Iberian Ranges and other defined Variscan terranes like the Moldanubian domain.

The intrusion of LGL dykes occurred during Permian times, as reflected in the U-Pb ages of matrix titanite crystals that yield concordia ages of 262±7Ma. Mafic rocks from Sardinia have similar age and probably shared a similar SCLM.

The emplacement of LGL dykes was controlled by secondary faults of the main NW-SE strike-slip dextral system that emplaced the granitoids during the post-collisional evolution. Thermal relaxing and lithospheric thinning after the Variscan continental collision allowed the emplacement of mantle-derived magmas at upper crustal levels in small volume short-lived magmatic pulses.

Post-magmatic processes of chloritization and albitization affected the lamprophyres causing the systematic variations of Na_2O, SiO_2, K_2O, CaO, F, Ba, Rb, Cs, Pb, Sr, Tl, and Zn. They are also shared with granitoid host rocks, so that albitization must be unrelated to magmatic processes and may have occurred during early Triassic times, by comparison with other albitized rocks of the Catalan Variscan domain.

The calc-alkaline signature of LGL dykes marks them as the latest Variscan magmatism event, which is related to the Early Permian strike-slip tectonics, before the Late Permian extension associated with the Neotethys opening and anorogenic alkaline magmatism.

ACKNOWLEDGMENTS
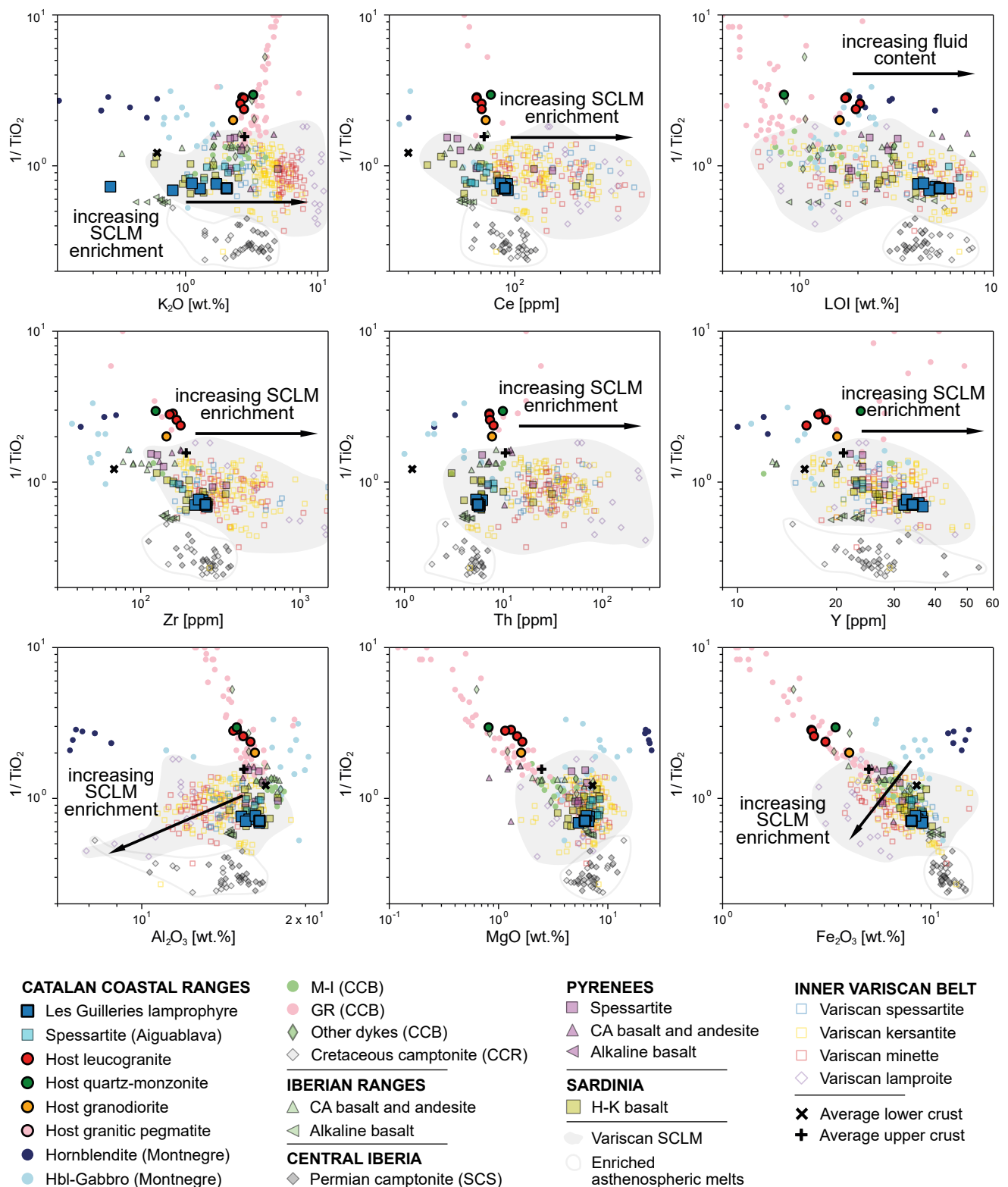
FIGURE 11. Plots of 1/TiO$_2$ vs. various elements showing major compositional end-members of Variscan magmatism in the Catalan Coastal Ranges and adjacent Paleozoic massifs. Calc-alkaline lamprophyres and lamproites define heterogeneous SCML enrichment in different parts of Western Europe, while alkaline lamprophyres represent the influence of enriched asthenospheric OIB melts in the SCML. Note that LGL dykes are compositionally similar to Aiguablava spessartites and high-K basalts from Sardinia in most elements. Data sources as in Figure 3.

REFERENCES

Aldanmaz, E., Pearce, J., Thirlwall, M., Mitchell, J.G., 2000. Petrogenetic evolution of late Cenozoic, post-collision volcanism in western Anatolia, Turkey. Journal of Volcanology and Geothermal Research, 102, 67-95.

Arche, A., López-Gómez, J., 1996. Origin of the Permian-Triassic Iberian Basin, central-eastern Spain. Tectonophysics, 266, 443-464.

Awdankiewicz, M., 2007. Late Paleozoic lamprophyres and associated mafic subvolcanic rocks of the Sudetes (SW Poland): petrology, geochemistry and petrogenesis. Geologia Sudetica, 39, 11-97.

Ayora, C., Soler, A., Melgarejo, J.C., 1990. The Hercynian ore deposits from the Catalonian Coastal Ranges. Acta Geologica Hispanica, 25, 65-73.

Bea, F., Montero, P., Molina, J.F., 1999. Mafic precursors, peraluminous granitoids, and late lamprophyres in the Avila batholith: A model for the generation of Variscan batholiths in Iberia. Journal of Geology, 107, 399-419.

Bonin, B., 1987. From orogenic to anorogenic magmatism: a petrological model for the transition calc-alkaline-alkaline complexes. Revista Brasileira de Geociencias, 17(4), 366-371.

Broska, I., Petrík, I., 2014. Accessory phases in the genesis of the igneous rocks. In: Kumar, S., Singh, R.N. (eds.). Modelling of Magmatic and Allied Processes, 109-149. DOI: 10.1007/978-3-319-06471-0_6

Bussy, F., Hernandez, J., Von Raumer, J., 2000. Bimodal magmatism as a consequence of the post-collisional readjustment of the thickened Variscan continental lithosphere (Aiguilles Rouges-Mont Blanc Massifs, Western Alps). Earth and Environmental Science Transactions of the Royal Society of Edinburgh, 91(1-2), 221-233.

Butjosa, L., Enrique, P., Galán, G., 2013. Las hornblenditas, gabros y dioritas del Macizo del Montnegre (Barcelona, Cordilleras Costero Catalanas). Geogaceta, 54, 35-38.

Campá-Viñeta, J.A., Montoriol-Pous, J., 1974. Mineralogénesis del yacimiento de Osor (Gerona). Acta Geologica Hispanica, 4, 139-141.

Castro, A., Corretgé, L.G., de la Rosa, J.D., Fernández, C., López, S., García-Moreno, O., Chacón, H., 2003. The appinite-migmatite complex of Sanabria, NW Iberian Massif, Spain. Journal of Petrology, 44, 1309-1344.

Cortesogno, L., Cassinis, G., Dallagiovanna, G., Gaggero, L., Oggiano, G., Ronchi, A., Seno, S., Vanossi, M., 1998. The Variscan post-collisional volcanism in Late Carboniferous Permian sequences of Ligurian Alps, Southern Alps and Sardinia (Italy): a synthesis. Lithos, 45(1), 305-328.

Debon, F., Zimmermann, J.L., 1993. Mafic dykes from some plutons of the Western Pyrenean Axial Zone (France, Spain): markers of the transition from Late-Hercynian to early Alpine events. Schweizerische Mineralogische und Petrographische Mitteilungen, 73, 421-433.

DePaolo, D.J., 1980. Crustal growth and mantle evolution: inferences from models of element transport and Nd and Sr isotopes. Geochimica et Cosmochimica Acta, 44(8), 1185-1196.

Dijkstra, A.H., Hatch, C., 2018. Mapping a hidden terrane boundary in the mantle lithosphere with lamprophyres. Nature Communications, 9, 1-8. DOI: 10.1038/s41467-018-06253-7

Durán, H., 1985. El Paleozóico de les Guilleries. Doctoral Thesis. Bellaterra (Spain), Universitat Autònoma de Barcelona, 243pp.

Durán, H., 1990. El Paleozoico de les Guilleries. Acta Geologica Hispanica, 25, 83-103.

Elter, F.M., Corsi, B., Cricca, P., Muzio, G., 2004. The south-western Alpine foreland: correlation between two sectors of the Variscan chain belonging to 'stable Europe': Sardinia (-) Corsica and the Maures Massif (south-eastern France). Geodinamica Acta, 17, 31-40.

Enrique, P., 1990. The Hercynian intrusive rocks of the Catalonian Coastal Ranges (NE Spain). Acta Geologica Hispanica, 25, 39-64.

Enrique, P., 2009. Las espesartitas, camptonitas y bostonitas del complejo intrusivo de Aiguablava (Cadenas Costeras Catalanas): Cartografía y composición. Geogaceta, 47, 125-128.

Esteve, S., Sunyer, J., Culí, L., Cirés, J., Alías, G., 2016. El complejo intrusivo diorítico-gabroico de Susqueda (Macizo del Montseny-Guilleries, Cataluña): unidades litológicas y características petrográficas. Geogaceta, 60, 99-102.

Esteve, S., Enrique, P., Alías, G., 2018. Relaciones intrusivas y cronología relativa del plutón básico de Susqueda con las rocas metamórficas encajantes (Cordillera Prelitoral Catalana). Geogaceta, 63, 107-110.

Fàbrega, C., Parcerisa, D., Thiry, M., Franke, C., Gurenko, A., Gómez-Gras, D., Solé, J., Travé, A., 2019. Permian-Triassic red-stained albitized profiles in the granitic basement of NE Spain: evidence for deep alteration related to the Triassic paleosurface. International Journal of Earth Sciences, 108, 2325-2347.

Foley, S.F., 1992. Vein-plus-wall-rock melting mechanisms in the lithosphere and the origin of potassic alkaline magmas. Lithos, 28, 435-453.

Fowler, M.B., Henney, P.J., 1996. Mixed Caledonian appinite magmas: implications for lamprophyre fractionation and high Ba-Sr granite genesis. Contributions to Mineralogy and Petrology, 126, 199-215.

Galán, G., Enrique, P., Butjosa, L., Fernández-Roig, M., 2017. Spinels of Variscan olivine hornblendites related to the Montnegre granitoids revisited (NE Spain): petrogenetic evidence of mafic magma mixing. Geologica Acta, 15(4), 323-336.

Innocent, C., Briqueu, L., Cabanis, B., 1994. Sr-Nd isotope and trace-element geochemistry of late Variscan volcanism in the Pyrenees: Magmatism in post-orogenic extension? Tectonophysics, 238, 161-181.

Jung, C., Jung, S., Hoffer, E., Berndt, J., 2006. Petrogenesis of Tertiary mafic alkaline magmas in the Hocheifel, Germany. Journal of Petrology, 47, 1637-1671.

Krmíček, L., Romer, R., Ulrych, J., Glodny, J., Prelević, D., 2015. Petrogenesis of orogenic lamproites of the Bohemian Massif: Sr-Nd-Pb-Li isotope constraints for Variscan enrichment of ultra-depleted mantle. Gondwana Research, 35, 198-216.

Lago, M., Arranz, E., Pocoví, A., Galé, C., Gil-Imaz, A., 2004. Permian magmatism and basin dynamics in the Southern Pyrenees: a record of transition from late Variscan transtension to early Alpine extension. In: Wilson, M., Neumann, E.-R., Davies, G.R., Timmerman, M.J., Heeremans, M., Larsen, B.T. (eds.). Permo- Carboniferous magmatism and rifting in Europe. London, Geological Society, 223 (Special Publications), 439-464.

Lago, M., de la Horra, R., Ubide., T., Galé., C., Galán-Abellán., B., Barrenechea., J.F., López-Gómez., J., Benito., M.I., Arche., A., Alonso-Azcárate, J., Luque., F.J., Timmerman., M.J., 2012. First report of a Middle-Upper Permian magmatism in the SE Iberian Ranges: characterisation and comparison with coeval magmatisms in the western Tethys. Journal of Iberian Geology, 38(2), 331-348.

Losantos, M., Montaner, J., Solà, J., Mató, E., Sampsó, J.M., Picart, J., Calvet, F., Enrique, P., Ferrés, M., Solé, J., 2000. Mapa Geològic de Catalunya 1:25.000. Palafrugell 335-1-1 (79-25). Barcelona, Servei Geològic de Catalunya (ICC).

le Maitre, R., Streckeisen, A., Zanettin, B., Le Bas, M., Bonin, B., Bateman, P. (eds.), 2002. Igneous Rocks: A Classification and Glossary of Terms: Recommendations of the International Union of Geological Sciences Subcommission on the Systematics of Igneous Rocks (2nd ed.). Cambridge, Cambridge University Press, 19. DOI: 10.1017/CBO9780511535581

Martínez, F.J., Reche, J., Iriondo, A., 2008. U-Pb SHRIMP-RG zircon ages of Variscan igneous rocks from the Guilleries massif (NE Iberia pre-Mesozoic basement): Geological implications. Comptes Rendus Geoscience, 340, 223-232.

Martínez, F.J., Iriondo, A., Dietsch, C., Aleinikoff, J.N., Peucat, J.J., Cirés, J., Reche, J., Capdevila, R., 2011. U-Pb SHRIMP-RG zircon ages and Nd signature of Lower Paleozoic rifting-related magmatism in the Variscan basement of the eastern Pyrenees. Lithos, 127, 10-23.

Martínez-Poza, A.I., Druguet, E., Castaño, L.M., Carreras, J., 2014. Dyke intrusion into a pre-existing joint network: The Aiguablava lamprophyre dyke swarm (Catalan Coastal Ranges). Tectonophysics, 630, 75-90.

McDonough, W.F., Sun, S.S., 1995. The composition of the Earth. Chemical Geology, 120, 223-253.

Murphy, J., 2013. Appinite suites: A record of the role of water in the genesis, transport, emplacement and crystallization of magma. Earth-Science Reviews, 119,35-59.

Orejana, D., Villaseca, C., Paterson, B.A., 2006. Geochemistry of pyroxenitic and hornblenditic xenoliths in alkaline lamprophyres from the Spanish Central System. Lithos, 86, 167-196.

Orejana, D., Villaseca, C., Billström, K., Paterson, B.A., 2008. Petrogenesis of Permian alkaline lamprophyres and diabases from the Spanish Central System and their geodynamic context within western Europe. Contributions to Mineralogy and Petrology, 156, 477-500.

Parcerisa, D., Thiry, M., Schmitt, J.M., 2010. Albitisation related to the Triassic unconformity in igneous rocks of the Morvan Massif (France). International Journal of Earth Sciences, 99, 527-544.

Pearce, J., 2008. Geochemical fingerprinting of oceanic basalts with applications to ophiolite classification and the search for Archean oceanic crust. Lithos, 100, 14-48.

Peccerillo, A., Taylor, S.R., 1976. Geochemistry of Eocene calc-alkaline volcanic rocks from the Kastamonu area, northern Turkey. Contributions to Mineralogy and Petrology, 58, 63-81.

Peng, P., Ernst, R., Hou, G., Söderlund, U., Zhang, S.H., Hamilton, M., Xu, Y.G., Denyszyn, S., Mège, D., Pisarevsky, S., Srivastava, R., Kusky, T., 2016. Dyke swarms: keys to paleogeographic reconstructions. Science Bulletin, 61(21), 1669-1671. DOI: 10.1007/s11434-016-1184-x

Pereira, M.F., Castro, A., Chichorro, M., Fernández, C., Díaz-Alvarado, J., Martí, J., Rodríguez, C., 2014. Chronological link between deep-seated processes in magma chambers and eruptions: Permo-Carboniferous magmatism in the core of Pangaea (Southern Pyrenees). Gondwana Research, 25, 290-308.

Perini, G., Cebria, J.M., López-Ruiz, J., Doblas, M., 2004. Carboniferous-Permian mafic magmatism in the Variscan belt of Spain and France: implications for mantle sources. London, Geological Society, 223 (Special Publications), 415-438.

Prelević, D., Foley, S.F., Cvetkovic, V., Romer, R.L., 2004. Origin of Minette by Mixing of Lamproite and Dacite Magmas in Veliki Majdan, Serbia. Journal of Petrology, 45(4), 759-792.

Reche, J., Martínez, F.J., 2002. Evolution of bulk composition, mineralogy, strain style and fluid flow during an HT-LP metamorphic event: sillimanite zone of the Catalan Coastal Ranges, Variscan basement, NE Iberia. Tectonophysics, 348, 111-134.

Riesco, M., Stüwe, K., Reche, J., Martínez, F.J., 2004. Silica depleted melting of pelites. Petrogenetic grid and application to the Susqueda Aureole, Spain. Journal of Metamorphic Geology, 22, 475-494.

Roberts, M., Pin, C., Clemens, J., Paquette, J.L., 2000. Petrogenesis of Mafic to Felsic Plutonic Rock Associations: the Calc-alkaline Querigut Complex, French Pyrenees. Journal of Petrology, 41(6), 809-844.

Rock, N.M.S., 1991. Lamprophyres. London, Blackie, 285pp.

Rollinson, H., 1993. Using geochemical data: Evaluation, presentation, interpretation. New York, Longman Scientific and Technical, Wiley, 352.

Ronca, S., Del Moro, A., Traversa, G., 1999. Geochronology, Sr-Nd isotope geochemistry and petrology of Late-Hercynian dyke magmatism from Sarrabus (SE Sardinia). Periodico di Mineralogia, 68, 231-260.

Rudnick, R.L., Gao, S., 2003. Composition of the continental crust. In: Rudnick, R.L. (ed.). The Crust. Treatise on Geochemistry, Oxford, Elsevier, 3, 1-64.

Scarrow, J.H., Molina, J.F., Bea, F. Montero, P., 2009. Within-plate calc-alkaline rocks: Insights from alkaline mafic magmas-peraluminous crustal melt hybrid appinites of the Central Iberian Variscan continental collision. Lithos, 110, 50-64.

Sebastian, A., Reche, J., Duran, H., 1990. Hercynian metamorphism in the Catalonian coastal ranges. Acta Geologica Hispanica, 255, 31-32.

Seifert, T., 2008. Metallogeny and Petrogenesis of Lamprophyres in the Mid-European Variscides. Amsterdam, IOS Press, 303.

Soder, C., 2017. Geochemistry and petrology of lamprophyres from the Hellenides and the European Variscides. PhD Thesis. Heidelberg (Germany), University of Heidelberg, 201pp. DOI: 10.11588/heidok.00023679

Solé, J., Cosca, M., Sharp, Z., Enrique, P., 2002. 40Ar/39Ar Geochronology and stable isotope geochemistry of Late-Hercynian intrusions from north-eastern Iberia with implications for argon loss in K-feldspar. International Journal of Earth Sciences, 91, 865-881.

Spišiak, J., Vetráková, L., Mikuš, T., Chew, D., Ferenc, S., Šimonová, V., Siman, P., 2019. Mineralogy and geochronology of calc-alkaline lamprophyres from the Nízke Tatry Mts. Crystalline complex (Western Carpathians). Mineralia Slovaca, 51, 61-78.

Srivastava, R., Ernst, R., Peng, P., 2019. Dyke Swarms of the World: A Modern Perspective. Singapore, Springer, 263-314. DOI: 10.1007/978-981-13-1666

Sun, S.S., McDonough, W.F., 1989. Chemical and isotopic systematics of oceanic basalts: implications for mantle composition and processes. London, Geological Society, 42 (Special Publications), 313-345.

Tanaka, T., Togashi, S., Kamioka, H., Amakawa, H., Kagami, H., Hamamoto, T., Yuhara, M., Orihashi, Y., Yoneda, S., Shimizu, H., Kunimaru, T., Takahashi, K., Yanagi, T., Nakano, T., Fujimaki, H., Shinjo, R., Asahara, Y., Tanimizu, M., Dragusanu, C., 2000. JNdi-1: a neodymium isotopic reference in consistency with La Jolla neodymium. Chemical Geology, 168, 279-281.

Ubide, T., Lago, M., Arranz, E., Galé, C., Larrea, P., 2010. The lamprophyric sub-vertical dyke swarm from Aiguablava (Catalonian Coastal Ranges): Petrology and composition. Geogaceta, 49, 83-86.

Ubide, T., 2013. The Cretaceous alkaline magmatism in northeast Iberia: igneous processes and geodynamic implications. Doctoral Thesis. Zaragoza (Spain), University of Zaragoza, 193pp.

Wilson, M., Neumann, E.R., Davies, G., Timmerman, M., Heeremans, M., Larsen, B., 2004. Permo-Carboniferous Magmatism and Rifting in Europe. London, Geological Society, 223 (Special Publications), 1-10. DOI: 10.1144/GSL.SP.2004.223.01.01

Winchester, J.A., Floyd, P.A., 1977. Geochemical discrimination of different magma series and their differentiation products using immobile elements. Chemical Geology, 20, 325-343.

CHAPTER 3

SECOND ARTICLE

Reference: **Mellado, E., Corbella, M A. Kylander-Clark, A, 2022. Allanite in Variscan Post-Collisional Lamprophyre Dykes from Les Guilleries (NE Iberia) as a Part of Rare Earth Elements Recycling in Collisional Orogens. Minerals, 12(8), 954.**

Allanite in Variscan Post-Collisional Lamprophyre Dykes from Les Guilleries (NE Iberia) as a Part of Rare Earth Elements Recycling in Collisional Orogens

Esteban Mellado [1,*], Mercè Corbella [1] and Andrew Kylander-Clark [2]

1   Department of Geology, Universitat Autònoma de Barcelona, Edifici Cs, 08193 Bellaterra, Spain; merce.corbella@uab.cat
2   Department of Earth Science, University of California, Santa Barbara, CA 93106, USA; kylander@geol.ucsb.edu
*   Correspondence: esteban.mellado@uab.cat

Abstract: Recent studies of Late Permian calc-alkaline lamprophyre dykes located in the Les Guilleries Paleozoic massif of the Catalan Coastal Range have revealed that allanite is present as the main REE-bearing accessory phase, which is the object of this study. The lamprophyre dykes are amphibole–plagioclase-dominated spessartites with a wide variety of accessory phases, including titanite, ilmenite, allanite, fluorapatite, spinel, zircon, and sulfides, and show complex alteration textures related to secondary albite, chlorite, epidote, titanite and calcite. The allanite crystal composition, analyzed by SEM-EPMA and LA-ICP-MS, evidences the solid solution between epidote and allanite with a ferriallanite component, similar to what is found in Variscan post-collisional granitoids from western Europe. However, heterogeneity in crystal shapes, sizes, type of zoning, dissolution embayment textures, growth of epidote coronas, mineral paragenesis, and the unique geochemical characteristics of allanite crystals suggest multiple crystallization events. At least two types of allanite–epidote composite grains have been identified: allanite Type I, with regular allanite–epidote core-to-rim zoning and a secondary allanite rim; and allanite Type II, with anhedral allanite cores surrounded by epidote coronas. Additionally, irregular zoning, complex dissolution textures and REE redistribution suggest the occurrence of deuteric and/or post-magmatic processes, which are also common in Variscan post-collisional plutons from the Catalan Coastal Range and nearby Paleozoic massifs. Multivariate statistical analyses of major elements in allanite–epidote composite grains show a relationship between major textural and geochemical variations for three out of ten principal components, mainly related to cationic substitutions between ferriallanite-(Ce) and epidote, but also involving Mn and Ti ($REE^{3+} + Fe^{2+} + Ti^{4+} + Mg^{2+} + Mn^{2+} = Al^{3+} + Ca^{2+} + Fe^{3+}$). The allanite U-Pb-Th-weighted mean age of 265 ± 15 Ma (MSWD = 0.57) is roughly similar to the age of emplacement of the lamprophyres in the upper crust in the mid–late Permian, and coincides with the period following the main tectonometamorphic and magmatic events of the post-collisional evolution in the Catalan Coastal Range. Th/U and La/Sm ratios suggest a metamorphic origin for most allanite grains, but a combination of metamorphic processes prior to partial melting, early–late magmatic crystallization, and/or post-magmatic hydrothermal processes is the most plausible explanation to account for the diversity of allanite grains in Les Guilleries lamprophyres.

Keywords: allanite; geochemistry; EPMA; calc-alkaline lamprophyre; geochemistry; Les Guilleries massif; Variscan orogeny; U-Pb ages

1. Introduction

Allanite-bearing calc-alkaline lamprophyres are widespread in the Variscan Belt of western Europe [1–4] and generally represent low-volume pulses of mantle-derived mafic magmas variably enriched in LILEs, HFSEs, and REEs, and emplaced in the brittle upper crust as dyke swarms during post-collisional periods of the Variscan orogeny, unlike

Permian and Cretaceous alkaline lamprophyre dykes that are post-Variscan. While the relative abundance of amphibole–phlogopite vs. plagioclase–K-feldspar is used to classify calc-alkaline lamprophyres and is thus the usual object of studies [5], the diversity of accessory phases present in these rocks is poorly constrained. Many studies of Variscan calc-alkaline lamprophyres have reported the presence of allanite as the main REE-bearing phase [2–4], but little information about their morphology, geochemistry and geochronology has been provided. Recent studies of post-collisional Variscan spessartite dykes in the Les Guilleries massif (Catalan Coastal Range, NE Iberia) have identified allanite as the main REE-carrier phase [6].

Allanite is a member of the epidote group, and its structure can accommodate large quantities of many chemical elements, mainly depending on the system composition rather than on the P-T conditions. This mineral testifies to the diversity of mineral formation environments, as well as to secondary processes such as metamictization and hydrothermal alteration [7,8]. Allanite's simplified crystal formula is $A_2M_3(SiO_4)(Si_2O_7)O(OH)$, where the A sites are mainly occupied by Ca^{2+} and REE^{3+}, and M sites are mainly occupied by Al^{3+}, Fe^{3+}, Fe^{2+}, Mg^{2+}, $Mn^{2+,3+}$, Ti^{4+}, and Th^{4+} [8,9]. Solid ferriallanite–allanite–epidote–clinozoisite solid solutions are well known within many igneous, metamorphic and sedimentary rocks, and, as they can also be an important repository of Th and U, which makes them a promising object for U-Pb-Th dating [10]. Allanite composition varies in terms of the ratio $Fe^{3+}/(Fe^{3+} + Al)$ but is limited by whole-rock composition, so that epidote group minerals in metabasite lithologies are more Fe-rich than those in metasedimentary lithologies, which tend to be more Al-rich and typically include zoisite [11]. Slow rates of intra-crystalline Fe^{3+}-Al exchange, especially at low temperatures, preserve complex zonation patterns in individual grains that can serve as a recorders of continuous or discontinuous prograde and retrograde reactions and the P-T-fluid-redox conditions of metamorphism [11]. Allanite can exhibit a large variety of textures depending on the reaction history during metamorphism [12–14]. The transformation of allanite to monazite during low-to-medium-grade metamorphism is relatively well known [15]. Allanite commonly forms at the expense of detrital, magmatic, or metamorphic monazite close to the biotite-in reaction, at the transition between the chlorite and biotite zones [13,14,16]; allanite is consumed to form monazite during the staurolite-in reaction, at the transition between the garnet and the staurolite–kyanite zones [14,16]. Thermodynamic modelling in schists shows that the first metamorphic allanite appears at ~425 °C and 4.5 kbar, and transforms to monazite at ~600 °C and 7.5 kbar [16]. The paragenesis allanite+apatite forms during retrograde metamorphism at the expense of monazite via fluid-assisted dissolution-precipitation processes at greenschist facies [17], commonly related to shear zones [13,18].

REE-zoning in igneous allanite has long been recognized as reflecting fractional crystallization [19], most commonly from melts of high water content [20]. Experimental data on igneous allanite solubility [21,22] cover a range of melt compositions and pressures. Where allanite forms in magma, it largely controls the LREE content of the melt because it can incorporate them at weight-% level. For Th, U, and Y, as noted above, competition from coexisting phases (zircon, monazite, xenotime, titanite or rutile) may intervene. As summarized by Smye et al. [23], REE fractionation in allanite depends on magma composition. Typically, chondrite-normalized REE patterns are steeply negative for early-formed allanite, but depletion of LREEs then leads to nearly flat patterns, and the overall core-to-rim zoning in allanite may end with REE-enriched (or even REE-poor) peripheral epidote [24]. La/Sm vs. Th/U and La/Sm vs. Eu/Eu* (europium anomaly) have been used to discriminate between metamorphic and magmatic allanite, considering that fluid has lower differentiation ability for La (LREE) and Sm (MREE) than magmatic melt, whereas the mobility of U in the fluid is higher than that in the melt [25,26].

This study characterizes allanite crystals from Les Guilleries spessartite dykes (amphibole–plagioclase-dominated lamprophyres) to gain insights about their occurrence, chemical composition, age and petrogenetic implications. The presented data will be useful

for further comparison and correlation between post-collisional lamprophyre dykes of the European Variscan Belt.

2. Geological Setting

The Variscan Belt in NE Iberia is found in the Catalan Coastal Range, the Pyrenees and the Iberian Ranges. Their geology records the syn- to post-collisional magmatic evolution from peak metamorphic conditions in the Late Carboniferous [27] until the end of the orogenic cycle in the Late Permian–Triassic, which is marked by the shift from post-collisional calc-alkaline magmatism to post-orogenic alkaline magmatism [28,29]. Felsic and mafic igneous rocks of Late Carboniferous–Early Permian age and syn- to post-collisional of calc-alkaline affinity outcrop in the area. They appear to have formed from variable degrees of lower crustal assimilation and differentiation and were emplaced in the mid–upper Variscan crust in a local predominantly extensional context. They are linked to a regional dextral strike-slip regime related to late-Variscan shear zones that must have displaced Gondwana to the west with respect to Laurasia during orogenic collapse [30]. The mafic complexes are suggested to have derived from a mantle source enriched in LILEs and LREEs, attributed to metasomatic processes of the lithospheric mantle during previous subduction events [30].

In Les Guilleries Massif, located 80 km NNE of Barcelona, outcrop the oldest Variscan igneous rocks which form the Susqueda complex, the largest basic massif of the Catalan Coastal Range that intruded the Paleozoic basement. The mafic complex is composed of quartz diorites and diorites with calc-alkaline geochemical affinity, together with hornblende gabbros and hornblendites [31,32]. A syn-collisional diorite sheet has provided a U-Pb age of 323.6 $\pm$ 2.8 Ma [33] but most mafic intrusives are younger and post-tectonic [34]. Felsic rocks are younger too; leucogranites have been dated to 305–299 Ma old [33], and porphyritic granites have yielded unpublished U-Pb SHRIMP ages of 284 $\pm$ 3 Ma [35], which agrees with the age of similar mafic and felsic plutonic bodies in the nearby Montnegre Massif ($^{40}Ar/^{39}Ar$ ages between ca. 291 and 285 Ma [36]). This massif also contains ultrabasic/basic-to-intermediate rocks associated with late-Variscan calc-alkaline granites, showing mineralogical and geochemical characteristics typical of appinite suites, with cumulate hornblendites and gabbros crystalized from K-rich and fluid-rich magmas, and a complex mingled zone between diorites and biotite granodiorites [37,38].

Les Guilleries lamprophyres appear as a subvertical dyke swarm emplaced in the intersection between two perpendicular regional fault systems oriented NE–SW and NW–SE (Figure 1a,b). These dykes crosscut all previous sequences including schist and marbles from the basement and Variscan leucogranites, granodiorites, quartz-monzonites and pegmatites. The lamprophyres are porphyric to panidiomorphic spessartites, with chloritized mafic phenocrysts of different shapes and sizes between 0.5 and 1.5 mm, where amphibole is the only recognizable primary phenocrystal phase [6]. The groundmass contains mainly of chloritized and feldspathic domains (anorthite > k-feldspar), both enclosing variable proportions of amphibole (actinolite to hornblende), titanite, epidote, calcite, ilmenite, allanite, fluoroapatite, spinel, zircon, pyrite, and spinel; and variably replaced by secondary calcite, epidote, chlorite, albite, titanite and quartz. These lamprophyres present a calc-alkaline geochemical signature similar to the other igneous rocks of the area, with hybrid mantle–crust composition typical of these rocks; that is, with enrichments in MgO, Cr and Ni together with LILEs, HFSEs and REEs, and initial Sm-Nd isotopic compositions consistent with an enriched subcontinental lithospheric mantle (SCLM) source [6]. Titanite U-Pb dating yields a MSWD age of 262 $\pm$ 7 Ma, which place these dykes as the youngest calc-alkaline mafic intrusion found in the area related to the fragmentation of the Variscan Belt [6].
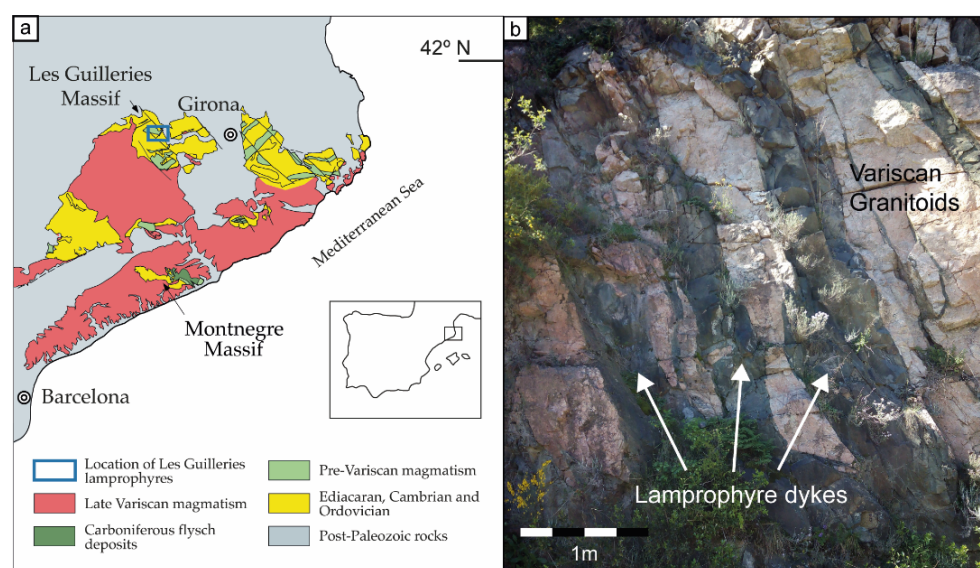
Figure 1. (**a**) Simplified geological map of the northernmost Catalan Coastal Range and geographic location of Les Guilleries massif; (**b**) Photograph of Les Guilleries spessartites dykes.

3. Materials and Methods

Petrographic analyses and SEM characterization of lamprophyre allanite crystals of 10 thin sections were performed at the Geology Department and Serveis de Microscòpia of the Universitat Autònoma de Barcelona.

The chemical composition of allanite was determined using a JEOL JXA-8230 electron microprobe at an accelerating voltage of 20 kV and a beam size of 3–5 μm at the Centres Científics i Tecnològics of the Universitat de Barcelona. Eighteen allanite crystals from two variably altered calc-alkaline lamprophyre dykes were analyzed for three different sets of elements to include Si, Ti, Al, Ca, Fe, Mg, Mn, La, Ce, Pr, Nd, Pr, Sm, Eu, Dy, Yb, Lu, Ba, Zn, Cr, V, K, Na, Th, U and F. Several elements were below detection limits: Eu to Lu (<1300 ppm), Cr < 600 ppm, V < 1000 ppm, Th and U < 2500 ppm, K < 500 ppm, Zn < 600 ppm, Na < 800 ppm, Sc < 600 ppm. SiO_2, TiO_2, Al_2O_3, CaO, FeO_{tot}, MgO, MnO, La_2O_3, Ce_2O_3, and Nd_2O_3 were analyzed in the three sets of elements.

Principal component analysis (PCA) has been used before to evaluate geochemical data [39,40]; PCA allows analysts to statistically group chemical compositions and identify possible variation trends. It is important to mention that PCA does not always represent geochemical processes, because natural geochemical processes do not always follow a multivariate Gaussian distribution or orthogonal coordinates, a prerequisite for PCA [41]. It is a useful tool to reduce bias when analyzing highly heterogeneous chemical systems and enables geological interpretations to be supported with statistics rather than stated merely as a subjective point of view. The analyses were made using scikit-learn package of Python 3.6.

In situ U-Th-Pb dating of allanite grains from two lamprophyre dykes was performed by laser-ablation split-stream ICP-MS (LASS) on the same polished thin sections used for the petrological and chemical studies. The analyses were conducted at the UC Santa Barbara (United States), following the procedures outlined in Spencer et al. [42], Kylander-Clark et al. [43], and Kylander-Clark [44]. Samples were ablated with a Photon Machines Excite 193 nm laser ablation system (San Diego, CA, USA) equipped with a HelEx cell, using a spot size of 15 μm and a repetition rate of 5 Hz. Aerosol from the laser was carried in He, mixed with Ar and analyzed by a Nu Instruments Plasma HR MC-ICPMS (Wrexham, UK) for U-Pb analysis and by an Agilent 7700X for trace element analysis. Allanite analysis and data reduction required a two-step approach, first using NIST612 glass to correct for instrument drift and bias in $^{207}Pb/^{206}Pb$ and $^{206}Pb/^{238}U$ ratios, followed by a correction of the $^{206}Pb/^{238}U$ ratio so that reference materials (RMs) SISS, BONA, and TARA yielded

ages within 2% of accepted values [23,45]. Trace elements were determined using NIST612 as the primary RM and 28Si as the internal standard, using a Si wt.% estimated by the stoichiometry of the major constituents (range of 14.9–17.3 wt.% Si).

4. Results

4.1. Petrography

Allanite is unevenly distributed within the lamprophyre matrix and is commonly found as large (10–100 micrometer) and isolated subhedral/anhedral crystals with compositions grading towards epidote, forming allanite–epidote composite grains (Figure 2). All studied grains exhibit complex growth and alteration textures, resulting in a wide variety of morphological differences. In spite of this diversity and the uniqueness of most individual composite grains, two types of morphologies are the most common. Allanite Type I corresponds to subhedral allanite cores with regular parallel zoning transitioning towards epidote rims. The zonation is perpendicular to the main crystal axis and is followed by a micrometer-size allanite outer rim (Figure 2a–c). This secondary allanite rims are not always parallel with the previous zonation (Figure 2a). Type I grains are encountered inside the feldspathic part of the lamprophyre matrix, commonly next to albitized anorthite microphenocrysts, titanite and apatite. Allanite Type II corresponds to anhedral allanite cores with irregular zoning, surrounded by epidote coronas of tens-of-micrometers thickness in sharp contact, and dissolution embayments within the allanite cores. These rounded grains are enclosed by chlorites crystals or within the chloritized part of the lamprophyre matrix, commonly next to tiny apatite crystals, euhedral amphibole, and ilmenite with titanite coronas. Type II grains are also variably replaced by secondary chlorite, albite and quartz (Figure 2d–f). Other composite grains present multiple allanite cores with apparently sigmoidal shapes (Figure 2g), while others are almost completely replaced by secondary minerals, obscuring their original morphology (Figure 2h). Additionally, some epidote coronas also show wave-like bright lines of allanite composition (Figure 2i).
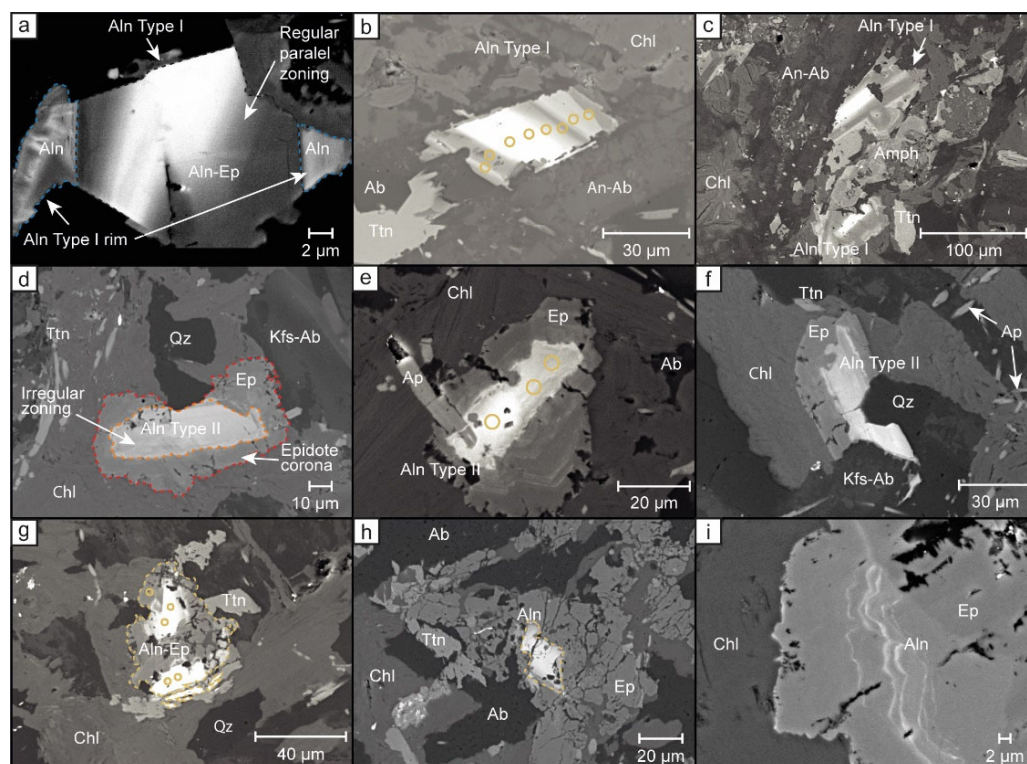

Figure 2. Back-scattered electron images representative of the morphological diversity found in allanite–epidote composite grains from Les Guilleries spessartite dykes. (**a**–**c**) Allanite Type I presenting

allanite cores grading towards epidote with parallel zoning and a secondary allanite rim (allanite Type I (rim)), variably affected by secondary replacement; (**d–f**) Allanite Type II presenting allanite cores with irregular zoning surrounded by epidote coronas, variably replaced by secondary chlorite, albite and quartz; (**g**) Unique allanite–epidote composite grain with two allanite cores and apparently sigmoidal shape in contact with titanite, surrounded by chlorite and affected by secondary albite; (**h**) Allanite fragment almost completely replaced by secondary epidote, chlorite and albite; (**i**) Wave-like allanite domain inside epidote corona. Blue, orange and red lines correspond to allanite Type I rim, allanite Type II, and epidote coronas, respectively. Yellow circles represent EPMA-analyzed spots.

4.2. Microprobe Chemistry

Electron microprobe data of 78-point analyses of 18 different allanite-epidote grains (capturing cores, zoned domains and rims) are presented in Supplementary Materials Table S1. From these analyses it is deduced that all allanite types are mainly composed of SiO_2 (30.2–38.2 wt.%), Al_2O_3 (12.8–24.3 wt.%), CaO (11.1–23.9 wt.%), FeO_{tot} (9.3–16.6 wt.%), Ce_2O_3 (0.1–11.4 wt.%), La_2O_3 (2.4–7.6 wt.%), and Nd_2O_3 (2.0–3.4 wt.%), with minimal TiO_2 (0.5–2.8 wt.%), MgO (0.2–0.7 wt.%), and MnO (0.1–0.7 wt.%). Table 1 shows a a summary of the compositional range of defined allanite types. Elemental mapping shows that the brightness in BSE images is proportional to rare earth element (Ce > La > Nd) and Fe concentration, and inversely proportional to Al, Si and Ca concentration (Figure 3).

Table 1. Range of chemical compositions obtained by EPMA of defined allanite types.

Allanite Type	Type I	Type I (rim)	Type II	Type II (EpC)	Other
N° of Analyses	24	7	21	6	20
SiO_2	30.2–38.1	33.3–36.4	30.8–35.2	37.0–38.4	30.9–37.5
Al_2O_3	13.3–24.2	20.7–24.3	12.8–22.0	23.2–24.4	13.4–22.8
CaO	11.1–23.2	15.6–21.1	11.8–19.3	22.2–23.5	11.2–21.3
FeO	10.0–15.1	9.7–10.7	10.3–15.4	11.5–12.8	10.7–16.2
Ce_2O_3	0.2–11.4	1.6–6.4	3.8–10.8	0.0–0.6	1.5–11.3
La_2O_3	0.1–7.6	0.8–4.2	2.1–5.9	0.0–0.2	0.7–7.3
Nd_2O_3	0.0–3.0	0.6–2.0	0.9–3.1	0.0–0.4	0.5–3.4
MgO	0.0–0.6	0.1–0.4	0.2–0.4	0.0–0.2	0.2–0.7
MnO	0.1–0.6	0.5–1.0	0.0–0.4	0.1–0.3	0.1–0.4
TiO_2	0.4–2.2	0.2–0.7	0.2–2.8	0.0–0.4	0.1–2.0
UO_2	<DL	<DL	<DL	<DL	<DL
ThO_2	<DL	<DL	<DL	<DL	<DL
Total	92.7–97.5	94.4–97.2	93.8–97.5	97.0–98.0	94.7–97.6
Si [apfu]	2.95–3.07	2.95–3.0	2.95–3.08	2.95–3.01	2.93–3.08
Al [apfu]	1.52–2.26	2.18–2.33	1.47–2.25	2.17–2.26	1.53–2.19
Ca [apfu]	1.15–1.97	1.48–1.84	1.23–1.75	1.89–2.0	1.15–1.86
Fe [apfu]	0.68–1.22	0.68–0.8	0.75–1.25	0.75–0.85	0.74–1.31
Ce [apfu]	0.01–0.4	0.05–0.21	0.12–0.39	0.0–0.02	0.05–0.39
La [apfu]	0.0–0.27	0.02–0.14	0.07–0.2	0.0–0.01	0.02–0.25
Nd [apfu]	0.0–0.1	0.02–0.06	0.03–0.11	0.0–0.01	0.01–0.11
Mg [apfu]	0.0–0.09	0.01–0.06	0.02–0.06	0.0–0.02	0.03–0.09
Mn [apfu]	0.0–0.04	0.04–0.07	0.0–0.03	0.01–0.02	0.01–0.03
Ti [apfu]	0.02–0.16	0.01–0.04	0.01–0.2	0.0–0.02	0.0–0.14
A	1.88–2.03	1.87–1.95	1.9–2.0	1.93–2.01	1.88–2.09
M	2.95–3.11	3.07–3.14	2.95–3.11	3.03–3.08	2.75–3.11
%Fe^{+3}	0.43–0.99	0.48–0.87	0.41–0.72	0.96–1.0	0.41–0.9
REE_2O_3 [wt.%]	0.4–22.61	2.91–13.6	7.29–20.95	0.13–1.14	2.76–21.68

Oxides in weight percent. [apfu] = atoms per formula unit. A and M correspond to crystallographic sites. REE_2O_3 = sum of rare earth element oxides. DL= detection limit.
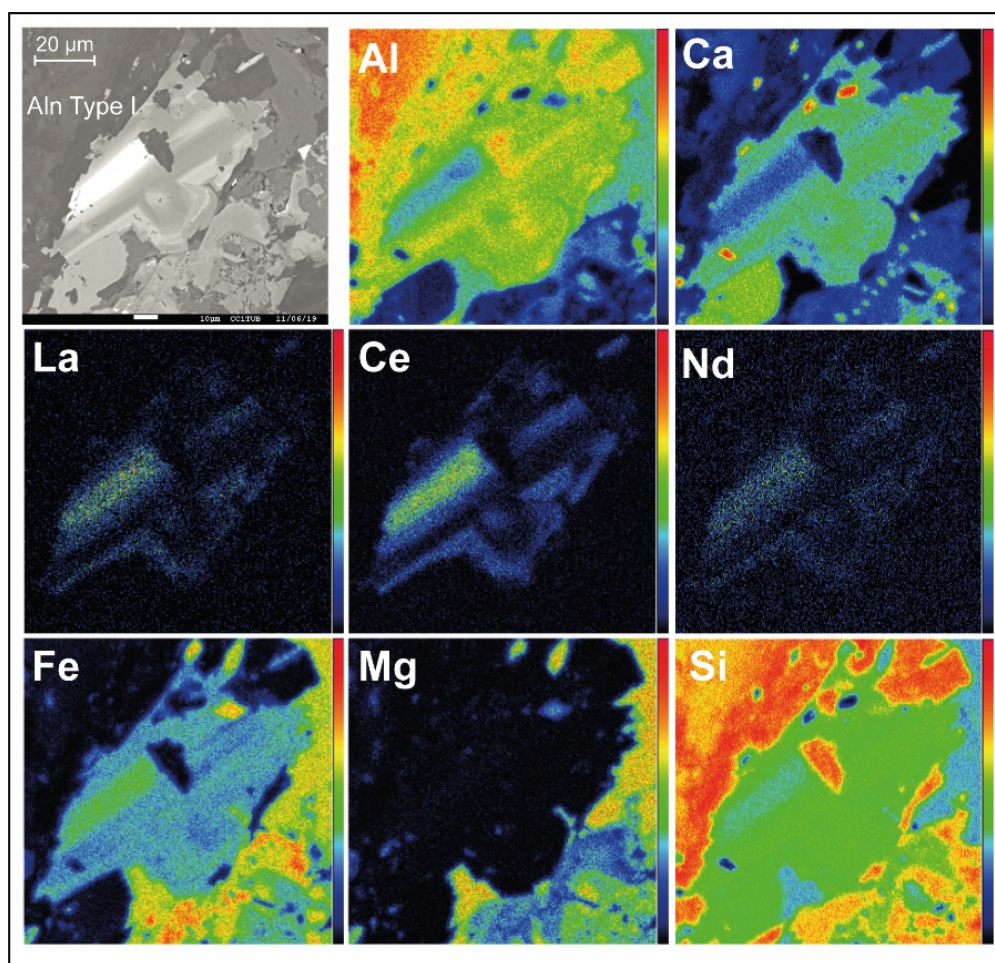
Figure 3. BSE image and concentration maps of a representative allanite Type I composite grain, including Al, Ca, La, Ce, Nd, Fe, Mg and Si. The scales for the color codes on the right-hand side of each image indicate counts of specific X-ray radiation per time unit; that is, red and yellow color indicate higher concentration, and blue-to-black the lower concentration. It is shown that the brightness of the BSE image is proportional to the REE content in allanite, which in this crystal is Ce > La > Nd.

Allanites of Type I show ferriallanite-(Ce) cores transitioning towards epidote, followed by a rim with a higher clinozoisite component and less REE enrichment (Figure 4a). Allanite Type I cores present the highest levels of REEs with a total of REE oxides up to 22.9 wt.% (Figure 4b). Type I rims have less FeO_{tot} at the same level of Ce_2O_3 and more Al_2O_3 at the same level of CaO than Type I cores (Figure 4c,d). Additionally, some cores of allanite Type I present the highest MgO and lowest SiO_2 content compared to the rims and to allanite Type II (Figure 4e).

Allanite Type II cores show similar ferriallanite–epidote solid solution to Type I cores but with REEs never below 0.2 apfu and less REE enrichment in general when compared with Type I cores. Irregularly zoned domains in Type II present similar geochemical characteristics to parallel-zoned domains of Type I. All allanite types also show an inverse correlation between REE and SiO_2 content (Figure 4b).
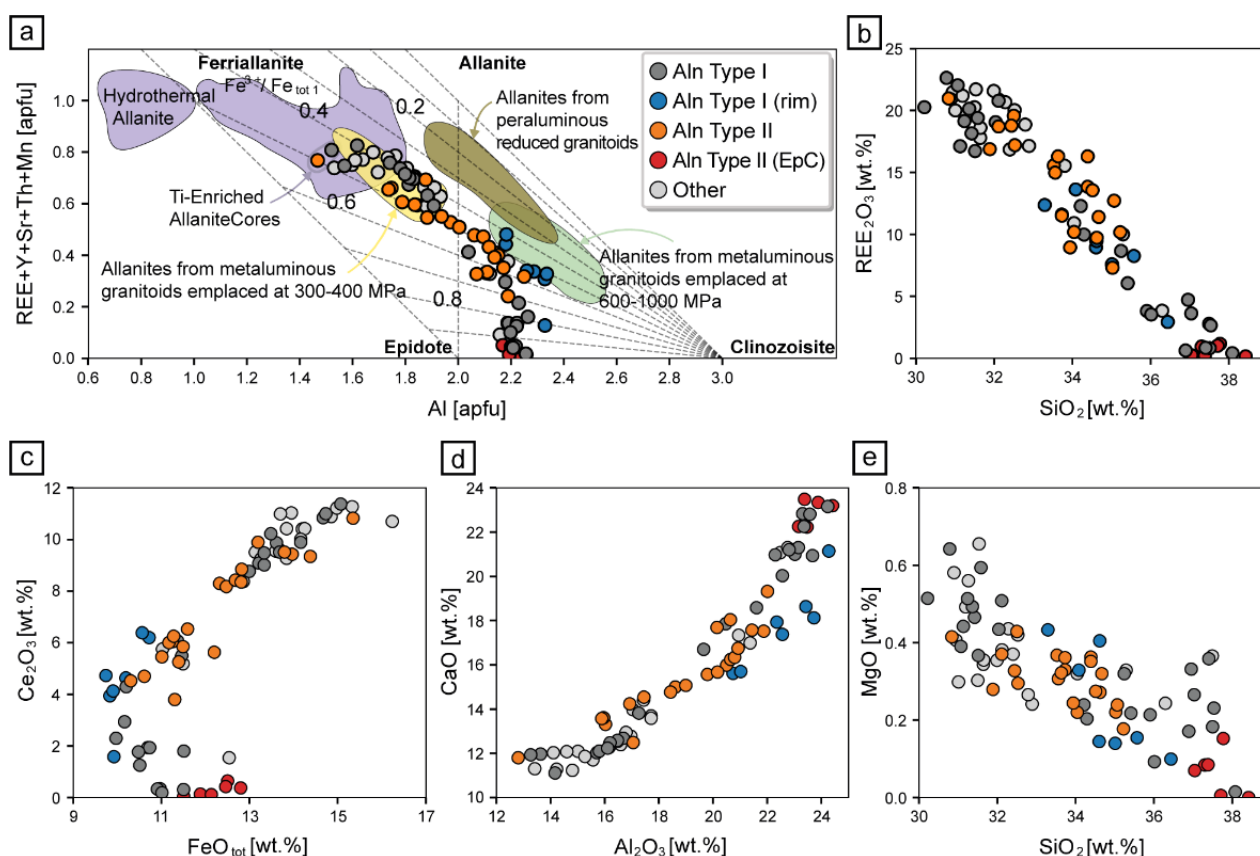
Figure 4. (**a**) Cationic Al vs. REE plot after Petrík et al. [46], showing the position of the studied allanites in the ferriallanite-allanite-epidote-clinozoisite system. (**b**) SiO_2 vs. REE_2O_3 (sum of rare earth element oxides. (**c**) FeO_{tot} (total Fe oxides) vs. Ce_2O_3. (**d**) Al_2O_3 vs. CaO. (**e**) SiO_2 vs. MgO. Aln Type I: Allanite Type I. Aln Type II: Allanite Type II. EpC: Epidote corona. Yellow, green and brown areas: allanite from peraluminous and metaluminous Variscan granitoids [47]. Purple area: hydrothermal allanite [48,49].

4.3. Principal Component Analyses

The 10 major oxides (SiO_2, Al_2O_3, CaO, FeO, Ce_2O_3, La_2O_3, Nd_2O_3, MgO, TiO_2, and MnO) of the 78 microprobe point analyses were used for PCA. The first principal component (PC1) accounts for 75.2% of the sample variance, the second principal component (PC2) accounts for 11.9%, and the third principal component (PC3) accounts for 4.8%. Accordingly, 91.9% of the variance was accounted for by the first three out of ten components (Figure 5a). This means that just three principal components describe most of the observed variation which can be visualized in binary plots. As observed in Figure 5, PC1 is dominated by the anti-correlation between Si-Al-Ca and Fe-LREE-Ti in the allanite–epidote zonation of both allanite Type I and II, while PC2 shows a relation with higher MnO values in the rims of allanite Type I. PC3 on the other hand is associated with high TiO_2 values in Type I, Type II and other allanite grains. These reveal the connection between textural and chemical variations, confirming that most of the variance of Les Guilleries lamprophyre allanites is related to the known ferriallanite–epidote solid solution (PC1), while other subtle compositional differences between cores and rims are revealed by PC2 and PC3.
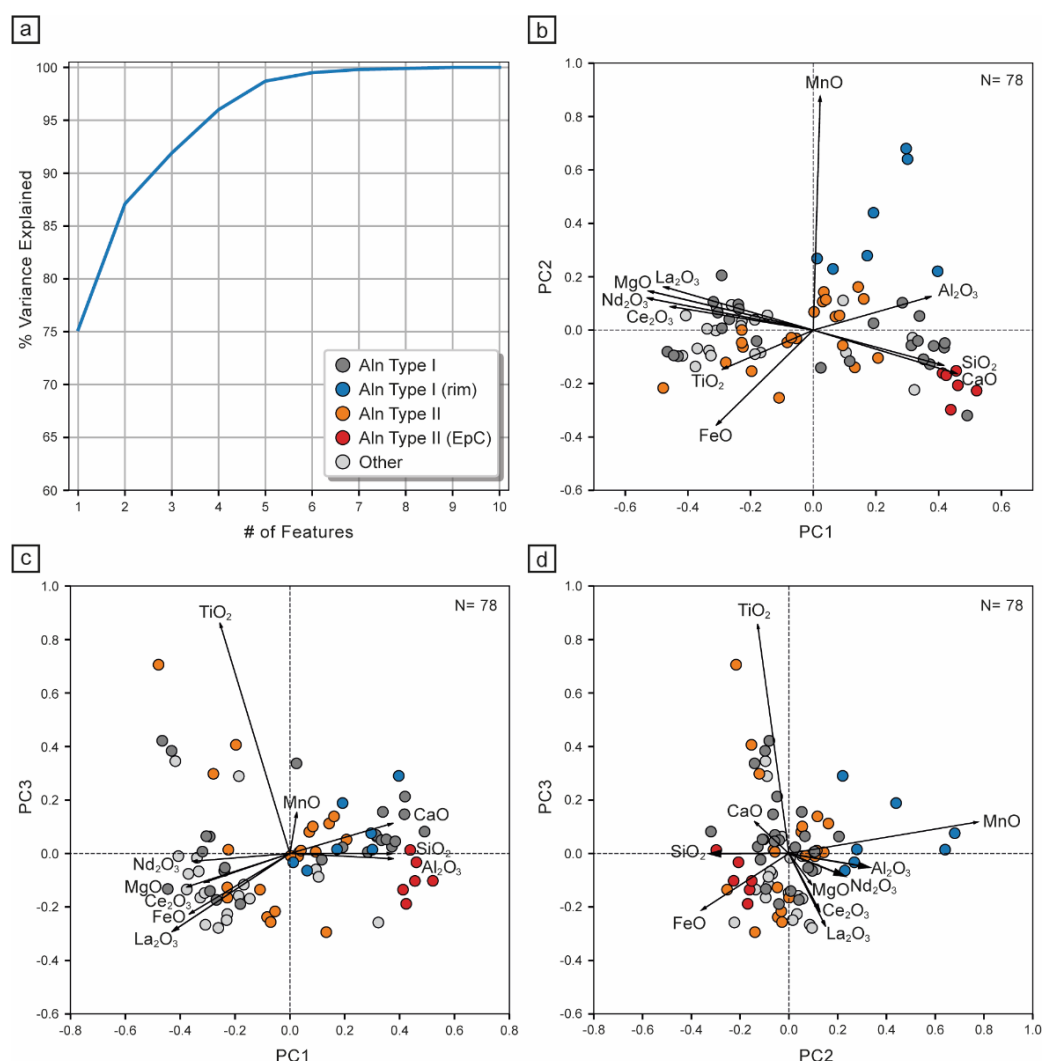
Figure 5. Principal component analysis of 10 major oxides using microprobe geochemical data. (**a**) Cumulative explained variance of the 10 principal components. A total of 91.9% of the variance is explained by the first three out of the 10 components. (**b**–**d**) correspond to binary plots of the three main principal components. (**b**) PC1 vs. PC2; (**c**) PC1 vs. PC3; (**d**) PC2 vs. PC3. The compositional vector of each major oxide is projected into principal components coordinates for easy visualization of the main patterns. N = number of point analyses considered.

4.4. LA-ICP-MS In Situ U-Th-Pb Ages

Radiometric dates obtained from 29-point analyses (Supplementary Materials Table S2) in different growth domains of five allanite crystals range between ~234–362 Ma (^{207}Pb-corrected ^{206}Pb/^{238}U date), and form a single isochron with an age of 265 $\pm$ 15 Ma (MSWD = 0.57, Figure 6); this age is equivalent to the 262 $\pm$ 7 Ma U-Pb age obtained from titanites of the same lamprophyres, interpreted as the age of lamprophyre emplacement [6]. It is important to note that the compositional changes in Type I, Type II and other allanite grains occur in a range of a few micrometers, smaller than the LA-ICP spot size of 15 micrometers, and therefore the ages obtained could represent averages of different growth domains, and not necessarily an exact period of crystal growth. Additionally, given the high uncertainty of individual allanite dates, the scatter of dates is probably the result of analytical scatter rather than geologic scatter. Nevertheless, younger dates in allanite Type I and older dates in allanite Type II are consistent with textural relationships. The rims of allanite Type I also show the youngest ages, but as they are always thinner than 5 micrometers, the dates are averaged with the internal part of the grain. On the other

hand, the timespan covered by the isochron age between ~280–250 Ma is roughly the same as the timespan covered by the late evolution of southern branch of the Variscan Belt; that is, a late Carboniferous–Permian collisional event, with localized magmatic recycling, extensional and transcurrent tectonic settings, exhumation of metamorphic terranes, and development of localized volcano-sedimentary basins [50]. The time span also corresponds to the period following the main syn- to post-collisional tectonometamorphic and magmatic evolution of the Catalan Coastal Range under the peak metamorphic conditions in Late Carboniferous described above in the Geological Setting Section, with specific periods of 305–299 Ma for leucogranites, 288 Ma for the Aiguablava pluton, and 285 Ma for porphyritic granites [33,36].
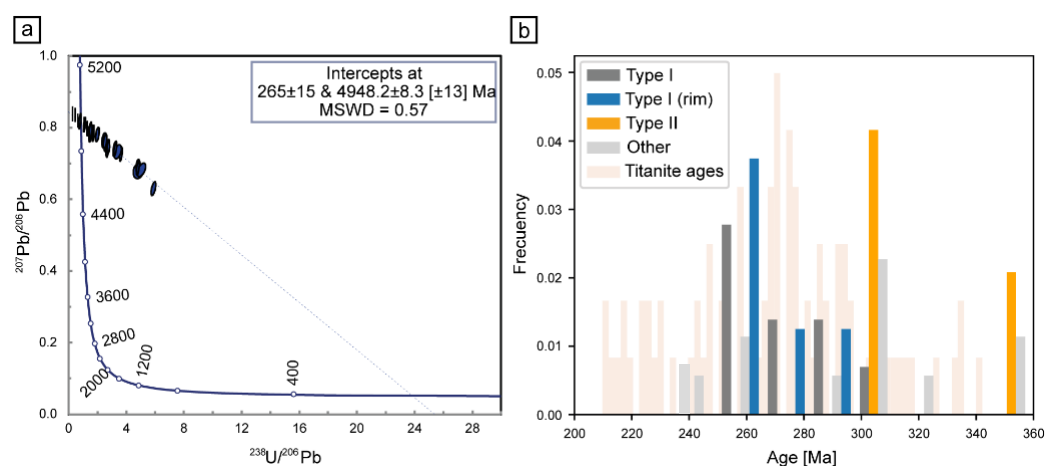
Figure 6. (**a**) Allanite Tera–Wasserburg concordia diagram using measured $^{207}Pb/^{206}Pb$ and $^{238}U/^{206}Pb$ ratios corrected for common Pb and Th content, with the data conversion performed by Isoplot 3.7. Allanite data from the two samples are plotted at 2σ and uncertainties on lower intercept ages are 95% confidence, with overall weighted average of 262 ± 7 Ma. (**b**) Histogram showing the frequency distribution of defined allanite types ranging from 234 and 362 Ma. Dated allanite crystals include the ones in Figure 2a,b,e,g. Titanite U-Pb dates from [6] are shown for comparison.

Complementary geochemical data reveal that U and Th concentrations are in the range of 4–45 ppm and 4–368 ppm, respectively (Supplementary Materials Table S2). Allanite Type I presents variable REE patterns with a tendency towards slightly-negative-to-positive Eu anomalies, decreasing Ce content, and variable trace element ratios (Figure 7). The most REE-rich cores of allanite Type I present flat HREE patterns and the highest HREE content. Allanite Type II, on the other hand, presents exclusively negative Eu anomalies, with similar HREE content in irregularly zoned cores but slightly variable LREE content, and epidote coronas with similar patterns but with total REE content lower by one order of magnitude. Th/U ratios are relatively low for all allanite types, and allanites of Type I present higher La/Sm ratios. Other allanite grains are roughly similar to allanite Type I, although unique features of some grains could also be present. Trace element ratios of all allanite–epidote grains (low Th/U and La/Sm, variable Eu/Eu*) plot in the field of metamorphic origin or closer to it in the diagram plots of La/Sm vs. Th/U and La/Sm vs. Eu/Eu* [25,26].
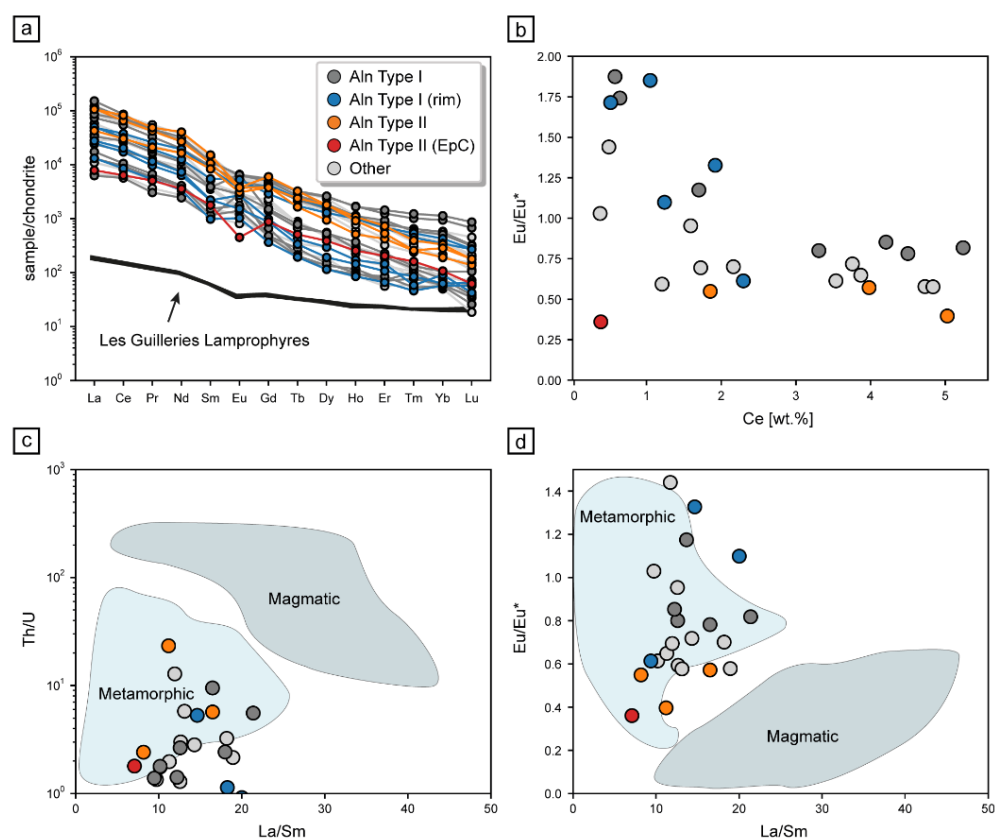
Figure 7. Trace elements of allanite from Les Guilleries lamprophyre dykes obtained by LA-ICP-MS. (**a**) Chondrite-normalized REE patterns of defined allanite types. Normalizing values are from Sun and McDonough [51]. (**b**) Ce vs. Eu/Eu* [Eu/Eu* = (Eu)cn/[(Sm)cn × (Gd)cn]0.5]. (**c**) Th/U vs. La/Sm. (**d**) Eu/Eu* vs. La/Sm. Magmatic and metamorphic allanite fields from [25,26].

5. Discussion

The textural and chemical heterogeneities of allanite–epidote composite grains found in Les Guilleries spessartite dykes suggest a complex geological story with multiple crystallization periods that could be related to metamorphic, magmatic, and/or hydrothermal processes. However, most grains are within the ferriallanite–allanite–epidote solid solution and generally present the same cationic substitutions, as indicated by PC1 of the principal component analysis, which accounts for 75% of the compositional variability (Figures 5b,c and 8a). Allanite crystals are also affected by secondary replacement, and therefore some primary features may have been modified by later processes. Nevertheless, petrographic, geochemical and statistical results show at least two distinct types of allanite–epidote composite grains. Allanite Type I, encountered in the feldspathic part of the matrix, corresponds to subhedral parallel-zoned crystals, from REE-enriched allanite cores grading towards epidote with a secondary rim of less REE-enriched allanite, the latter with a higher clinozoisite component and characteristic slight Mn enrichment, as revealed by PC2 of the principal component analysis (Figures 5b,d and 8b). Allanite Type I is apparently younger than allanite Type II and shows a variable Eu anomaly, being negative in the most REE-enriched cores, and positive towards the less REE-enriched rim (Figure 7). Allanite Type II, encountered in the chloritized part of the matrix, corresponds to REE-rich cores surrounded by epidote coronas, presents a negative Eu anomaly, and is, apparently, the oldest (Figures 6 and 7).

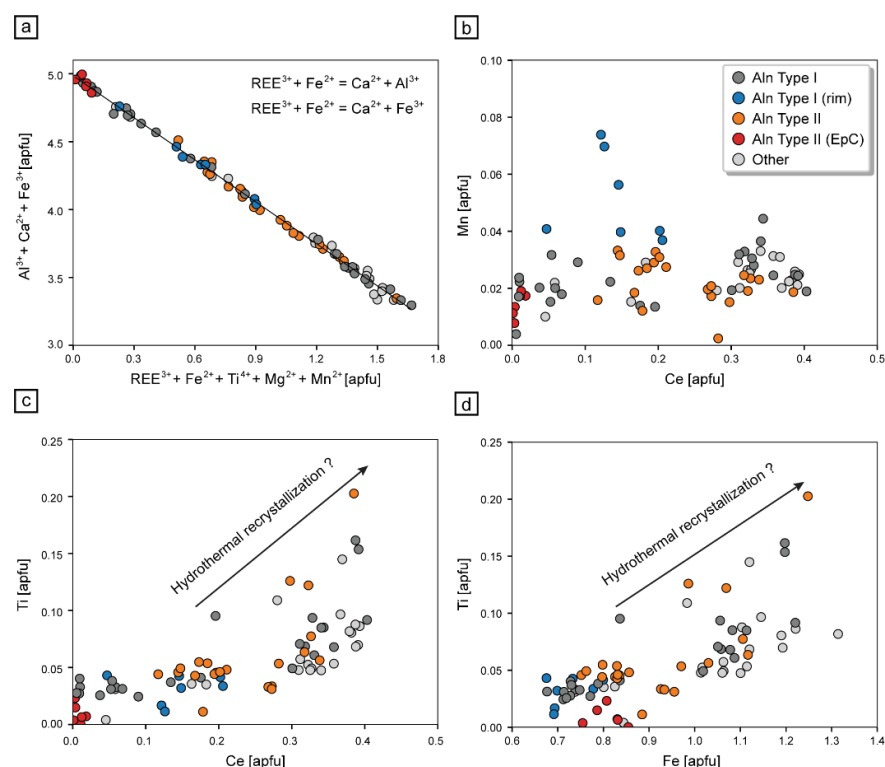**Figure 8.** Cationic plots of defined allanite types relating the groups of elements resulting from the principal component analyses. (**a**) $REE^{3+} + Fe^{2+} + Ti^{4+} + Mg^{2+} + Mn^{2+}$ vs. $Al^{3+} + Ca^{2+} + Fe^{3+}$ showing the cationic substitutions in allanite structure. (**b**) Ce vs. Mn. (**c**) Ce vs. Ti. (**d**) Fe vs. Ti. [apfu] = atoms per formula unit. See explanation in the text.

Les Guilleries lamprophyres represent, to date, the last magmatic pulse with a calc-alkaline geochemical signature of the Catalan Coastal Range and Eastern Pyrenees. It occurred in a post-collisional tectonic setting related to lithospheric-scale dextral mega shear zones which developed during orogenic collapse before the onset of generalized Triassic extension [30]. These mafic dykes were emplaced in the upper Variscan crust after the main syn- to post-collisional magmatism which evolved batholitic-sized calc-alkaline granitoids, minor mafic intrusions with local ultramafic cumulates, and peraluminous leucogranite bodies. An enriched SCLM origin has been inferred indirectly for the most mafic components of the post-collisional magmatic system, and Les Guilleries lamprophyres must represent the least differentiated sample from this subduction-related enriched SCLM source [6]. According to the obtained ages, the emplacement of the lamprophyres was also cogenetic with volcanism in pull-apart basins evolving from calc-alkaline-to-alkaline geochemistry during Permian times [28] and later was affected by regional scale syn- to post-magmatic hydrothermal alteration.

Considering this interpretation, and the coincidence of allanite U-Th-Pb dates with the late Variscan evolution of the area, it is suggested that allanite crystallization was a multi-stage process related to (i) the metamorphic evolution of the SCLM source, (ii) magmatic evolution after partial melting until emplacement, (iii) deuteric/autometasomatic processes common in lamprophyres due to their high volatile content, and/or (iv) post-magmatic hydrothermal alteration. Older allanite relicts encountered in this study (allanite Type II, Figure 6) could represent unique windows to this enriched SCLM source and be a recorder of its metamorphic evolution in an environment evolving from peak compression to strike-slip motions, and of its later extension during orogenic collapse, related to mantle delamination, asthenospheric upwelling, rapid exhumation and low degree of partial melting favored by shear zones. This is supported by the similar ferriallanite–epidote composition of most allanite grains which are consistent with the nearly isochemical

evolution of a metabasic source in a nearly closed system, except for allanite Type I rims which are apparently the youngest and represent an abrupt change in thermodynamic conditions. Measured Th/La and Sm/La ratios (Figure 7c,d) are also indicative of the metamorphic origin of older grains, but we do not discount the possibility that these ratios could also be related to post-emplacement metamorphic retrogression in some of the grains, considering a rapid exhumation environment. The change from Type II to Type I allanite may also be related to a change in metamorphic conditions in the SCLM source during exhumation, or alternatively, to a change in stress conditions from dominant compression to dominant extension in the lamprophyre SCLM source. The later could explain why older allanite Type II crystals are generally rounded and anhedral while younger allanite Type I presents subhedral crystals with seemingly simple shear characteristics (Figure 2a,b). On the other hand, the unique Mn enrichment in allanite Type I rims and the higher clinozoisite component suggest a later event with a change in thermodynamic conditions that could be related to late magmatic and/or post-magmatic processes (the replacement of Mn-ilmenite by titanite as observed could be a viable mechanism to provide Mn to the system). Some unique Ti-enriched cores, revealed by PC3 of the principal component analysis, could also be associated with the latest hydrothermal processes as these are encountered in all allanite types and only in those allanite–epidote grains in which the alteration affected the internal parts of the grains (for example Figure 2f presents a high Ti core, while Figure 2d,e do not). The increase in Ti is related to increases in REEs, which suggest REEs are locally remobilized and recrystallized in hydrothermally affected cores (Figure 8c). Abundant secondary titanite suggests Ti was available during post-magmatic processes and the replacement of ilmenite by titanite—or the dissolution of Ti-rich amphiboles as observed—could be viable mechanisms to provide Ti to the system. Ti-enriched cores also present an increase in the ferriallanite component (Figure 8d), which is characteristic of hydrothermal ferriallanite [48,49]. Different concentrations of REEs, the slope and curvature in the REE patterns and the presence or absence of Eu anomalies (Figure 7) could also reflect competition between allanite and other minerals as the allanite crystals grew [15]. Therefore, the observed variations of REEs within grains and between samples may in part reflect local time-dependent changes of fluid or solid interactions of the lamprophyre magma or dykes, either in the lamprophyre's source prior to—or during—partial melting, or after consolidation in the crust.

A question remains whether the enrichment of the lamprophyre's SCLM source with rare earth elements was an ancient event that occurred before Variscan times, or whether it was the tectonic activity of the Variscan orogeny that generated lithospheric scale shear systems that allowed REE-rich fluids to penetrate the upper mantle/lower crust and crystallize as allanite in several steps during the syn- to post-collisional evolution of the mantle source. The first proposition implies the occurrence of ancient subduction-collision events, which indeed have been recorded in the area, dating from Ordovician times [52]. There is also a regional correlation in Sr and Nd isotopic compositions among the Variscan calc-alkaline lamprophyres of Western Europe that could be related to enriched mantle domains at the northern edge of Gondwana during Variscan times [6,53]. The second possibility—of a Variscan lithospheric-scale shear—implies that the oldest allanite relics could represent the beginning of the tectonic activity in the SCLM source of Les Guilleries lamprophyres during the Variscan post-collisional evolution of NE Iberia. Additionally, considering the known allanite–monazite transformations, the lack of monazite relics could also suggest a metamorphic re-equilibration of the lamprophyre's source under greenschist facies conditions after peak metamorphic conditions, consuming all monazite into allanite+apatite. Abundant apatite crystals around allanite Type I could be the result of monazite re-equilibration and dissolution. The epidote coronas around older allanite crystals (allanite Type II) may have prevented recrystallization at higher metamorphic conditions retaining previous features; therefore, it cannot be ruled out that higher metamorphic conditions were reached in the source of the lamprophyres.

Finally, it is also possible that both possibilities occurred. In this case, there would have been a recurrent recycling of rare earth elements during successive Wilson cycles, with subduction of REE-rich crustal material, REE transfer to the mantle via fluids, melts and mechanical mixing, and back up to the crust via tectonic exhumation and volcanic-magmatic systems originated from partial melting of REE-enriched mantle domains. From this discussion, it can be seen that the study of allanite crystals is a useful tool to unravel the history of deeper parts of orogenic systems.

6. Conclusions

Allanite crystals of 10–100 μm length have been identified in the matrix of late Variscan calc-alkaline lamprophyre dykes of Les Guilleries Massif (NE Variscan chain of the Iberian peninsula). Based on the complex zoning and alteration textures of the allanite crystals, two predominant types have been distinguished: Allanite Type I is found in feldspathic zones and consists of subhedral cores with regular parallel zoning that transitions smoothly into epidote; Allanite Type II corresponds to anhedral cores with irregular zoning that are in sharp contact with epidote coronas and are observed in chloritized zones. Both types show gradations from ferriallanite-(Ce) to epidote.

A principal component analysis of allanites reveals an anti-correlation between Si-Al-Ca and Fe-LREE-Ti-Mg in all grain types (PC1), which accounts for 75% of variations. PC2 relates to high concentrations of Mn in the rims of Type I, whereas PC3 is related to high Ti contents. These three principal components account for 92% of compositional differences, which can be summarized as $REE^{3+} + Fe^{2+} + Ti^{4+} + Mg^{2+} + Mn^{2+} = Al^{3+} + Ca^{2+} + Fe^{3+}$.

In situ U-Th-Pb dates of 29 analytical points in allanite crystals yield a weighted mean age of 265 ± 15 Ma. The coincidence of allanite dates in Les Guilleries lamprophyres with the period following the main syn- to post-collisional Variscan magmatism in the Catalan Coastal Range (280–250 Ma), in conjunction with the differences in allanite textures, suggest the allanite crystals from this study represent multi-stage metamorphic, magmatic and/or hydrothermal processes that occurred both before partial melting of the lamprophyre's source and later, during the early, late and post-magmatic evolution of the post-collisional system.

The low ratios of Th/U and La/Sm and variable Eu/Eu* of all analyzed allanites plot within or near the metamorphic domain. This could be due to previous ancient subduction-collision events recycling allanite, possibly in Ordovician times, or to a Variscan lithospheric-scale shear, with the oldest allanite relicts representing the beginning of the tectonic activity in the SCLM source of Les Guilleries lamprophyres (and maybe the entire Variscan collisional system of NE Iberia). In any case, recurrent recycling of rare earth elements with subduction of REE-rich crustal material into the mantle seems plausible.

Petrological, geochemical and geochronological results from this study are consistent with the interpretation that Les Guilleries lamprophyre dykes represent mantle-derived magmas that were emplaced into the brittle upper crust during late Permian times at the final stages of the Variscan orogenic collapse. This occurred in relation to shear zones, lithospheric thinning, asthenospheric upwelling, and partial melting of subduction-related enriched SCLM domains.

The Variscan basement of the Catalan Coastal Range and Eastern Pyrenees record the transition from a contractional or transpressional tectonic regime, characterized by crustal thickening, to a strike-slip regional setting that occurred during lithospheric delamination during late Variscan times, prior to the extensional collapse of the orogen and the breakup of Pangea. The results from this study suggest allanite could be a useful tool to indirectly elucidate the history of deeper parts of this system that are apparently not manifested at the surface.

References

1. Owen, J.P. Geochemistry of lamprophyres from the Western Alps, Italy: Implications for the origin of an enriched isotopic component in the Italian mantle. *Contrib. Mineral. Petrol.* **2008**, *155*, 341–362. [CrossRef]
2. Seifert, T. *Metallogeny and Petrogenesis of Lamprophyres in the Mid-European Variscides*; IOS Press: Amsterdam, The Netherlands, 2008.
3. Soder, C. Geochemistry and Petrology of Lamprophyres from the Hellenides and the European Variscides. Ph.D. Thesis, University of Heidelberg, Heidelberg, Germany, 2017.
4. Errandonea-Martin, J.; Sarrionandia, F.; Carracedo-Sánchez, M.; Gil Ibarguchi, J.I.; Eguíluz, L. Petrography and geochemistry of late- to post-Variscan vaugnerite series rocks and calc-alkaline lamprophyres within a cordierite-bearing monzogranite (the Sierra Bermeja Pluton, southern Iberian Massif). *Geol. Acta* **2018**, *16*, 237–255.
5. Le Maitre, R.; Streckeisen, A.; Zanettin, B.; Le Bas, M.; Bonin, B.; Bateman, P. (Eds.) *Igneous Rocks: A Classification and Glossary of Terms: Recommendations of the International Union of Geological Sciences Subcommission on the Systematics of Igneous Rocks*, 2nd ed.; Cambridge University Press: Cambridge, UK, 2002.
6. Mellado, E.; Corbella, M.; Navarro-Ciurana, D.; Kylander-Clark, A. The enriched Variscan lithosphere of NE Iberia: Data from post-collisional Permian calc-alkaline lamprophyre dykes of Les Guilleries. *Geol. Acta* **2021**, *19*, 1–23. [CrossRef]
7. Deer, W.A.; Howie, R.A.; Zussman, J. *Rock-Forming Minerals, Vol. 1B: Disilicates and Ringsilicates*, 2nd ed.; Longman: Harlow, UK, 1986.
8. Gieré, R.; Sorensen, S.S. Allanite and other REE-rich epidote group minerals. *Rev. Mineral. Geochem.* **2004**, *56*, 431–493. [CrossRef]
9. Armbruster, T.; Bonazzi, P.; Akasaka, M.; Bermanec, V.; Chopin, C.; Giere, R.; Heuss-Assbichler, S.; Liebscher, A.; Menchetti, S.; Pan, Y. Recommended nomenclature of epidote-group minerals. *Eur. J. Mineral.* **2006**, *18*, 551–567. [CrossRef]
10. Catlos, E.J.; Sorensen, S.S.; Harrison, T.M. Th–Pb ion-microprobe dating of allanite. *Am. Mineral.* **2000**, *85*, 633–648. [CrossRef]
11. Grapes, R.H.; Hoskin, W.O. Epidote group minerals in low-medium pressure metamorphic terranes. *Rev. Mineral. Geochem.* **2004**, *56*, 301–345. [CrossRef]
12. Finger, F.; Broska, I.; Roberts, M.P.; Schermaier, A. Replacement of primary monazite by apatite-allanite-epidote coronas in amphibolite facies granite gneiss from the eastern Alps. *Am. Mineral.* **1998**, *83*, 248–258. [CrossRef]
13. Janots, E.; Engi, M.; Berger, A.; Allaz, J.; Schwarz, J.O.; Spandler, C. Prograde metamorphic sequence of REE minerals in pelitic rocks of the Central Alps: Implications for allanite–monazite–xenotime phase relations from 250 to 610 °C. *J. Metamorph. Geol.* **2008**, *26*, 509–526. [CrossRef]
14. Janots, E.; Berger, A.; Engi, M. Physico-chemical control on the REE-mineralogy in chloritoid-grade metasediments from a single outcrop (Central Alps, Switzerland). *Lithos* **2011**, *121*, 1–11. [CrossRef]
15. Engi, M. Petrochronology based on REE-minerals: Monazite, allanite, xenotime, apatite. *Rev. Mineral. Geochem.* **2017**, *83*, 365–418. [CrossRef]
16. Goswami-Banerjee, S.; Robyr, M. Pressure and temperature conditions for crystallization of metamorphic allanite and monazite in metapelites: A case study from the Miyar Valley (high Himalayan Crystalline of Zanskar, NW India). *J. Metamorph. Geol.* **2015**, *33*, 535–556. [CrossRef]
17. Budzyń, B.; Harlov, D.; Williams, M.; Jercinovic, M. Experimental determination of stability relations between monazite, fluorapatite, allanite, and REE-epidote as a function of pressure, temperature, and fluid composition. *Am. Mineral.* **2011**, *96*, 1547–1567. [CrossRef]
18. Cenki-Tok, B.; Darling, J.; Rolland, Y.; Rossi, M.; Engi, M. Allanite Behavior in Upper-Mid Crustal Shear Zones: Can we Date Deformation Directly? Example from the Mont Blanc Massif and Implications on Its Alpine Evolution. *Terra Nova* **2011**, *0*, 1–9.
19. Levinson, A.A. A system of nomenclature for rare-earth minerals. *Am. Mineral.* **1966**, *51*, 152–158.
20. Beard, J.; Sorensen, S.; Gieré, R. REE zoning in allanite related to changing partition coefficients during crystallization: Implications for REE behaviour in an epidote-bearing tonalite. *Miner. Mag.* **2006**, *70*, 419–436. [CrossRef]

21. Klimm, K.; Blundy, J.D.; Green, T.H. Trace Element Partitioning and Accessory Phase Saturation during H_2O-Saturated Melting of Basalt with Implications for Subduction Zone Chemical Fluxes. *J. Petrol.* **2008**, *49*, 523–553. [CrossRef]
22. Hermann, J. Allanite: Thorium and light rare earth element carrier in subducted crust. *Chem. Geol.* **2002**, *192*, 289–306. [CrossRef]
23. Smye, A.; Roberts, N.; Condon, D.; Horstwood, M.; Parrish, R. Characterising the U-Th-Pb systematics of allanite by ID and LA-ICPMS: Implications for geochronology. *Geochim. Cosmochim. Acta* **2014**, *135*, 1–28. [CrossRef]
24. Oberli, F.; Meier, M.; Berger, A.; Rosenberg, C.; Gieré, R. U-Th-Pb and $^{230}Th/^{238}U$ disequilibrium isotope systematics: Precise accessory mineral chronology and melt evolution tracing in the Alpine Bergell intrusion. *Geochim. Cosmochim. Acta* **2004**, *68*, 2543–2560. [CrossRef]
25. Gregory, C.J.; Rubatto, D.; Hermann, J.; Berger, A.; Engi, M. Allanite behaviour during incipient melting in the southern Central Alps. *Geochim. Cosmochim. Acta* **2012**, *84*, 433–458. [CrossRef]
26. Janots, E.; Rubatto, D. U–Th–Pb dating of collision in the external Alpine domains (Urseren zone, Switzerland) using low temperature allanite and monazite. *Lithos* **2014**, *184–187*, 155–166. [CrossRef]
27. Reche, J.; Martínez, F.J. Evolution of bulk composition, mineralogy, strain style and fluid flow during an HT-LP metamorphic event: Sillimanite zone of the Catalan Coastal Ranges, Variscan basement, NE Iberia. *Tectonophysics* **2002**, *348*, 111–134. [CrossRef]
28. Arche, A.; López-Gómez, J. Origin of the Permian-Triassic Iberian Basin, central-eastern Spain. *Tectonophysics* **1996**, *266*, 443–464. [CrossRef]
29. Perini, G.; Cebria, J.M.; Lopez-Ruiz, J.; Doblas, M. Carboniferous-Permian mafic magmatism in the Variscan belt of Spain and France: Implications for mantle sources. *Geol. Soc. Spec. Publ.* **2004**, *223*, 415–438. [CrossRef]
30. Liesa, M.; Aguilar, C.; Castro, A.; Gisbert, G.; Reche, J.; Muñoz, J.A.; Vilà, M. The role of mantle and crust in the generation of calc-alkaline Variscan magmatism and its tectonic setting in the Eastern Pyrenees. *Lithos* **2021**, *406–407*, 106541. [CrossRef]
31. Enrique, P. The Hercynian intrusive rocks of the Catalonian Coastal Ranges (NE Spain). *Acta Geol. Hisp.* **1990**, *25*, 39–64.
32. Esteve, S.; Sunyer, J.; Culí, L.; Cirés, J.; Alías, G. El complejo intrusivo diorítico-gabroico de Susqueda (Macizo del Montseny-Guilleries, Cataluña): Unidades litológicas y características petrográficas. *Geogaceta* **2016**, *60*, 99–102.
33. Martínez, F.J.; Reche, J.; Iriondo, A. U-Pb SHRIMP-RG zircon ages of Variscan igneous rocks from the Guilleries massif (NE Iberia pre-Mesozoic basement): Geological implications. *C. R. Geosci.* **2008**, *340*, 223–232. [CrossRef]
34. Esteve, S.; Enrique, P.; Alías, G. Relaciones intrusivas y cronología relativa del plutón básico de Susqueda con las rocas metamórficas encajantes (Cordillera Prelitoral Catalana). *Geogaceta* **2018**, *63*, 107–110.
35. Martínez, F.J.; Universitat Autònoma de Barcelona, Barcelona, Spain. Personal communication, 2022.
36. Solé, J.; Cosca, M.; Sharp, Z.; Enrique, P. 40Ar/39Ar Geochronology and stable isotope geochemistry of Late-Hercynian intrusions from north-eastern Iberia with implications for argon loss in K-feldspar. *Int. J. Earth. Sci.* **2002**, *91*, 865–881.
37. Butjosa, L.; Enrique, P.; Galán, G. Las hornblenditas, gabros y dioritas del Macizo del Montnegre (Barcelona, Cordilleras Costero Catalanas). *Geogaceta* **2013**, *54*, 35–38.
38. Galán, G.; Enrique, P.; Butjosa, L.; Fernández-Roig, M. Spinels of Variscan olivine hornblendites related to the Montnegre granitoids revisited (NE Spain): Petrogenetic evidence of mafic magma mixing. *Geol. Acta* **2017**, *15*, 323–336.
39. Saxena, S.K.; Walter, L.S. A statistical-chemical and thermodynamic approach to the study of lunar mineralogy. *Geochim. Cosmochim. Acta* **1974**, *38*, 79–95. [CrossRef]
40. Ubide, T.; Gale, C.; Larrea, P.; Arranz Yagüe, E.; Lago San José, M.; Tierz, P. The Relevance of Crystal Transfer to Magma Mixing: A Case Study in Composite Dykes from the Central Pyrenees. *J. Petrol.* **2014**, *55*, 1535–1559. [CrossRef]
41. Iwamori, H.; Albarède, F. Decoupled isotopic record of ridge and subduction zone processes in oceanic basalts by independent component analysis. *Geochem. Geophys. Geosyst.* **2008**, *9*, 1525–2027. [CrossRef]
42. Spencer, K.; Hacker, B.; Kylander-Clark, A.; Andersen, T.; Cottle, J.; Stearns, M.; Poletti, J.; Seward, G. Campaign-style titanite U-Pb dating by laser-ablation ICP: Implications for crustal flow, phase transformations and titanite closure. *Chem. Geol.* **2013**, *341*, 84–101. [CrossRef]
43. Kylander-Clark, A.; Hacker, B.; Cottle, J. Laser-ablation split-stream ICP petrochronology. *Chem. Geol.* **2013**, *345*, 99–112. [CrossRef]
44. Kylander-Clark, A. Expanding Limits of Laser-Ablation U-Pb Calcite Geochronology. *Geochronology* **2020**, *2*, 343–354. [CrossRef]
45. von Blackenburg, F. Combined high-precision chronometry and geochemical tracing using accessory minerals: Applied to the Central-Alpine Bergell intrusion (central Europe). *Chem. Geol.* **1992**, *100*, 19–40. [CrossRef]
46. Petrík, I.; Broska, I.; Lipka, J.; Siman, P. Granitoid Allanite-(Ce) sub-stitution relations, redox conditions and REE distributions (on an Example of I-Type Granitoids, Western Carpathians, Slovakia). *Geol. Carpath.* **1995**, *46*, 79–94.
47. Broska, I.; Petrík, I. Accessory Phases in the Genesis of Igneous Rocks. In *Modelling of Magmatic and Allied Processes*; Kumar, S., Singh, R., Eds.; Society of Earth Scientists Series; Springer: Cham, Switzerland, 2014.
48. Vlach, S.R.F.; Gualda, G.A.R. Allanite and chevkinite in A-type granites and syenites of the Graciosa Province, southern Brazil. *Lithos* **2007**, *97*, 98–121. [CrossRef]
49. Hirtopanu, P.; Andersen, J.; Fairhurst, R.J.; Jakab, G. Allanite-(ce) and its associations, from the Ditrau alkaline intrusive massif, East Carpathians, Romania. *Proc. Rom. Acad. Series B* **2013**, *15*, 59–74.
50. Schulmann, K.; Catalán, J.R.; Lardeaux, J.; Janousek, V.; Oggiano, G. The Variscan orogeny: Extent, timescale and the formation of the European crust. In book: The Variscan Orogeny: Extent, Timescale and the Formation of the European Crust. *Geol. Soc. Spec. Publ.* **2014**, *405*, 1–6. [CrossRef]

51. Sun, S.S.; McDonough, W.F. Chemical and isotopic systematics of oceanic basalts implications for mantle composition and processes. In *Magmatism in the Ocean Basins*; Saunders, A.D., Norry, M.J., Eds.; Geological Society of London: London, UK, 1989; pp. 313–345.

52. Navidad, M.; Castiñeiras, P.; Casas, J.M.; Liesa, M.; Fernández-Suárez, J.; Barnolas, A.; Carreras, J.; Gil-Peña, I. Geochemical characterization and isotopic age of Caradocian magmatism in the northeastern Iberian Peninsula: Insights into the Late Ordovician evolution of the northern Gondwana margin. *Gondwana Res.* **2010**, *17*, 325–337. [CrossRef]

53. Dijkstra, A.H.; Hatch, C. Mapping a hidden terrane boundary in the mantle lithosphere with lamprophyres. *Nat. Commun.* **2018**, *9*, 3770. [CrossRef]

CHAPTER 4

THIRD ARTICLE

Rare earth elements and Sr-Nd isotopic compositions of fluorite from the Osor vein deposit (Catalan Coastal Ranges, NE Iberia)

Esteban Mellado [1*] and Mercè Corbella [1]

[1]   Universitat Autònoma de Barcelona, Spain; merce.corbella@uab.cat

*   Correspondence: esteban.mellado@uab.cat

Abstract: The Osor fluorite deposit, located in Les Guilleries Massif (CCR, NE Iberia) and hosted in Lower Paleozoic rocks, is mineralogically similar to other late- to post-Hercynian mineral systems of this type in Europe. The Osor deposit consist of MVT-like fluorite-barite veins with sphalerite and galena crosscutting Variscan porphyritic granites and metapelites. These veins show different stages of recrystallization that have been attributed to Variscan movements and subsequent rejuvenation during the Alpine orogeny. In this study, chemical REY and Sr-Nd isotopic data indicate that total REY content ranges between 127 and 247 ppm, with $^{87}Sr/^{86}Sr$ ratios between 0.71290 and 0.71308 and $^{143}Nd/^{144}Nd$ ratios between 0.51238 and 0.0.51247. PAAS-normalized REY patterns show enrichment in MREE with depletion in LREE and HREE, and a characteristic Eu and Y positive anomalies. These patterns combined with Sr-Nd isotopic concentrations suggest large-scale fluid convection interacted with a basement dominated by metamorphic rocks. Four-point Sm-Nd isochrones with acceptable values of MSWD ~1 gave 224±85 (MSWD = 1.3) and 58±44 (MSWD=0.99) Ma ages, which are consistent with its relation with Variscan and Alpine tectonic events; however the error is too high for establishing absolute dates of mineralization.

Keywords: Fluorite, rare earth elements, Sr-Nd isotopes, Osor, Catalan Coastal Ranges.

1. Introduction

The concentration of rare-earth elements and yttrium (REY) in mineral phases have become a powerful tool in studying the genesis of hydrothermal ores (Bau and Dulski, 1995; Schwinn and Markl, 2005). Particularly in fluorite (CaF_2), REY patterns and Sr-Nd isotopic compositions are usually preserved and can be used as fingerprints of the hydrothermal fluid from which they precipitated and, hence, can be used as reliable geochemical archives to reconstruct the physicochemical parameters of ancient and modern hydrothermal systems (Bau and Dulski, 1995, Schwinn and Markl, 2005). REY are strongly complexed with fluoride in F-rich hydrothermal fluids, which may lead to a significant enrichment of REY in F-bearing hydrothermal fluids and in fluorite (Moller et al 1998; Bau et al., 2003). The analysis of REY provides important information on metal sources, temperature conditions, fluid migration, host rock interaction and the chemical composition of the fluid phase (Bau et al., 2003, Schwinn and Markl, 2005, Castorina et al., 2008, Sánchez et al., 2010). Understanding ancient and modern hydrothermal systems and their specific chemistries is essential for constructing accurate and detailed models for ore deposit formation, which in turn may facilitate the discovery of other mineral deposits.

Fluorite-rich veins are widespread in the Variscan basement of Central and Western Europe. Important examples are found in the Massif Central (Sizaret et al., 2004), in the Hercynian massifs of Spain (Galindo et al., 1994, Piqué et al., 2008, Sánchez et al., 2019) and of Germany (Schwinn and Markl, 2005), Sardinia (Castorina et al., 2008), Pyrenees (Subías et al., 2015). Muchez et al. (2005) suggest that the major basin-hosted deposits in Europe are related to extensional tectonics and that the mineralizing fluids, which originated as (evaporated) seawater, intruded downward into the basin through interconnected fractures. The ore-bearing fluids would then be expelled along extensional faults in regions characterized by pronounced extension and heat production.

In this study, fluorites from the Osor deposit were investigated for their REY content, age and possible relation with other hydrothermal manisfestations as alteration in lamprophyres and porphyritic granites nearby (Figure 1, Mellado et al. 2021). Campà y Monturiol (1974) showed that Osor fluorite mineralization occurred as precipitates in fluid-filled fractures in an E-W compressive-distensive system hosted by schist and in some cases coexist with pegmatites (Amigó and Font-Altaba, 1966a,b). The three major mineral species are fluorite, sphalerite and galena, with minor calcite, pyrite, marcasite, barite and quartz (Amigó and Font-Altaba, 1966b). Barite is present in small amounts in the upper levels of the mine, whereas galena and sphalerite are more abundant at depth. Fluorite presents irregular textures and appear crushed with cracks filled by quartz. Only in some parts of the higher plants

can it be observed some stratification into light and dark bands. Sulphides occur within fluorite mineralization, forming pockets or irregular masses. According to Font (1983), homogenization temperatures in fluid inclusions from these fluorites are lower than 100°C (between 60 and 95°C). No data on the salinity of the fluids are available.

The mineralization in the Osor fluorite deposit is considered a fluorine-bearing sub-type of Mississippi Valley Type (MVT) mineralization (Colman et al., 1989). Mississippi-Valley-Type mineralization usually forms through precipitation from mildly hot hydrothermal basinal brines (100–200 °C) with relatively high fluid salinities (15–25 wt-% NaCl equivalent; Leach et al., 2001). These epigenetic ore deposits form predominantly in dolostone, but also in limestone and sandstone, and are globally important sources of lead and zinc sulphides; occasionally MVT deposits are significantly enriched in fluorite (Leach et al., 2001). MVT mineralization usually lacks a genetic affinity to igneous activity (Leach et al., 2001. In the CCR, other well studied Mesozoic fluorite–barite–base metal veins hosted in the crystalline basement are Rigròs and Berta. The Sm–Nd age of Rigròs (137 ±25 Ma) places the ore formation during the Late Jurassic–Early Cretaceous rifting episode in the western European basins, which is in turn related to the opening of the North Atlantic Ocean (Piqué et al. 2008). Similar Sm–Nd ages of of 145 ± 18 have been found in F-Ba-base metals veins in Sierra de Guadarrama in the Spanish Central System (Galindo et al. 1994), and 185 ± 28 Ma in vein and stratabound fluorite deposits from Asturias (Sánchez et al. 2010). In the central Pyrenees, Subías et al. (2015) suggested vein and MVT deposits formed around 260 and 220Ma respectively. In the CCR temperature conditions were constrained from fluid inclusion microthermomtry measurements in fluorite-barite veins (Canals and Cardellach 1997; Cardellach et al. 2002; Piqué et al. 2008). In the Central Catalan Coastal Ranges, i.e., in Berta and Rigròs mines, temperatures recorded in the Mesozoic veins range between 80 and 230 °C, whereas Miocene veins formed between 100 and 150 °C (Cardellach et al. 2002; Piqué et al. 2008). Moreover, fission-track data in the CCR (Juez-Larré 2003) provided constrain on the minimum temperature during the Mesozoic and the Neogene corresponding to the closure temperature of apatites and zircons. Temperature was found to drop from T > 200 °C before Mesozoic to the closure temperature of zircon during Mesozoic and down to the closure temperature of apatite (100 °C) during the Miocene. The above-mentioned data provide a general framework, but a more detailed evolution of fluorite mineralization linked to different tectonic events still remains to be done. In the present study, the combination of REY geochemistry and Sr-Nd isotopic composition in the Osor fluorite deposit is used to get insights on metal and fluid sources, precipitation conditions, fluid pathways and host rock interaction.
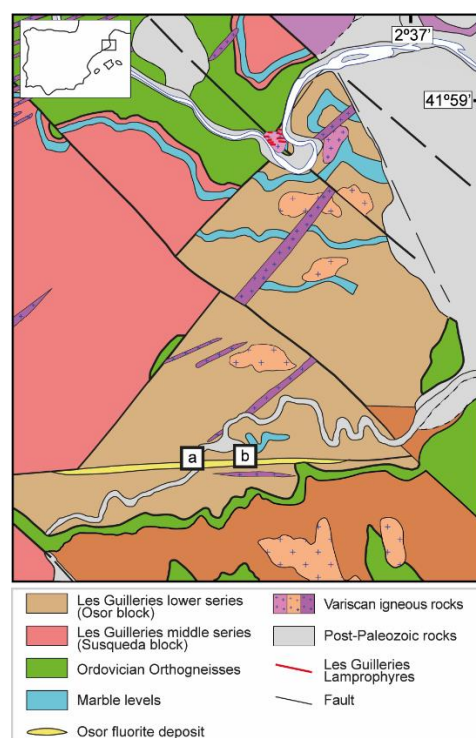

Figure 1. Detailed geological map of the study area and location of Osor fluorite deposit (Map derived from l'Institut Cartogràfic de Catalunya (ICGC) Mapa geològic comarcal 1:50.000 (CCBY4.0, 2016)).

2. Materials and Methods

Green and white fluorite samples were collected from dumps close to the abandoned Osor mine and few samples were taken from in situ massive white fluorite near the dumps Additionally, two other samples were collected in fluorite veins also hosted by pre-Mesozoic metamorphic and crystalline basement, one in Cap Gros 70km to the NE from Osor deposit, and the other from Mina Gato, 30km to the SW from Osor. These two plus seven representative samples from the Osor deposit (green and white fluorite) were crushed, separated by hand-picking, pulverized to 200μm and sent to ACTLABS, Ontario (Canada), for whole-rock geochemical analysis of 51 elements, including rare earth elements and yttrium (REY). The analytical techniques used were lithium metaborate/tetraborate fusion with subsequent analysis by Ion Selective Electrode (ISE) for fluorine and Inductively Coupled Plasma Mass Spectrometry (ICP-MS) for the rest of the elements (SiO_2, TiO_2, Al_2O_3, Fe_2O_3, MnO, MgO, CaO, Na_2O, K_2O, P_2O_5, Li, Be, Sc, V, Cr, Co, Ni, Cu, Zn, Ga, Ge, Rb, Sr, Y, Zr, Nb, Sn, Cs, Ba, La, Ce, Pr, Nd, Sm, Eu, Gd, Tb, Dy, Ho, Er, Tm, Yb, Lu, Hf, Ta, W, Tl, Pb, Th and U). Detection limits and analytical errors are presented in Table 1.

For the same fluorite samples of the Osor deposit, in addition to two samples recovered from the Museu de Ciències Naturals de Barcelona (Samples F_4168 and F_2905), Sr-Nd isotopic analyses were carried out at the Geochronology Unit of Universidad Complutense de Madrid (UCM). For $^{87}Sr/^{86}Sr$, a mass spectrometer VG Sector-54® was used, following data acquisition method of dynamic multicollection during 10 blocks of 16 cycles each, with beam intensity of 3V. Isotopic standards used were NBS 987 ($^{87}Sr/^{86}Sr$= 0.710248±0.000003, National Bureau of Standards Certificate of Analysis). For $^{143}Nd/^{144}Nd$ mass spectrometer TIMS-Phoenix® was used, following data acquisition method of dynamic multicollection during 160 cycles with beam intensity of 1V. Isotopic standard used was JNdi-1 ($^{143}Nd/^{144}Nd$= 0.512115±0.000002; Tanaka et al., 2000). Analytical errors referred to two standard deviations are 0.0004% for $^{87}Sr/^{86}Sr$ and 0.0003% for $^{143}Nd/^{144}Nd$.

3. Geological setting

The abandoned Osor mining area (Fig. 1) lies some 35 km SE of Girona, in the Montseny-Guilleries massif, which forms part of the Catalonian Coastal Ranges (CCR) in the NE section of the Iberian Peninsula. The massif is composed of three blocks separated by NE-SW striking normal faults. The deeper and higher-grade metamorphic block, the Osor block, outcrops in the southern part of the massif and contains sillimanite grade metapelites with interlayered metapsammites, calc-silicates, amphibolites, and orthogneisses (Durán, 1990; Reche and Martínez, 2002). The Susqueda block is the intermediate one, which is composed of metapelites and metapsammites with quartzite layers and represents shallower levels of the crust, as the metamorphism reaches the andalusite-cordierite grade. The Osor and Susqueda blocks contain sill-like bodies of orthogneisses that record essentially continuous magmatic activity beginning at the Cambro-Ordovician boundary (488±3Ma) and reaching a peak of intrusions volume during the late Ordovician (462±8 to 459±3Ma; Martínez et al., 2011). The northern and uppermost Sant Martí block is composed of Ordovician metavolcanic rocks interbedded with metagreywackes and metapelites (U-Pb age 452±4Ma; Martínez et al., 2011). Some Silurian and Devonian volcanosedimentary rocks also crop out in the northern part, although the sequences appear incomplete due to faulting (Durán, 1990).

Felsic and mafic igneous rocks of Late Carboniferous–Early Permian age and syn- to post-collisional of calc-alkaline affinity outcrop in the area, some of them dated at 323.6 ± 2.8 Ma (diorites; Martínez et al., 2008), 305-299Ma old (U-Pb zircon ages in granite; Martínez et al., 2008), 291 and 285Ma (40Ar/39Ar ages in felsic plutonic bodies in the nearby Montnegre Massif, Solé et al., 2002). Finally, Les Guilleries lamprophyre dykes crosscut all previous sequences including schist and marbles from the basement and Variscan leucogranites, granodiorites, quartz-monzonites and pegmatites. Titanite U-Pb dating of the lamprophyres yields a concordia age of 262 ± 7 Ma, which place these dykes as the youngest calc-alkaline mafic intrusion found in the area related to the fragmentation of the Variscan Belt (Mellado et al 2021).

This Variscan post-collisional magmatic system is considered to have formed from variable degrees of lower crustal assimilation and differentiation and were emplaced in the mid–upper Variscan crust in a local predominantly extensional context. They are linked to a regional dextral strike-slip regime related to late-Variscan shear zones that must have displaced Gondwana to the west with respect to Laurasia during orogenic collapse (Liesa et al. 2021). The mafic complexes are suggested to have derived from a mantle source enriched in LILEs and LREEs, attributed to metasomatic processes of the lithospheric mantle during previous subduction events (Liesa et al. 2021; Mellado et al., 2021).

Several types of ore mineralizations have been found in Les Guilleries (Ayora, 1990). Epigenetic mineralizations, mainly skarns (Cu, Fe, Zn, Pb) and veins (F, Ba, Zn, Pb), seem to be related to hydrothermal fluid circulation induced by the post-metamorphic granitic intrusions (Ayora, 1990). The most important deposit occurs in the Osor block and consists of fluorite-barite veins with sphalerite and galena crosscutting Variscan porphyritic granites and metapelites. These veins show different stages of recrystallization that have been attributed to Variscan movements and subsequent rejuvenation during the Alpine orogeny (Campá-Viñeta and Montoriol-Pous, 1974).

125   The pre-Mesozoic basement is unconformably covered by sequences of Mesozoic sediments, which consist of Triassic si-
126 liciclastics, carbonates and evaporites, followed by Jurassic and Cretaceous shallow water carbonates. In the Mesozoic two major
127 rifting events were recorded, the first occurred during the late Permian-Hettangian and the second one during the late Oxfordian-
128 Albian (Salas et al., 2001). Cenozoic materials comprise detrital sediments, mainly filling the Neogene basins. During the Eocene to
129 early Oligocene, the Pyrenean orogeny produced a tectonic inversion, with the development of thrust sheets. The present geo-
130 graphic features of the ranges, subdivided in two main horsts and several grabens, were acquired during the opening of the Valencia
131 trough, from the late Oligocene to the early Miocene (Roca et al., 1999).

132 **4. Results**

133 *4.1. REY geochemistry*

134   Fluorite samples from the Osor deposit are characterized by total REY concentrations ranging from 128 ppm to 248 ppm,
135 where green fluorite presents higher concentrations than white fluorite. REY contents (Table 1) normalized to the post-Archean
136 Australian Shale (PAAS; Taylor and McLennan, 1985) are compared with data of other deposits of the same type. The PAAS-normal-
137 ized REY patterns shown in Figure 2 are similar for Osor's green and white fluorite, with enrichment of the middle REY (MREE: Eu to
138 Dy) over light (LREE: La-Sm) and heavy REY (HREY: Ho-Lu), and Y/Ho fractionation observed in all samples. LREE and HREE in Osor
139 fluorite are generally lower than PAAS, while MREE are higher than PAAS. It is possible to observe that the REE concentrations
140 normalized to PAAS have a roof-shaped pattern, characterized by positive Eu and Y anomalies (Fig. 7A). Osor fluorites have similar
141 REY patterns than Cap Gros fluorite, expect for the latter having a negative Eu anomaly and lower total REY (100ppm). On the other
142 hand, Mina Gato fluorite presents the highest total REY concentration of 528ppm, with roughly similar patterns but with Eu and Y
143 anomaly not as pronounced as in Osor. Osor fluorite are also strikingly similar to homologous fluorite veins hosted in the Paleozoic
144 basement of Sardinia.

145
146
147
148
149
150
151
152
153
154
155
156
157
158
159
160
161
162
163
164
165
166
167
168
169
170
171
172
173
174

175
176
Table 1. La-ICP-MS chemical data of Osor fluorite samples. Green fluorite: GI-14b, GI-15a, GI-15d, GI-32, GI-33, F_4168. White fluorite: GI-14a, GI-14c, GI-34, F_2905. Mina Gato: GA-100. Cap Gros: CG-101.

|	Method	DT	Unit	GI-14b	GI-15d	GI-30	GI-32	GI-34	V-2104381	B-2104382	GA-100	CG-101
SiO2	FUS-ICP	0.01	%	36500	24300	57000	29500	65200	61500	36500	26900	2000
Al2O3	FUS-ICP	0.01	%	400	600	100	700	100				
Fe2O3(T)	FUS-ICP	0.01	%	100	100	100	100	100	760	190		
MnO	FUS-ICP	0.001	%	40	40	30	5	5				
MgO	FUS-ICP	0.01	%	100	100	100	100	100				
CaO	FUS-ICP	0.01	%	701200	707800	694000	709600	681800	668850	621000	674500	710700
Na2O	FUS-ICP	0.01	%	100	100	200	200	200			320	
K2O	FUS-ICP	0.01	%	100	100	<100	200	<100				
TiO2	FUS-ICP	0.001	%	10	10	<10	<10	<10				
P2O5	FUS-ICP	0.01	%	300	200	200	200	100				
LOI	GRAV		%	15300	17000	13300	11300	17600	59700	42800	33100	16700
Total	FUS-ICP	0.01	%	754400	750300	764900	751900	765400	790810	700490	734819.9	729399.9
F	FUS-ISE	0.01	%	440000	447000	435000	433000	425000	419400	399500	444200	466600
Sc	FUS-ICP	1	ppm	<1	<1	<1	<1	<1				
Be	FUS-ICP	1	ppm	<1	<1	<1	<1	<1	0.3	0.2	4.0	0.1
V	FUS-ICP	5	ppm	<5	<5	<5	<5	<5	10			
Cr	FUS-MS	20	ppm	<20	<20	<20	<20	<20	34	4	4	1
Co	FUS-MS	1	ppm	<1	<1	<1	<1	<1	2.2	0.4	0.6	0.1
Ni	FUS-MS	20	ppm	<20	<20	<20	<20	<20	22	2	2	
Cu	FUS-MS	10	ppm	<10	<10	<10	<10	<10	10	2	4	2
Zn	FUS-MS	30	ppm	220	120	40	170	40	4350	1896	15	8
Ga	FUS-MS	1	ppm	<1	<1	<1	<1	<1	2.6	0.7	0.8	0.1
Ge	FUS-MS	0.5	ppm	<1	<1	<1	<1	<1	1.4	0.3	1.3	0.1
As	FUS-MS	5	ppm	<5	<5	<5	<5	<5		2	1	1
Rb	FUS-MS	1	ppm	<2	<2	<2	<2	<2	1.4	0.3	0.3	0.2
Sr	FUS-ICP	2	ppm	22	25	38	27	38	32	825	214	13
Y	FUS-MS	0.5	ppm	124	118	96	157	93	119	87	250	72
Zr	FUS-ICP	1	ppm	<4	<4	<4	<4	<4	9	6	8	5
Nb	FUS-MS	0.2	ppm	2	1	1	1	<1	0.13	0.02	0.04	
Mo	FUS-MS	2	ppm	<2	8	<2	2	<2	5			
Ag	FUS-MS	0.5	ppm	<0.5	<0.5	<0.5	<0.5	<0.5				
In	FUS-MS	0.1	ppm	<0.2	<0.2	<0.2	<0.2	<0.2				
Sn	FUS-MS	1	ppm	<1	<1	<1	<1	<1				
Sb	FUS-MS	0.2	ppm	<0.5	<0.5	<0.5	<0.5	<0.5	15.2	0.5	0.3	0.2
Cs	FUS-MS	0.1	ppm	<0.5	<0.5	<0.5	<0.5	<0.5			0.04	
Ba	FUS-ICP	2	ppm	8	4	<3	24	<3	183	45181	10132	
La	FUS-MS	0.05	ppm	4.8	4.1	5	6.7	5	6.4	3.5	18.5	1.3
Ce	FUS-MS	0.05	ppm	12.3	10.9	12.6	17.9	12.5	15.1	8.0	63.9	3.9
Pr	FUS-MS	0.01	ppm	2.12	1.96	2.07	2.96	2.09	2.2	1.3	12.7	0.7
Nd	FUS-MS	0.05	ppm	12.7	13.4	12.7	17.3	12.1	12.8	8.6	73.5	5.0
Sm	FUS-MS	0.01	ppm	5.9	6.5	4.7	7.8	4.7	5.2	3.7	28.0	2.9
Eu	FUS-MS	0.005	ppm	3.02	3.22	1.9	4.01	1.91	2.3	2.0	7.6	0.4
Gd	FUS-MS	0.01	ppm	10.8	10.8	7.3	12.9	7	8.1	5.8	29.8	5.0
Tb	FUS-MS	0.01	ppm	1.6	1.5	1	2	1	1.2	0.7	4.2	0.8
Dy	FUS-MS	0.01	ppm	8.7	7.8	5.5	11.4	5.4	7.2	4.1	22.9	4.6
Ho	FUS-MS	0.01	ppm	1.5	1.3	1	1.9	1	1.4	0.8	4.2	0.9
Er	FUS-MS	0.01	ppm	3.1	2.8	2.4	3.9	2.3	2.8	1.7	8.7	1.8
Tm	FUS-MS	0.005	ppm	0.28	0.23	0.21	0.35	0.2	0.2	0.1	0.8	0.1
Yb	FUS-MS	0.01	ppm	1.1	0.9	0.8	1.4	0.8	0.9	0.5	3.4	0.5
Lu	FUS-MS	0.002	ppm	0.11	0.09	0.08	0.11	0.08	0.1	0.1	0.4	0.1
Hf	FUS-MS	0.1	ppm	0.4	0.2	<0.2	0.2	<0.2	0.2	0.1	0.2	0.1
Ta	FUS-MS	0.01	ppm	0.3	0.3	0.3	0.4	0.3	0.1	0.1	0.2	0.1
W	FUS-MS	0.5	ppm	<1	<1	<1	<1	<1			1	
Tl	FUS-MS	0.05	ppm	0.1	<0.1	<0.1	<0.1	<0.1				
Pb	FUS-MS	5	ppm	8	2.5	62	60	51	1211	201	597	2
Bi	FUS-MS	0.1	ppm	0.2	0.2	0.2	0.2	0.2			0.1	
Th	FUS-MS	0.05	ppm	<0.1	0.1	<0.1	<0.1	<0.1	0.15	0.05	0.22	0.07
U	FUS-MS	0.01	ppm	<0.1	<0.1	<0.1	<0.1	<0.1	0.11	0.04	0.23	
ΣREE	FUS-MS	0.01	ppm	192.03	183.5	153.26	247.63	149.08	185.34	127.72	528.26	99.48

177
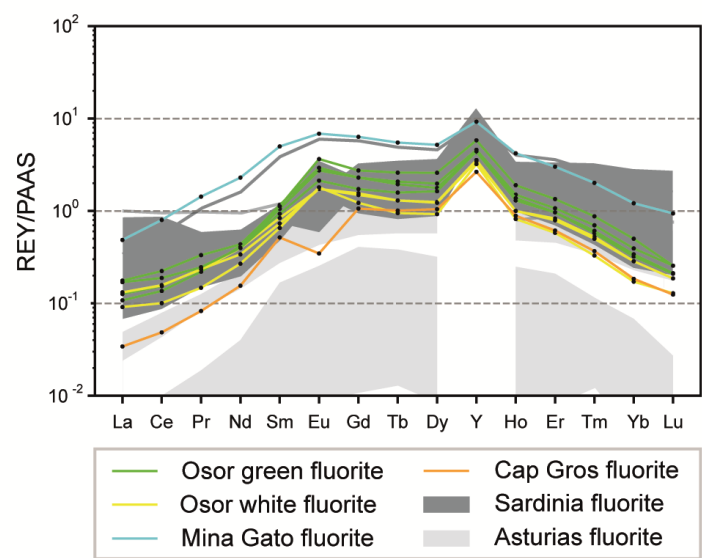
Figure 2. REE concentrations in fluorite samples, normalized to PAAS (post-Archean Australian Shale; Taylor and McLennan, 1985). Dark grey fluorite from Sardinia (Castorina et al., 2008). Light grey fluorite from Asturias (Sanchez et al., 2010).

4.2. Sr-Nd isotope results

$^{87}Sr/^{86}Sr$ ratios of the seven fluorite samples from Osor deposit are presented in Table 2. The strontium ratios of fluorite samples are slightly variable, between 0.712693 to 0.71308, and green fluorite presenting always higher values than white fluorite (Table 2) (green> 0.71299 and white fluorite always <0.71291). These values are higher than the ones reported in Triassic to Early Jurassic Atrevida and Rigròs fluorite veins always below 0.7123, and lower than those of Miocene age in Berta mine (up to 0.7168) (see Canals and Cardelach (1993)). On the other hand, these values are similar to Parzan fluorites, in the Spanish Central Pyrenees, that ranges between 0.71236 and 0.71339.

Table 2. Sr-Nd isotopic data of Osor fluorite samples. Green fluorite: GI-14b, GI-15a, GI-15d, GI-32, GI-33, F_4168. White fluorite: GI-14a, GI-14c, GI-34, F_2905.

	GI-14a	GI-14b	GI-14c	GI-15a	GI-15d	GI-32	GI-33	GI-34	F_4168	F_2905
Sr [ppm]		22			25	27		38		
$^{87}Sr/^{86}Sr$	0.712734	0.712994	0.712693	0.713026	0.713031	0.713085	0.713084	0.712903		
Sm [ppm]	4.27	3.93	4.13	3.72	4.49	4.77	5.27	3.49	3.93	3.23
Nd [ppm]		8.56		7.52	9.22	10.59	11.68	9.60	9.14	5.55
$^{147}Sm/^{144}Nd$		0.2772		0.2993	0.2942	0.2725	0.2727	0.2197	0.2603	0.3522
$^{143}Nd/^{144}Nd$		0.512398		0.512337	0.512387	0.512387	0.512276	0.512475	0.512303	0.512420
NdError*10-6		3		2	2	4	10	2	1	2

Sm and Nd isotopic analyses were carried out on 10 samples, but some white fluorite samples had too low Sm and Nd content to be measured, and therefore white fluorite is underrepresented. Sm and Nd concentrations of analyzed fluorite range between 3.23-5.22 and 5.55-11.67, respectively. The $^{147}Sm/^{144}Nd$ ratios scatter between 0.21 and 0.35 irrespective of their color (Figure 3a). Due to the scatter in Sm and Nd isotopic ratios, it is not possible to define a single Sm–Nd isochron. However, when compared to Sm-Nd data from Rigròs fluorite isochrones that yield an age of 137 ± 25 Ma (2ơ) (MSWD = 0.40), it is observed that some Osor fluorites must be older than that date, while others must be younger, which is consistent with previous interpretations that Osor fluorites were affected by Hercynian and Alpine tectonic events. Moreover, two 4 point isochrones with acceptable values of MSWD ~1 gave 224±85 (MSWD = 1.3) and 58±44 (MSWD=0.99), although the error is too high for establishing absolute dates of mineralization (Figure 3b). Which also means that the Sr–Nd isotopic data cannot be corrected to their initial isotopic values and use it to accurately constrain the source.
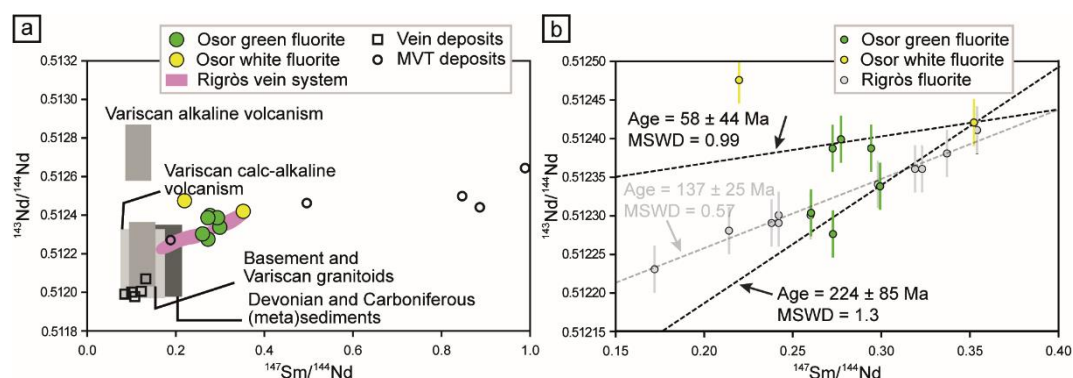
Figure 3. Plot of a) $^{147}Sm/^{144}Nd$ vs. $^{143}Nd/^{144}Nd$. potential source reservoirs of fluorite MVT deposits in Central Pyrenees described by Subías et al. 2015 (and references therein). b) Sm–Nd isochron from Osor fluorites and Rigros vein system (Piqué et al 2008). Isochron age calculated with Isoplot 3.7. See text for explanation.

5. Discussion

MVT deposits are commonly defined as epigenetic (they formed after the rocks that host them) hydrothermal ore deposits in which lead and zinc are the major commodities. These deposits are characterized by low temperatures of formation (50°–200°C, but usually 100°–150°C). They exhibit stratigraphically controlled emplacement within restricted dolostone or limestone strata (and rarely sandstone) of sedimentary basins. Mineralization occurs mostly as open-space fillings, collapse and solution breccias, and/or replacement of the carbonate host rock. Less commonly, minerals may occupy primary carbonate porosity (e.g., Hansonburg mining district). Ore and gangue precipitation is from highly saline basinal brines, with approximately 10–30 weight-percent dissolved salts. They are also typically found far from, and lack a genetic relationship to, igneous activity or igneous rocks. The most abundant ore minerals in MVTs are sphalerite (Zn) and galena (Pb). Other common minerals include pyrite, marcasite, dolomite, calcite, quartz, and occasionally barite, fluorite, celestine, gypsum, anhydrite, native sulfur, and pyrrhotite.

Although most MVTs share the common features listed above, if one looks in detail at these deposits, it becomes apparent that there is a great diversity in characteristics (i.e., the ratio of Pb to Zn, the dominant gangue minerals, the exact style of emplacement, trace-element and isotope chemistry, and so on) and possibly their origins. The differences and similarities have been the subject of numerous studies, and many scientists have grouped MVTs into subclasses, whereas others have considered diversity one of the characteristic features of these deposits. A common division of different MVT deposits includes the Pb-rich subtype, Zn-rich subtype and the fluoritic subtype (Fisher et al, 2013). In the fluoritic subtype, F concentrations are so high that fluorite is the dominant gangue mineral or may be present in economic concentrations as an ore of F. This is in contrast to the scarcity or absence of fluorite in many MVTs. The source of the anomalously high concentrations of F in these deposits has been the topic of serious interest and debate and may be related to igneous activity in some districts. The features that set the fluoritic subtype apart from typical MVT deposits (F concentration, the possible relationship to igneous activity, and so forth) are distinct enough that some authors consider them a separate type of deposit (Fisher et al, 2013).

Several hypotheses have been proposed for the source of F in MVT deposits, including leaching of F-rich igneous rocks by the basinal brines associated with MVT formation (Sánchez et al. 2009); the addition of F in a gaseous form, HF, from mantle-derived magmas, to basinal fluids (Plumlee et al., 1995); and the addition of F from degassing crustal magmas (Van Alstine, 1976). Sanchez et al. (2010) showed that in different fluorite deposits in the same region, with the same geological framework, the variability in sources and processes can led to each area having its own distinctive characteristics in terms of REY content and Sr-Nd isotopic compositions. They also show that variation in Sr isotopic data is compatible with mixing between seawater and evolved ground-water that interacted with basement rocks.

This seems to be the case in the CCR, where Osor fluorite present higher Sr ratios than most mesozoic veins. A similar REY pattern suggests similar fluids were involved in the mineralization processes, where apparently white fluorite could be a diluted version of green fluorite without significant fractionation in any element. The consistency of REY and Sr-Nd isotopic compositions between different samples suggest large scale homogenization of the fluids prior to crystallization. The roof shaped REY patterns with Eu and Y anomalies suggest that leaching of gneiss and metamorphic rocks predominate over the crystalline basement as the main source of mineralizing elements in the fluids. However, considering the great diversity of metamorphic and igneous rocks surrounding the Osor deposit in the same structural system, averages of more than one source is probable for the final fluid composition. Tb/La-Tb/Ca diagram after Möller et al. (1998) suggest an hydrothermal origin of Osor fluorite samples, that when combined with Cap Gros and Mina Gato's data present a NE-SW trend from sedimentary to hydrothermal to pegmatitic enviroments, apparently also related to increasing REY content (Figure 4). Y vs Yb diagram of Makin show that Osor fluorite deposits display

elevated Y and Yb contents with respect to other fluorite MVT deposits. The Y - Yb diagram represents the most straightforward method for the exploration industry to distinguish between fluorite grains from carbonatite and MVT, which could be indicating some REY mineralizing potential towards de SW of the CCR in the fluorites hosted in the pre-Mesozoic metamorphic basement.
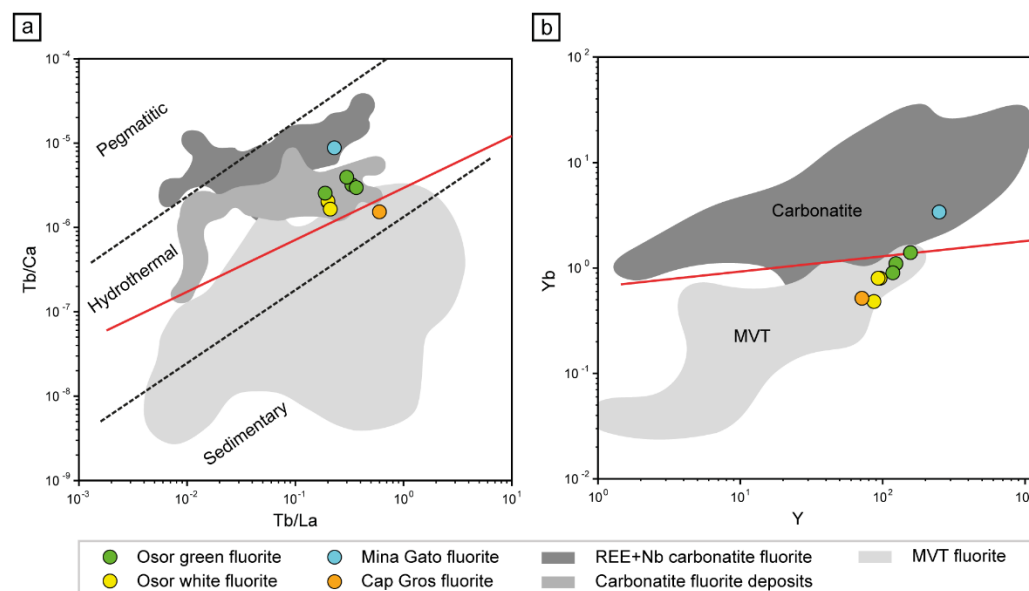

Figure 4. (a) Tb/La-Tb/Ca diagram after Möller et al. (1998). (b) Y-Yb plot for fluorite from carbonatite and MVT deposits. The carbonatite-related fluorites define a trend with a shallow positive slope and have higher concentrations of Yb than fluorites from MVT deposits. The solid red line defines the boundary between MVT-related fluorite and carbonatite-related fluorite (Makin et al., 2014).

Most hydrothermal activity in Catalan Coastal Ranges has been linked to tectonic events occurring between the Variscan and Alpine orogenies. The end of the Variscan orogeny in the CCR is marked by the last magmatic pulse with a calc-alkaline geochemical signature, namely Les Guilleries lamprophyres with U-Pb titanite date of 262±7Ma. These mafic dykes were emplaced in the upper Variscan crust after the main syn- to post-collisional magmatism, which contain evolved batholitic-sized calc-alkaline granitoids, minor mafic intrusions with local ultramafic cumulates, and peraluminous leucogranite bodies, emplaced in the lower Paleozoic basement of Les Guilleries (which host the Osor fluorite deposit). These occurred in an environment evolving from peak compression to strike-slip motions, to later extension during orogenic collapse, and related to mantle delamination, asthenospheric upwelling and rapid exhumation. An enriched SCLM origin has been inferred indirectly for the most mafic components of the post-collisional magmatic system, indicating a direct fluid pathway between mantle and crustal fluids during the orogenic collapse, which was also cogenetic with volcanism in pull-apart basins evolving from calc-alkaline-to-alkaline geochemistry during Permian times (Arche et al 1999), followed by post-orogenic hydrothermal activity. Recent studies have suggested that an albitization event developed under low-temperature subsurface conditions previous to erosion that led to the Lower Triassic paleosurface (Fàbrega et al., 2019; Parcerisa et al., 2010). Mellado et al. (2021) pointed out that a similar hydrothermal event affected Les Guilleries lamprophyres producing intense albitization and remobilizing elements like Ba, F, Pb, Zn, the same elements that are concentrated in nearby Osor fluorite deposit. This led to the suggestions that the same event that formed Osor fluorite deposits affected Les Guilleries lamprophyres, indicating and upper limit to the age of Osor deposit (262±7Ma). This is consistent with the Sm-Nd isochrones age of 224±85Ma.

6. Conclusions

Fluorite samples from the Osor deposit display maximum REY values of 258ppm and consistent PAAS normalized REY patterns with depletions of LREE and HREE, enrichment in MREE, Eu and Y positive anomalies. Tb/Ca vs Tb/La as well as Y vs Yb diagrams corroborate the hydrothermal origin proposed in previous studies, and also its MVT affinity. These patterns suggest large scale fluid circulation and homogenization prior to deposition, with metamorphic rocks as the main source of mineralizing elements, and probable contributions from the Variscan crystalline basement. Field relations combined with Sm-Nd isotopic compositions restrain the age of Osor fluorite deposits: they are younger than 262 ±7 Ma, older than 137 ±25 Ma, and most probably formed in the Lower Triassic; however, younger Osor fluorite ages indicate a much younger mineralizing event during Miocene times.

277

281 **References**

282   Amigó, J.M., Font-Altaba, M., 1966a. Estructura del yacimiento de fluorita de Osor (Gerona). Estudios Geológicos 22, 151-165.

283   Amigó, J.M., Font-Altaba, M., 1966b. Contribución al conocimiento mineralogenético del yacimiento de fluorita de Osor. Estudios Geológicos 22, 167-170.

284   Ayora, C., Soler, A., Melgarejo, J.C., 1990. The Hercynian ore deposits from the Catalonian Coastal Ranges. Acta Geologica Hispanica, 25, 65-73.

285   Bau, M., Dulski, P., 1995. Comparative study of yttrium and rare earth element behaviours in fluorine-rich hydrothermal fluids. Contributions to Mineral Petrology, 119, 213–223.

286   Bau, M.; Romer, R.L.; Lüders, V.; Dulski, P., 2003. Tracing element sources of hydrothermal mineral deposits: REE and Y distribu-tion and Sr-Nd-Pb isotopes in fluorite from MVT

287   deposits in the Pennine Orefield, England. Mineral Deposits, 38, 992–1008.

288   Campá-Viñeta, J.A., Montoriol-Pous, J. 1974. Mineral orogénesis del yacimiento de Osor (Gerona). Acta Geológica Hispánica, 9(4), 139-141.

289   Canals, À., Cardellach, E., 1997. Ore lead and sulphur isotope pattern from the lowtemperature veins of the Catalonian Coastal Ranges (NE Spain). Mineralium Deposita 32 (3),

290   243–249.

291   Cardellach, E., Canals, À., Grandia, F., 2002. Recurrent hydrothermal activity induced by successive extensional episodes: the case of the Berta F-(Pb–Zn) vein system (NE Spain).

292   Ore Geology Reviews 22 (1–2), 133–141.

293   Castorina, F., Masi, U., Padalino, G., Palomba, M., 2008. Trace-element and Sr–Nd isotopic evidence for the origin of the Sardini-an fluorite mineralization (Italy). Applied Geo-

294   chemistry, 23(10), 2906–2921.

295   Durán, H., 1985. El Paleozóico de les Guilleries. Doctoral Thesis. Bellaterra (Spain), Universitat Autònoma de Barcelona, 243pp.

296   Fàbrega, C., Parcerisa, D., Thiry, M., Franke, C., Gurenko, A., Gómez-Gras, D., Solé, J., Travé, A., 2019. Permian-Triassic red-stained albitized profiles in the granitic basement of NE

297   Spain: evidence for deep alteration related to the Triassic paleosurface. International Journal of Earth Sciences, 108, 2325-2347.

298   Fisher, J., Ross Lillie, R., Rakovan, J., 2013. Fluorite in Mississippi Valley–type Deposits. Rocks & Minerals, 88(1), 20-49.

299   Font, X., 1983: Estudio de las mineralizaciones del Macizo del Montseny-Guilleries (Barcelona y Girona) y su aplicación en la prospección geoquímica de redes de drenaje. Ph.

300   D. Thesis, Facultat de Geologia Universitat. de Barcelona, 317 pp.

301   Galindo, C., Tornos, F., Darbyshire, D.P.F., Casquet, C., 1994. The age and origin of the barite–fluorite (Pb–Zn) veins of the Sierra del Guadarrama (Spanish Central System, Spain):

302   a radiogenic (Nd, Sr) and stable isotope study. Chemical Geology, 112 (3-4), 351-364.

303   Juez-Larré, J., Andriessen, P.A.M., 2006. Tectonothermal evolution of the northeastern margin of Iberia since the break-up of Pangea to present, revealed by lowtemperature

304   fission-track and (U–Th)/He thermochronology: a case history of the Catalan Coastal Ranges. Earth and Planetary Science Letters 243 (1–2), 159–180.

305   Leach, D., Bradley, D., Lewchuk, M.T., Symons, D.T., de Marsily, G., Brannon, J., 2001. Mississippi Valley-type lead–zinc deposits through geological time: implications from recent

306   age-dating research. Mineralium Deposita 36 (8), 711–740

307   Makin, S.A., Simandl, G.J., and Marshall, D., 2014. Fluorite and its potential as an indicator mineral for carbonatiterelated rare earth element deposits. In: Geological Fieldwork

308   2013, British Columbia Ministry of Energy and Mines, British Columbia Geological Survey Paper 2014-1, pp. 207-212

309   Martínez, F.J., Reche, J., Iriondo, A., 2008. U-Pb SHRIMP-RG zircon ages of Variscan igneous rocks from the Guilleries massif (NE Iberia pre-Mesozoic basement): Geological

310   implications. Comptes Rendus Geoscience, 340, 223-232.

311   Martínez, F.J., Iriondo, A., Dietsch, C., Aleinikoff, J.N., Peucat, J.J., Cirés, J., Reche, J., Capdevila, R., 2011. U-Pb SHRIMPRG zircon ages and Nd signature of Lower Paleozoic

312   riftingrelated magmatism in the Variscan basement of the eastern Pyrenees. Lithos, 127, 10-23.

313   Mellado, E.; Corbella, M.; Navarro-Ciurana, D.; Kylander-Clark, A., 2021. The enriched Variscan lithosphere of NE Iberia: Data from post-collisional Permian calc-alkaline lampro-

314   phyre dykes of Les Guilleries. Geologica Acta, 19, 1–23.

315   Migdisov, A.A., Williams-Jones, A.E., 2014. Hydrothermal transport and deposition of the rare earth elements by fluorine-bearing aqueous liquids. Mineral. Deposita 49, 987–997.

316   Möller, P., Bau, M., Dulski, P., Lüders, V., 1998. REE and Y fractionation in fluorite and their bearing on fluorite formation. Proceed-ings of the 9th Quadrennial IAGOD Symp.,

317   Schweizerbart, Stuttgart, pp. 575–592.

318   Muchez, P., Heijlen, W., Banks, D., Blundell, D., Boni, M., Grandia, F., 2005. Extensional tectonics and the timing and formation of basin-hosted deposits in Europe. Ore Geology

319   Reviews. 27, 241–267.

320   Parcerisa, D., Thiry, M., Schmitt, J.M., 2010. Albitisation related to the Triassic unconformity in igneous rocks of the Morvan Massif (France). International Journal of Earth Sciences,

321   99, 527-544.

322   Piqué, À., Canals, À., Grandia, F., Banks, D.A., 2008. Mesozoic fluorite veins in NE Spain record regional base metal-rich brine circu-lation through basin and basement during

323   extensional events. Chem. Geol. 257, 139–152.

324   Plumlee, G. S., M. B. Goldhaber, and E. L. Rowan. 1995. The potential role of magmatic gases in the genesis of Illinois-Kentucky fluorspar deposits: Implications from chemical

325   reaction path modeling. Economic Geology 90:999–1011.

326   Reche, J., Martínez, F.J., 2002. Evolution of bulk composition, mineralogy, strain style and fluid flow during an HT-LP metamorphic event: sillimanite zone of the Catalan Coastal

327   Ranges, Variscan basement, NE Iberia. Tectonophysics, 348, 111-134.

328   Roca, E., Sans, M., Cabrera, L., Marzo, M., 1999. Oligocene to MiddleMiocene evolution of the central Catalan margin (northwestern Mediterranean). Tectonophysics 315 (1–4), 209–

329   229.

330   Salas, R., Guimer`a, J., Mas, R., Martín-Closas, C., Meléndez, A., Alonso, A., 2001. Evolution of the Mesozoic Central Iberian Rift System and its Cainozoic inversion (Iberian Chain).

331   In: Ziegler, P.A., Cavazza, W., Robertson, A.H.F., Crasquin-Soleau, S. (Eds.), Peri-Tethys Memoir 6: Peri-Tethyan Rift/Wrench Basins and Passive Margins, French National Museum of

332   Natural History, vol. 186, pp. 145–185.

333   Sánchez, V., Vindel, E., MartÍN-Crespo, T., Corbella, M., Cardellach, E., Banks, D., 2009. Sources and composition of fluids associated with fluorite deposits of Asturias (N Spain).

334   Geofluids 9, 338–355.

335   Sánchez, V., Cardellach, E., Corbella, M., Vindel, E., Martín, T., Boyce, A., 2010. Variability in fluid sources in the fluorite deposits from Asturias (N Spain): Further evidences from

336   REE, radiogenic (Sr, Sm, Nd) and stable (S, C, O) isotope data. Ore geology reviews, 37.

337   Schwinn, G.; Markl, G., 2005. REE systematics in hydrothermal fluorite. Chem. Geol., 216, 225–248.

338   Sizaret, S., Marcoux, E., Jebrak, M., Touray, J., 2004. The Rossignol Fluorite Vein, Chaillac, France: Multiphase Hydrothermal Activity and Intravein Sedimentation. Economic

339   Geology 99, 1107-1122.

340   Subías, I., Fanlo, I., Billström, K., 2015. Ore-forming timing of polymetallic-fluorite low temperature veins from Central Pyrenees: A Pb, Nd and Sr isotope perspective. Ore Geology

341   Reviews 70, 241–251.

342   Tanaka, T., Togashi, S., Kamioka, H., Amakawa, H., Kagami, H., Hamamoto, T., Yuhara, M., Orihashi, Y., Yoneda, S., Shimizu, H., Ku-nimaru, T., Takahashi, K., Yanagi, T., Nakano, T.,

343   Fujimaki, H., Shinjo, R., Asahara, Y., Tanimizu, M., Dragusanu, C., 2000. JNdi-1: a neodymium isotopic reference in consistency with La Jolla neodymium. Chemical Geology, 168, 279-

344   281.

345   Van Alstine, R. E. 1976. Continental rifts and lineaments associated with major fluorspar districts. Economic Geology, 71,977–87.

346   Taylor, S.R., McLennan, S.M., 1985. The Continental Crust: Its Composition and Evolution. Blackwell Scientific Publications Oxford, London, Edinburgh, 312.

CHAPTER 5

SUMMARY AND DISCUSSION

General aspects of Les Guilleries lamprophyres

The similarities among all LGL dykes in terms of direction, verticality, color, texture and mineral composition suggest that they came from the same magma source. This is consistent with the comparable HFSE, REE and some major elements contents (**Chapter2, Figure 2**) so they are possibly related to a unique intrusive event or close in time events. Additionally, systematic variations in Na2O, SiO2, K2O and LILE concentrations, correlated with variations in the abundance of albite and replacement textures (**Chapter 2, Figure 5**), suggest that LGL underwent an albitization process, with variable degrees of intensity. This albitization was also accompanied by chloritization and hematitization. Consequently, LGL register at least two geological processes of mineral formation, the magmatic event and at least one alteration event.

Petrographic classification and source characteristics

According to the major and trace element geochemistry described in **Chapter 2**, LGL have a calc-alkaline affinity. From the mineralogical point of view, though, alteration makes it difficult to classify these dykes, as the principal criteria of lamprophyre classification (Neuendorf et al., 2011) correspond to: i) relative abundance of primary mica and amphibole phenocrysts, which appear fully chloritizied in LGL, and ii) relative abundance of plagioclase and K-feldespar, which are strongly modified by albitization in LGL. The abundance of amphibole in the matrix and predominance of plagioclase in the less albitized samples point to a spessartitic composition. However, if the abundance of chlorite were due to alteration of original biotite/phlogopite, it would suggest a kersantitic composition instead. Either way, the mineral composition also points towards a calc-alkaline affinity. Nevertheless, the calc-alkaline lamprophyre definition includes the lack of feldspar phenocrysts, but they are present in LGL. The occurrence of feldspar phenocrysts may be of significance because they are attributed to an evolved magma within lamprophyric systems (Awdankiewicz, 2007). The evolved compositions have been described as transitional between spessartites and monzodiorites, although it is not clear whether this is due to fractional crystallization, assimilation or mixing with other magmas (Awdankiewicz, 2007).

Age and comparison with other lamprophyres

From field relations, LGL are younger than the c. 305 Ma Late-Hercynian leucogranites (Martinez et al., 2008) and c. 285 Ma microgranites (Martínez personal communication) found in Les Guilleries Massif, but before this study there were no constrain on the lower limit age. The shift from calc-alkaline to alkaline signature in Variscan related magmas during Permian times has long been recognized (Bonin, 1987). In the Pyrenees, this shift has been established between a 275 Ma calc-alkaline volcanism and 267 Ma alkaline volcanism (Denèle et al., 2012). As late Carboniferous-early Permian magmatism is very similar in the Pyrenees and the CCR (Aguilar et al. 2013), a similar shift in volcanism would be expected. Titanite age of 262+-7Ma presented in **Chapter 2** is in agreement with the above interpretation. LGL are easily distinguished from Permian alkaline lamprophyres from Central Iberia (Orejana et al., 2008) and from the Subbetic Zone in southern Spain (Puga et al., 2010), as they lack Nb-Ta, Ti and Eu negative anomalies. On the other hand, LGL show similar patterns to other calc-alkaline lamprophyres along the Variscan massifs, with negative Nb and Ti anomalies together with Pb positive anomalies. The most characteristic differences are LILE concentrations (Cs, Rb, Ba and K), which are anomalously low and variable among the LGL dykes. These particularities of LGL are probably the result of two superimposed different processes. On the one hand, alteration remobilized these elements,

reducing the absolute values and increasing the variability. On the other hand, LGL show low values not only in these mobile elements, but also in less mobile elements commonly enriched in calc-alkaline lamprophyres such as Th, La, Zr and P (Figs. 9 and 10). These suggest that LGL may come from a less enriched source in comparison to other Variscan regions. Overall, the geochemical composition of LGL fall inside the ranges of variation of lamprophyres from the Central Vosges (Soder, 2017) and the Bohemian Massif (Seifert, 2008); one group of lamprophyres from the Bohemian Massif, named LD2e-type (Seifert, 2008), show strikingly similar patterns in all elements except for the ones that may have been removed by albitization (Cs, Rb, Ba and K). Therefore, it is possible that concentrations of some of these elements where originally higher, as the maximum values in LGL (Cs: 2.2 ppm; Rb: 68 ppm; Ba: 776 ppm; Th: 6.13 ppm; K2O: 2.05 ppm; and P2O5: 0.4 ppm) are close or lower than the minimum values of LD2e type lamprophyres (Cs: 5.2 ppm; Rb: 78 ppm; Ba: 605 ppm; Th: 7.8 ppm; K2O: 2.13 ppm; and P2O5: 0.4 ppm). Another interesting feature is that very few of the many types of lamprophyres described in the Bohemian massif contain F concentrations below 1000 ppm like LGL do; among those are the LD2e type. As this type of lamprophyres reach values higher than 3000 ppm of F with a mean of 1800 ppm, it is also possible that fluorine concentrations in LGL were originally much higher. Additionally, the values of F concentration for calc-alkaline lamprophyres given by Rock (1991) are around 1100 ppm, which also support this possibility.

Post-magmatic processes

The replacement of primary magmatic phases by secondary minerals typical of greenschist facies metamorphism (calcite, chlorite and epidote) is an ubiquitous feature in many lamprophyres. This is sometimes understood as autometasomatic processes upon solidification of melts with high volatile content (Rock 1991). In the LGL this paragenesis have been observed but it occurs together with intense albitization and hematitization. On the other hand, the variable degree of albitization of the LGL suggest that these dykes belong to either different magmatic pulses with variable amounts of SiO2 and alkalis, or the albitization event was younger than post-solidification and modified major element concentrations at different proportions. Most samples show strikingly similar concentrations in most elements and the principal differences occur in the more mobile elements (Cs, Rb, Ba, K and Pb), suggesting similar source characteristics and a post-emplacement remobilization of these elements. Additionally, systematic variations in Na2O, SiO2, K2O, CaO, Ba, Rb, Cs, Pb, Sr, Tl and Zn (**Chapter 2, Figure 5**), correlated with variations in the abundance of albite, chlorite, hematite, titanite and replacement textures, strongly suggest that LGL were affected by post-magmatic albitization accompanied with chloritization and hematitization. The highest values of LOI (Loss On Ignition) are encountered in the less albitizied sample (**Chapter 1, Table 1**), pointing to volatile loss during albitization. This sample also presents the lowest values of iron and the highest of aluminum, suggesting an addition of iron and a loss of aluminum during albitization, which correlates well with the increase in hematitization and progressive albitization of Ca-plagioclase, respectively. The addition of Fe and hematititzation could also be related to the loss of the element during the chloritization and albitization of amphiboles. The anomalously low values of K$_2$O and K$_2$O/Na$_2$O in LGL with respect to lamprophyres from other massifs, are only shared by Aiguablava spessartites, which may suggest that the albitization was a regional process that did not occur in other massifs.

Subtle differences in REE concentrations may also be due to elemental mobility during albitization. The more albitized dyke show some of the lowest values from La to Eu, being the Eu the most mobile (up to 10% less with respect to the less albitized dyke). As Eu commonly replaces Ca in plagioclase, some Eu is expected to be lost during albitization. Dissolution/replacement of apatite may also explain the slight decrease in LREE contents, as no apatite were found in the more albitized dyke. Nevertheless, only very small apatite crystals (<10 µm) were found in the less albitized dykes, so the impact would be very small.

On the other hand, allanite crystals probably control the REE patterns observed in the dykes, as it is the main REE bearing mineral present in LGL. The intense alteration of allanite crystals observed in BSE microscopy (Fig. 4f) coupled with very small variation of whole rock

REE contents (Fig. 6d) indicate that the mobility of these elements was scarce. In situ U-Th-Pb dates of 29 analytical points in allanite crystals yield a weighted mean age of 265 ± 15 Ma. The coincidence of allanite dates in Les Guilleries lamprophyres with the period following the main syn- to post-collisional Variscan magmatism in the Catalan Coastal Range (280–250 Ma), in conjunction with the differences in allanite tex-tures, suggest the allanite crystals from this study represent multi-stage metamorphic, magmatic and/or hydrothermal processes that occurred both before partial melting of the lamprophyre's source and later, during the early, late and post-magmatic evolution of the post-collisional system.

Similar secondary alteration minerals have been observed in late-Variscan granitoids of the extended Montseny-Guilleries Massif, with precipitation of minute hematite crystals and albitization of pristine plagioclases (e.g. Fàbrega et al., 2013). Pseudomorphic replacement of the primary plagioclases into albite, pseudomorphic replacement of primary biotite into chlorite and minor precipitation of minerals like albite, chlorite, apatite, hematite, calcite and titanite, are also observed in Paleozoic rocks of the Variscan Morvan Massif in France (Parcerisa et al., 2010). Based on their geometric and petrographic characteristics, the authors conclude that these secondary alterations were developed under low temperature subsurface conditions in relation to the Triassic palaeosurface. Interestingly, the elements that may have been remobilized by the albitization are the same found concentrated in epigenetic vein mineralizations nearby. They seem to be related to hydrothermal fluid circulation induced by late to post-Variscan granitic intrusions and later events in the CCR (eg. Zn, Pb and F; Amigó and Font-Altaba, 1966; Campá-Viñeta and Montoriol-Pous, 1974; Ayora 1990). Most hydrothermal activity in Catalan Coastal Ranges has been linked to tectonic events occurring between the Variscan and Alpine orogenies. The end of the Variscan orogeny in the CCR is marked by the last magmatic pulse with a calc-alkaline geochemical signature, namely Les Guilleries lamprophyres with U-Pb titanite date of 262±7Ma. These mafic dykes were emplaced in the upper Variscan crust after the main syn- to post-collisional magmatism, which contain evolved batholitic-sized calc-alkaline granitoids, minor mafic intrusions with local ultramafic cumulates, and peraluminous leucogranite bodies, emplaced in the lower Paleozoic basement of Les Guilleries (which host the Osor fluorite deposit). These occurred in an environment evolving from peak compression to strike-slip motions, to later extension during orogenic collapse, and related to mantle delamination, asthenospheric upwelling and rapid exhumation. An enriched SCLM origin has been inferred indirectly for the most mafic components of the post-collisional magmatic system, indicating a direct fluid pathway between mantle and crustal fluids during the orogenic collapse, which was also cogenetic with volcanism in pull-apart basins evolving from calc-alkaline-to-alkaline geochemistry during Permian times (Arche et al., 1999), followed by post-orogenic hydrothermal activity. Recent studies have suggested that an albitization event developed under low-temperature subsurface conditions previous to erosion that led to the Lower Triassic paleosurface (Fàbrega et al., 2019; Parcerisa et al., 2010). Mellado et al. (2021) pointed out that a similar hydrothermal event affected Les Guilleries lamprophyres producing intense albitization and remobilizing elements like Ba, F, Pb, Zn, the same elements that are concentrated in nearby Osor fluorite deposit. This led to the suggestions that the same event that formed Osor fluorite deposits affected Les Guilleries lamprophyres, indicating and upper limit to the age of Osor deposit (262±7Ma). This is consistent with the Sm-Nd isochrones age of 224±85Ma.

Geodynamic environment of formation: implications for the Variscan orogeny

The Variscan orogeny was the result of the collision between Laurussia and Gondwana with several microcontinents set between these two large continents. As these two large continents approached, subduction-collision systems and related magmatism where developed (Franke, 2014). A recent review of Schulman et al. (2014) shows that the Variscan evolution of continental Europe resulted from several major orogenic cycles which were not superimposed in space and time. The northern Variscan realm (western and central Europe) is generally dominated by well-characterized Late Devonian-Carboniferous tectono-metamorphic and magmatic events. These rifting, subduction and collisional events are defined by sedimentary records, crustal growth, recycling of continental crust and large-scale deformations observed. The southern European

Variscan realm (Spain, southern France and Italy) has a different appearance, as the area was reworked by a major late Carboniferous-Permian post-collisional events, sometimes superimposed on previous Late Devonian and Carboniferous orogenic processes. The evidence for this late event is marked by localized magmatic recycling, extensional and transcurrent tectonic settings and development of localized sedimentary basins (Schulman et al., 2014). In spite of the differences between diverse subduction-collision systems, the timing of the Variscan magmatism show a progressive shift from Laurasia towards Gondwana from late Devonian to Permian. Subduction-collision related magmatism occurred between c. 375-327 in the Bohemian massif (Lardeaux et al., 2014); c. 334-312 Ma in Vosges (Tabaud et al., 2014); c. 344-297 Ma in Maures Massif (Elter et al., 2004); c. 326-280 Ma in the Pyrenees and CCR (Martinez et al. 2008; Bea et al., 1999); c. 320-230 in Sardinia and Corsica (Traversa et al., 2003). Calc-alkaline lamprophyres seem to occur in the post tectonic phase of the Variscan magmatism (Awdankiewicz, 2007; Seifert, 2008; Soder, 2017), following a period of subduction, mantle-enrichment and later transcurrent tectonics that opened the conduits for mantle derived magmas to reach upper crustal levels. Structural and paleomagnetic studies show that the Variscan orogen had a predominant N-S direction during late Devonian-Early Carboniferous, but changed the magnetic orientation during late Carboniferous-early Permian times (305-280 Ma; Edel et al. 2014). This trend is interpreted by Edel et al. (2014) in terms of a large-scale 90° clockwise rotation of the southern branch of the Variscan belt that matches the successive change in shortening directions revealed by structural geology. The relative rotation between Gondwana and Laurassia can account for the transcurrent motions needed for the emplacent of calc-alkaline lamprophyres in upper crustal levels and could explain why they have younger ages towards the south. The higher contents of potassium in the lamprophyres of the northern massifs (Bohemian, Vosges) with respect to the southern parts (Pyrenees, CCR), show similarities with what occurs in young subduction-collision systems. In Tuscany (Italy) the transition from older lamproitic (ultrapotassic) to young high-K calc-alkaline rocks, through shoshonites, is a time-related feature (Conticcelli et al., 2009). This characteristic has been interpreted as an increasing contribution of a lithospheric mantle component to the hybrid vein-derived magmas with time. Minette and lamproitic magmas of the Tuscan Province reflect low degree of partial melting, which involves mainly the vein components, whereas shoshonitic and high-K calc-alkaline magmas would correspond to higher degrees of melting where the surrounding peridotitic wall rock interacted with the vein melts (Conticcelli et al., 2009). An increasing temperature regime is assumed in the Variscan realms during Late Carboniferous to Lower Permian since c. 340 Ma (Franke, 2014), so higher degrees of partial melting of the lithospheric mantle would be expected with time. This could explain why younger lamprophyres from the southern domains are less enriched in K_2O and related elements, while in the northern parts there are older and more potassic lamprophyres. On the other hand, the presence of ultrapotassic magmatism in the Bohemian massif have also been related to ultra-high pressure rocks (Janoušek and Holub, 2007); therefore, heterogeneities in mantle composition beneath the different massifs may also contribute to these geochemical differences. An example of how these mantle heterogeneities can be formed is provided by numerical simulations of colissional systems (Faccenda et al., 2009).

Although it is challenging to establish a direct relationship between the calc-alkaline lamprophyres from the different Paleozoic massifs, they were all the result of complex processes that involved mixing between variable proportions of crustal materials and the lithospheric mantle during the development of subduction-collision systems of the Variscan orogeny, and a subsequent differential partial melting of these heterogeneous domains during transcurrent tectonics. More and better quality data is needed to truly understand these widely heterogenous potassium rich mantle derived rocks, the lamprophyres, and the interplay between subduction of different lithologies, migration of elements to the mantle wedge, mantle metasomatism, ancient mantle enrichments, partial melting, fractional crystallization, magma mixing and tectonism.

Lithologies like high-K basalts and gabbros show remarkably similar chemistry to calc-alkaline lamprophyres; their geochemical variation is rather a continuum, which suggests that our current discrete petrological classification misses to relate rocks that may be intimately related. One example of this is the classification of calc-alkaline lamprophyres and alkaline lamprophyres

in the same group ('lamprophyre') although they are rather different, whereas calc-alkaline lamprophyres are deeply related to other Variscan igneous rocks, but are usually considered exotic and less significant than granites or basalts. Here we show that Variscan calc-alkaline lamprophyres are widespread and show even higher geochemical variability that the rest of Variscan rocks, as well as the highest enrichments in LILE, HFSE and REE. Therefore their study is fundamental to understand how subducted materials are recycled in SCLM and how the elements are incorporated in the different types of orogenic magmatism.

Collisional orogens host many of the important hydrothermal ore deposits in the world, but their building itself has the limited metallogenic endowment with respect to mountain building by either pre-collisional accretionary orogeny or post-collisional rifting orogeny. Metallogenesis of collisional orogens is pre-conditional by the pre-enrichment of ore-forming elements in the orogenic crust and mantle. Heterogeneous fertilization of the mantle wedge by the subduction of oceanic lithosphere generates the metasomatic domains with variable enrichment of ore-forming elements. This process provides metal pre-enriched reservoirs that can be reactivated by continental rifting magmatism, resulting in the formation of hydrothermal ore deposits either immediately during accretionary orogeny or later on during collisional and rifting orogenesis. In this regard, the generation of metal preenriched domains in the mantle wedge is the key step to the metallogenesis of either accretionary or collisional orogens.

References

Aguilar, C., Liesa, M., Castineiras, P., Navidad, M., 2014. Late-Variscan metamorphic and magmatic evolution in the eastern Pyrenees revealed by U-Pb age zircon dating. Journal of Geological Society of London, 171, 181-192.

Amigó, J., Font-Altaba, M., 1966. Contribución al conocimiento mineralogenético del yacimiento de fluorita de Osor (Gerona). Estudios Geológicos, 22, 167-170.

Awdankiewicz, M., 2007. Late Paleozoic lamprophyres and associated mafic subvolcanic rocks of the Sudetes (SW Poland): petrology, geochemistry and petrogenesis. Geologia Sudetica, 39, 11-97.

Ayora, C., Soler, A., Melgarejo, J.C., 1990. The Hercynian ore deposits from the Catalonian Coastal Ranges. Acta Geologica Hispánica, 25, 65-73.

Bea, F., Montero, P., Molina, J.F., 1999. Mafic precursors, peraluminous granitoids, and late lamprophyres in the Avila batholith: A model for the generation of Variscan batholiths in Iberia. Journal of Geology, 107, 399-419.

Bonin, B., 1987. From orogenic to anorogenic magmatism: a petrological model for the transition calcalkaline- alkaline complexes. Revista Brasileira de Geociencias, 17(4), 366-371.

Campá-Viñeta, J.A., Montoriol-Pous, J., 1974. Mineralogénesis del yacimiento de Osor (Gerona). Acta Geologica Hispánica, 4,139-141.

Conticelli, S., 2009. Trace elements and Sr-Nd-Pb isotopes of K-rich, shoshonitic, and calc-alkaline magmatism of the Western Mediterranean Region: Genesis of ultrapotassic to calc-alkaline magmatic associations in a post-collisional geodynamic setting. Lithos, 107, 68-92.

Denèle, Y., Paquette, J.L., Olivier, P., Barbey, P., 2012. Permian granites in the Pyrenees: the Aya pluton (Basque Country). Terra Nova, 24,105-11.

Edel, J.B., Casini, L., Oggiano, G., Rossi, P., Schulmann, K., 2014. Early Permian 90° clockwise rotation of the Maures–Estérel–Corsica–Sardinia block confirmed by new palaeomagnetic data and followed by a Triassic 60° clockwise rotation. Geological Society of London, Special Publication, 405, 333-361.

Elter, F.M., Corsi, B., Cricca, P., Muzio, G., 2004. The south-western Alpine foreland: correlation between two sectors of the Variscan chain belonging to 'stable Europe': Sardinia(-) Corsica and the Maures Massif (south-eastern France). Geodinamica

Acta, 17, 31-40. Enrique, P., 1990. The Hercynian intrusive rocks of the Catalonian Coastal Ranges (NE   Spain). Acta Geologica Hispánica, 25, 39-64.

Fàbrega, C., Parcerisa, D., Thiry, M., Franke, C., Gurenko, A., Gómez-Gras, D., Solé, J., Travé, A., 2019. Permian-Triassic red-stained albitized profiles in the granitic basement of NE Spain: evidence for deep alteration related to the Triassic paleosurface. International Journal of Earth Sciences, 108, 2325-2347.

Faccenda, M., Minelli, G., Gerya, T.V., 2009. Coupled and decoupled regimes of continental collision: Numerical modeling. Earth Planetary Science Letter, 278, 337-349.

Franke, W., 2014. Topography of the Variscan orogen in Europe: failed–not collapsed. International Journal of Earth Sciences, 103, 1471-1499.

Janoušek, V., Holub, F.V., 2007. The causal link between HP-HT metamorphism and ultrapotassic magmatism in collisional orogens: Case study from the Moldanubian Zone of the Bohemian Massif. Proceedings of the Geologists Association, 118, 75-86.

Lardeaux, J.M., et al., 2014. The Moldanubian Zone in the French Massif Central, Vosges/Schwarzwald and Bohemian Massif revisited: differences and similarities. In: Schulmann, K., et al., 2014. The Variscan Orogeny: Extent, Timescale and the Formation of the   European Crust. Geological Society of London Special Publications, 405.

Le Maitre, R.W., et al., 2002. Igneous Rocks: A Classification and Glossary of Terms. Cambridge   University Press.

Martínez, F.J., Reche, J., Iriondo, A., 2008. U-Pb SHRIMP-RG zircon ages of Variscan igneous rocks from the Guilleries massif (NE Iberia pre-Mesozoic basement): Geological implications. Compt Rendus Geosci, 340, 223-232.

Neuendorf, K.K.E., Mehl, J.P., Jackson, J.A., 2011. Glossary of Geology, 5th edition. Alexandria, VA. American Geological Institute.

Orejana, D., Villaseca, C., Billström, K., Paterson, B.A., 2008. Petrogenesis of Permian alkaline lamprophyres and diabases from the Spanish Central System and their geodynamic context within western Europe. Contributions to Mineral Petrology, 156, 477-500.

Parcerisa, D., Thiry, M., Schmitt, J.M., 2010. Albitisation related to the triassic unconformity in igneous rocks of the morvan massif (France). International Journal of Earth Sciences, 99, 527-544.

Puga, E., et al., 2010. First evidence of lamprophyric magmatism within the Subbetic Zone (Southern Spain). Geologica acta, 8, 111-130.

Rock, N.M.S., 1991. Lamprophyres. Blackie, Glasgow and London.

Schulmann, K., Catalán, J.R.M., Lardeaux, J.M., Janoušek, V., Oggiano, G., 2014. The Variscan orogeny: extent, timescale and the formation of the European crust. Geological Society of London Special Publications, 405, 1-6.

Seifert, T., 2008. Metallogeny and Petrogenesis of Lamprophyres in the Mid-European Variscides. Amsterdam, IOS Press, 303.

Soder, C., 2017. Geochemistry and petrology of lamprophyres from the Hellenides and the European Variscides. PhD Thesis. Heidelberg (Germany), University of Heidelberg, 201.

Tabaud, A.S., et al., 2014. Devonian-Permian magmatic pulses in the northern Vosges Mountains (NE France): result of continuous subduction of the Rhenohercynian Ocean and Avalonian passive margin. In: Schulmann, K., et al., 2014. The Variscan Orogeny: Extent, Timescale and the Formation of the European Crust. Geological Society of London Special Publications, 405, 1-6.

Traversa, G., et al., 2003. Late to post-Hercynian dyke activity in the Sardinia-Corsica Domain: A transition from orogenic calc-alkaline to anorogenic alkaline magmatism. Bollettino della Società geologica italiana, 2, 131-152.

CHAPTER 6

CONCLUSIONS

The relative position of Guilleries massif and the Catalan Coastal Ranges with respect to other Paleozoic massifs of Western Europe place the NE Iberia domain in external position with respect to the internal Reic Suture. Similarities in basement lithologies and tectonothermal evolution had led to correlations with adjacent massifs in the Pyrenees, Iberian Ranges and Sardinia. However, each massif present its own unique characteristics in terms of peak metamorphic conditions, the volume of magmatic manifestations, the proportion of volcanic and plutonic products, the proportion of mafic and felsic products, geometry of main structures, the timing of compression-tranpression-transtention-extention and the proportion and geochemistry of mafic dykes. These differences are expected as modern collisional orogens show that these parameters vary widely in space and time and at very smale scales, depending on the distribution of km-scale coeval compression and extention during the orogenic cycle. Here we present detailed descriptions of Les Guilleries lamprophyres, allanites crystals contained in them, and fluorites from the Osor deposits that improve the overall knowledge of mineralizing systems related with late-post Variscan events in Les Guilleries massif.

The main contributions of this thesis are detailed geochemical descriptions of two elements of the post-collisional Variscan system of Les Guilleries massif, Les Guilleries lamprophyres and Osor fluorite deposit. Les Guilleries lamprophyres correspond to mafic dikes emplaced vertically in an E-W direction in the metamorphic basement and in late Variscan plutons of the Les Guilleries Massif. The lamprophyres have calc-alkaline geochemical affinity and correspond to amphibole–plagioclase-dominated spessartites with a wide variety of accessory phases (titanite, ilmenite, allanite, fluorapatite, spinel, zircon, sulfides) and secondary minerals (albite, chlorite, epidote, titanite and calcite). Their enrichment in LILE, HFSE and REE and initial Sr-Nd isotopic compositions ($87Sr/86Sri$ between 0.70851 and 0.71127, ε Ndi between -5.23 and -4.63) are consistent with an enriched subcontinental lithospheric mantle source. U-Pb dating in titanite yield a concordia age of 262±7Ma. Post-magmatic processes are evidenced by intense chloritization and albitization of the lamprophyres, together with systematic variations of Na_2O vs SiO_2, K_2O, CaO, Ba, Rb, Cs, Pb, Sr, Tl, and Zn, and possibly the removal of F. The geochemical and geochronological are consistent with the transitional tectonic regime between Variscan compression/transpression and post-collisional transtension/extension, related to the fragmentation of Pangea and thinning of the lithosphere. The lamprophyre dykes studied could represent the youngest pulse of Variscan orogenic magmatism and, therefore, mark its end in NE Iberia before the onset of the generalized Triassic extension. The main REE-bearing accessory phase in Les Guilleries lamprophyres is allanite. SEM-EPMA and LA-ICP-MS chemical analyses in allanite revealed a solid solution between epidote and allanite with a ferriallanite component. Heterogeneity in crystal shapes, sizes, type of zoning, dissolution embayment textures, growth of epidote coronas, mineral paragenesis, and the unique geochemical characteristics of allanite crystals suggest multiple crystallization events. Two types of allanite–epidote composite grains were identified: allanite Type I, with regular allanite–epidote core-to-rim zoning and a secondary allanite rim; and allanite Type II, with anhedral allanite cores surrounded by epidote coronas. Additionally, irregular zoning, complex dissolution textures and REE redistribution suggest the occurrence of deuteric and/or post-magmatic processes. Multivariate statistical analyses of major elements in allanite–epidote composite grains show a relationship between major textural and geochemical variations, mainly related to cationic substitutions. U-Pb-Th dating in allanite yield weighted mean age of 265 ± 15Ma similar to the age of emplacement of the lamprophyres in the

upper crust in the mid–late Permian. To account for the diversity of allanite grains in Les Guilleries lamprophyres, a combination of metamorphic processes prior to partial melting, early–late magmatic crystallization, and/or post-magmatic hydrothermal processes are suggested as the most plausible explanations.

Fluorite samples from the Osor deposit display maximum REY values of 258ppm and consistent PAAS normalized REY patterns with depletions of LREE and HREE, enrichment in MREE, Eu and Y positive anomalies. Tb/Ca vs Tb/La as well as Y vs Yb diagrams corroborate the hydrothermal origin proposed in previous studies, and also its MVT affinity. These patterns suggest large scale fluid circulation and homogenization prior to deposition, with metamorphic rocks as the main source of mineralizing elements, and probable contributions from the Variscan crystalline basement. Field relations combined with Sm-Nd isotopic compositions restrain the age of Osor fluorite deposits: they are younger than 262±Ma, older than 137 ±25 Ma, and most probably formed in the Lower Triassic; however, younger Osor fluorite ages indicate there was also a much younger mineralizing event during Miocene times.